POLITECNICO
MILANO 1863

SCUOLA DI INGEGNERIA INDUSTRIALE
E DELL'INFORMAZIONE

Magnetic switching of Ta/CoFeB/MgO heterostructures via Spin-Orbit Torque for memory applications

Tesi di Laurea Magistrale in
Electronics Engineering - Ingegneria Elettronica

Author: **Matteo Fettizio**

Student ID: 946715
Advisor: Prof. Riccardo Bertacco
Co-advisors: Dr. Luca Nessi
Academic Year: 2021-22

Abstract

In the landscape of emerging memory technologies, perpendicular magnetic tunnel junctions have been attracting great interest due to their favourable scalabilty, their high thermal stability and their possibility of efficient current-induced switching.
Due to the combined possibility to provide thin films with perpendicular magnetic anisotropy and high tunneling magnetoresistance and efficient Spin-Orbit Torque, the Ta/CoFeB/MgO heterostructure has rapidly become the preferred one for state of the art memory applications. The aim of this work is the exploitation of Ta/CoFeB/MgO thin films for the fabrication of perpendicular magnetic tunnel junctions and for the realization of magnetization reversal via Spin-Orbit Torque (SOT) effect, a current-induced switching mechanism enabled by the charge to spin conversion taking place in a heavy metal channel, topological insulator or Rashba system underlying the junction. In its first stage, the work focuses on the realization of CoFeB/MgO based thin films with perpendicular magnetic anisotropy (PMA). Once the desired magnetic properties are obtained, perpendicular magnetic tunnel junctions (pMTJs) are fabricated and characterized, while Spin-Orbit Torque switching is independently studied on Ta/CoFeB/MgO based Hall bars using anomalous Hall effect to probe the state of the magnetization. An accurate study of the dependencies of SOT induced switching on external magnetic fields parallel and transverse to the injected current is carried out, highlighting the presence of field induced asymmetries on the switching behaviour. These asymmetries are therefore analyzed quantitatively and possible physical explanations are provided.
Finally, we explore the possibility of using SOT to obtain multistate state switching and to manipulate the latter using a magnetic field transverse to the injected current, with a view to the development of spintronic memristive devices for neuromorphic applications.

Keywords: perpendicular magnetic anisotropy, Spin-Orbit Torque, magnetic tunnel junction, lithography, tunneling magnetoresistance, SOT-MRAM, neuromorphic computing

Abstract in lingua italiana

Nel panorama delle tecnologie per le memorie emergenti, le giunzioni a effetto tunnel con anisotropia magnetica perpendicolare hanno attratto grande interesse grazie alla loro scalabilità, la loro stabilità termica e la possibilità di sfruttare la corrente per indurre switching.
Viste le possibilità combinate di garantire film sottili con anisotropia magnetica perpendicolare e alta magnetoresistenza tunnel, la eterostruttura Ta/CoFeB/MgO è diventata rapidamente la favorita per la realizzazione di dispositivi di memoria allo stato dell'arte. Lo scopo di questo lavoro è l'utilizzo di film sottili basati sulla struttura Ta/CoFeb/MgO per la fabbricazione di giunzioni a effetto tunnel con anisotropia magnetica perpendicolare e per la realizzazione di switching magnetico tramite Spin-Orbit Torque (SOT), un meccanismo di inversione magnetica indotto da corrente basato sulla conversione carica-spin avente luogo in un layer composto da un metallo pesante, isolante topologico o sistema Rashba posto al di sotto della giunzione.
Nella prima fase il lavoro si concentra sulla realizzazione di film sottili basati sulla struttura Ta/CoFeB/MgO aventi anisotropia magnetica perpendicolare. Una volta ottenute le proprietà magnetiche desiderate, giunzioni a effetto tunnel sono fabbricate e caratterizzate, mentre la commutazione indotta da Spin-Orbit torque è studiata indipendentemente su delle Hall bar basate sulla stessa eterostruttura in cui l'effetto Hall anomalo viene usato per sondare lo stato della magnetizzazione.
Viene presentato uno studio accurato delle dipendenze dello switching magnetico indotto da SOT da campi magnetici esterni paralleli e trasversi rispetto alla corrente iniettata, mettendo in evidenza la presenza di asimmetrie nel comportamento di switching indotte dal campo esterno. Queste asimmetrie sono quindi analizzate quantitativamente e sono fornite possibili cause fisiche. Infine, viene esplorata la possibilità di usare l'effetto di SOT per ottenere switching di stati intermedi e di manipolare quest'ultimo con un campo magnetico trasverso rispetto alla corrente iniettata, con la prospettiva di realizzare dispositivi spintronici con carattere memristivo per applicazioni neuromorfiche.

Parole chiave: anisotropia magnetica perpendicolare, Spin-Orbit Torque, giunzione a effetto tunnel magnetica, magnetoresistenza tunnel, SOT-MRAM, computazione neuro-

morfica

Contents

1 | Introduction

1.1. The evolution of magnetic storage

Ferromagnets are materials that can present a net macroscopic magnetic moment even in the absence of an external magnetic field and this makes them suitable for the storage of digital information.
Let us consider a ferromagnet with uniaxial anisotropy, having the relationship between applied field and magnetization of Figure 1.1.

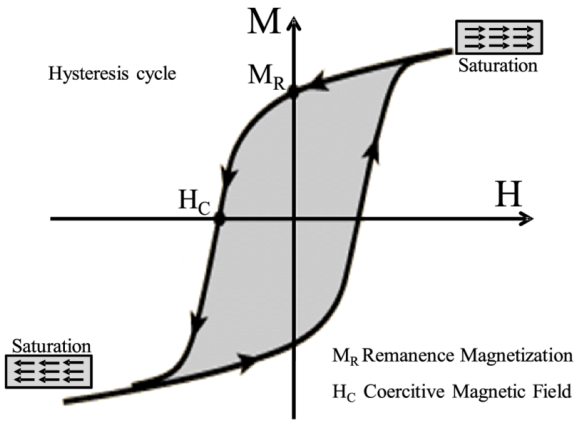

Figure 1.1: M-H loop of a ferromagnet when the external field is applied parallel to its easy axis. The image is taken from Ref. [10].

.

The anisotropy forces the magnetization to lie along two directions only, parallel or antiparallel to the easy axis, so it is straightforward to associate to these two possible states the two units of information, the bits "0" and "1".
Looking at the hysteresis cycle of Figure 1.1, two advantages of encoding bits as magnetic states arise:

- The information does not need a power supply to be retained, since it relies on the remanent magnetization;

- The information is stable against external perturbation up to the coercive field of the structure.

These characteristics, therefore, suggest the possibility of using ferromagnetic materials to realize non volatile memories.
The first use of magnetism for data storage is the magnetic hard drive, developed by IBM in 1956. However, due to the time consuming reading and writing processes, such technology cannot sustain direct communication with a CPU and therefore has been limited to secondary memories(HDD in Figure 1.2).

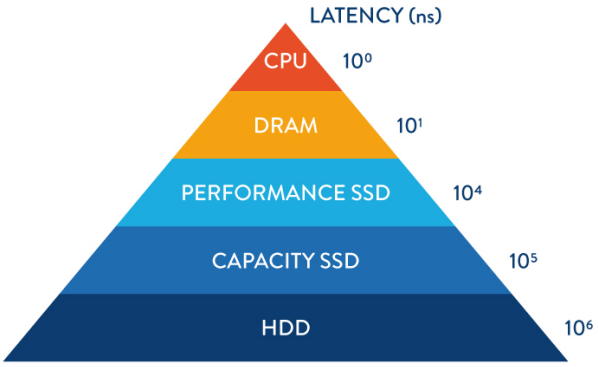

Figure 1.2: The memory hierarchy pyramid. Every level has decreasing latency as it approaches the CPU. The image is taken from Ref. [49].

The discoveries of giant magnetoresistance in 1988 by Fert [15] and of tunneling magnetoresistance in 1975 by Julliere [32] open new horizons for magnetic storage, allowing it to finally represent a competitive alternative to CMOS technology for the implementation of primary memories (DRAM in Figure 1.2).
As discussed in detail in Section 2.2, When a tunneling barrier is placed between two ferromagnetic layers, the current flowing perpendicularly to them experiences a different resistance depending on whether their magnetizations are oriented parrallel or antiparallel to each other. Associating the two bits to these two configuration allows the creation of a new non volatile device in which information can be accessed fastly and efficiently by means of a resistance measurement.
This is in fact the working principle of the "magnetoresistive random access memory" (MRAM), which has been integrated in commercial storage units with progressively higher density over the past 20 years [19]. Non volatilty and efficient readout let this technology reach performances comparable to standard DRAM and SRAM in terms of power consumption and access time [19], but the first generation of MRAM presents a fundamental limitation that kept it from having the edge over the CMOS counterpart.
The writing process was based on the reversal of one the two layers (free layer) by means

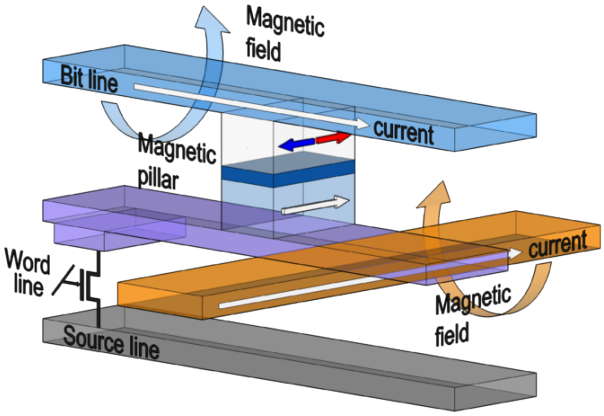

Figure 1.3: Illustration of the writing process of a MRAM element. Since the devices are arranged in a matrix, two writing lines are required to select the desired one. The image is taken from Ref. [30].

.

of the Oersted field generated by two current lines placed in proper proximity of the junction, as indicated in Figure 1.3.
Since the magnetic field required to switch a storing element is roughly inversely proportional to its size, the reduction of the latter implies a non sustainable increase of the writing current, thus limiting scalability [40].
The described issue was solved with the discovery of Spin transfer torque (STT) by Slonczewsky in 1996 [20], which allows to flip the bit of a memory cell simply by running a current through it thanks to the transfer of magnetic moment from the fixed layer to the free layer. The physical details behind this mechanism are provided in Section 2.3.1.
Oersted fields are no longer needed, but sharing the same path for reading and writing introduces new reliability issues, such as unwanted bit flipping during the read operation [4] or barrier breakdown due to large writing currents [57].
The discovery of Spin Orbit Torques (SOT) introduced a way to solve this issue, since it permits to write the magnetization of the cell's free layer injecting a current in a heavy metal layer, topological insulator or Rashba system placed underneath it [37]. As better explained in Section 2.3.2, due to spin-orbit interaction this current gets converted into a pure spin current which provides the magnetic momentum needed for switching.
Decoupled read and write path, along with fast switching and improved power consumption, makes this generation of MRAM, called SOT-MRAM, the most promising for large scale integration [37] (Figure 1.4).
Due to the simple realization, initially MRAM elements were realized with in plane magnetized junctions. However, relying on shape anisotropy for the stability against thermal fluctuation makes the latter decrease as the cell size scales down. The stability ratio Δ is

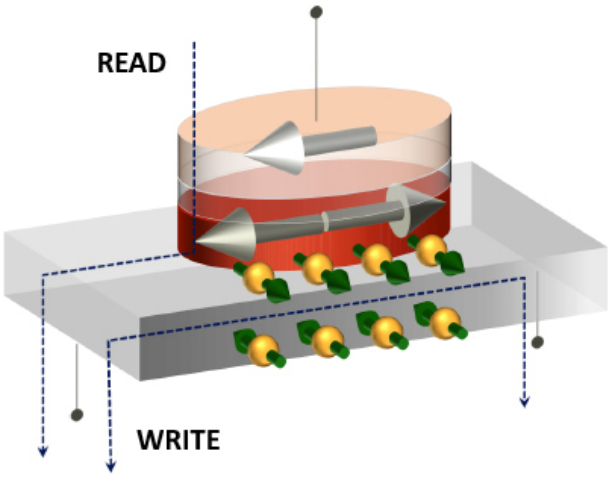

Figure 1.4: Illustration of a SOT-MRAM element.The two decoupled reading and writing path are highlighted. The green arrows in the writing channel represent the spin current generated by SOT. The image is taken from Ref. [51].

.

given by [19].

$$\Delta = \frac{E_b}{K_b T} = \frac{\pi^2 M_s^2 t \omega (AR - 1)}{K_b T}, \tag{1.1}$$

where E_b is the energy barrier between the two bits, K_b the Boltzmann constant, T is the working temperature, ω is the width of the cell, AR is the length-witdh ratio of the cell, t is the thickness of the cell, M_s is the saturation magnetization. From Equation 1.1 the linear decrease of Δ with ω is evident.

A succesfull solution proposed to overcome the scalability-thermal stability tradeoff is the introduction of materials with perpendicular magnetic anisotropy (PMA). Of particular relevance is the observation of large PMA in CoFeB/MgO heterostructures, when the CoFeB thickness is around 1nm, due to interfacial effects [18].

This system, in fact, not only provides PMA but it is also suitable for the realization of magnetic tunneling junction since, when grown on top of CoFeB, MgO can achieve the (001) texture needed to give rise to a high tunneling magnetoresistance (TMR) [22].

Finally, the presence of tantalum, beneficial for PMA [22], allows for SOT induced writing due to the high spin hall angle of its beta crystalline phase [28].

In conclusion, these are the reasons why the experimental work described in this thesis deals with the realization and characterization of Ta/CoFeB/MgO/CoFeB/Ta based perpendicular magnetic tunneling junctions (pMTJ) and of SOT switching of Ta/CoFeB/MgO trilayers, with the future goal of integrating the results obtained in the final SOT-MRAM element.

1.2. Summary and outlook of the thesis

All the experimental activities were conducted at PoliFab, Politecnico di Milano, within the Nanomagnetism and Spintronics group (NaBis) under the supervision of prof. Riccardo Bertacco, over a time span of ten months.
The experimental work presented in this thesis is divided in two main parts.
The first part focuses on the fabrication and characterization of Ta/CoFeB/MgO/CoFeB/Ta based pMTJs.
The initial step is the realization of CoFeB/MgO and MgO/CoFeB based thin films with PMA, to be later combined in the full heterostructure needed for the junctions.
Once the desired magnetic properties are obtained, the pMTJs' lithographic process is carried out and finally the devices are electrically characterized to evaluate crucial parameters such as R×A product and TMR.
The second part is centered on the realization of SOT switching in Ta/CoFeB/MgO films. Hall bars are fabricated using trilayers with different Tantalum's thickness, in order to assess its influence on the SOT efficiency.
Once correct SOT induced magnetization reversal is obtained, the dependence of the latter on the presence of external magnetic fields is investigated.
Finally, the possibility of multistate switching is investigated, due to its importance in the emerging field of neuromorphic computing.
The thesis is organized as follows. Chapter 2 provides the main theoretical concepts behind the phenomena studied experimentally. After a brief introduction about the basics of micromagnetism, the attention is focused on more advanced effects such as tunneling magnetoresistance, spin orbit torque and anomalous Hall effect.
In Chapter 3 the main experimental techniques needed for the fabrication and characterization of the devices are presented.
Chapter 4 and 5 delineate the experimental work carried out throughout the thesis.
The first presents the results regarding the magnetic and electrical characterization of, respectively, the thin films with PMA and the pMTJs, along with the description of the latter's fabrication process.
The second deals with the realization of SOT switching of Ta/CoFeB/MgO trilayers, briefly showing the hall bars' fabrication method and focusing more on the measurements' results.
Finally, the last chapter presents the conlcusions and some proposals for possible further developments of the work carried out so far.

2 | Theoretical background

2.1. Micromagnetics

Ferromagnets (FMs) are a wide class of materials with very peculiar properties. The most striking feature is the existence of a macroscopic non-zero magnetization $\boldsymbol{M}$, defined as the average magnetic moment per unit volume, in zero external magnetic field. This so-called remanence magnetization is due to the partial alignment of magnetic moments at the atomic scale and manifests through the external field (stray field) which it generates. Ferromagnetic properties disappear if the material reaches a critical temperature, called Curie temperature (T_c), after which a phase transition occurs and paramagnetic behaviour arises.
Magnetic phenomena are described in terms of three inter-related vectors: the magnetic flux density $\boldsymbol{B}$, the magnetic field $\boldsymbol{H}$ and the magnetization $\boldsymbol{M}$, which are related by the following equation:

$$\boldsymbol{B} = \mu_0(\boldsymbol{H} + \boldsymbol{M}) \tag{2.1}$$

The magnetic configuration of a ferromagnet in equilibrium conditions depends on several competing contributions to the total energy of the system [11]; the equilibrium state corresponds to the minimum (or minima) of the free Gibbs energy, as established by statistical physics. They are: exchange energy, dipolar or magnetostatic energy, magneto-crystalline anisotropy, Zeeman coupling to an external field and interfacial effects.
The first fundamental contribution to the total energy represents the essence of magnetic phenomena: the exchange interaction between spins. It arises from the anti-symmetry of the wavefunction describing an ensemble of electrons and it can be represented by the Heisenberg Hamiltonian:

$$H = \sum_{i<j} J_{ij} \boldsymbol{S}_i \cdot \boldsymbol{S}_j \tag{2.2}$$

Within the framework of micromagnetism, in which a mesoscopic point of view is taken and the magnetic "elementary cell" contains several spins, the exchange energy is modelled by:

$$E_{ex} = \frac{A}{2}\int_V [(\nabla m_x)^2 + (\nabla m_y)^2 + (\nabla m_z)^2]dV \tag{2.3}$$

with m_i cartesian components of the magnetization unit vector $\boldsymbol{m} = \frac{\boldsymbol{M}}{|\boldsymbol{M}|}$. A is called exchange stiffness because the higher its value, the more difficult it is to cause a steep variation of the magnetization.
The exchange interaction term associates a high energy cost to configurations where $\boldsymbol{m}$ varies rapidly in space.
Dipolar energy is related to the magnetostatic intra-interaction of the magnetic moments and can be expressed as two equivalent integrals of the form:

$$E_m = -\frac{\mu_0}{2}\int_V \boldsymbol{M}\cdot\boldsymbol{H}_{dem}dV \;=\; \frac{\mu_0}{2}\int_{allspace} \boldsymbol{H_{dem}}\cdot\boldsymbol{H}_{dem}dV \tag{2.4}$$

With $\boldsymbol{M}$ the magnetization and $\boldsymbol{H}_{dem}$ the demagnetizing field caused by the magnetic moments seen as a continuum.
In case the ferromagnet is an ellipsoid, the two vectors $\boldsymbol{M}$ and $\boldsymbol{H}_d$ are proportional through a second order diagonal tensor $\boldsymbol{N}$, the demagnetizing tensor, with unitary trace and with elements determined by the actual shape: $\boldsymbol{H}_{dem} = \boldsymbol{NM}$ [36]. The previous relation can be reformulated as:

$$E_m = \frac{\mu_0}{2}\int_V [N_x M_x^2 + N_y M_y^2 + N_z M_z^2]dV \tag{2.5}$$

The expression is at the basis of the so-called shape anisotropy: the geometry of the sample determines the values of the N_i and hence the total energy.
Realistic applications however involve thin films which are not second order surface. They can however be approximated as a thin ellipsoid elongated in the xy plane, for which we have that $N_x \simeq N_y << N_z$. The consequence of this condition is that magnetostatic energy can be written as:

$$E_{dem} \simeq \frac{\mu_0}{2} N_z M_z^2 \tag{2.6}$$

It follows that in thin films, due to shape anisotropy, the energetically favourable situation is the one with the magnetization alligned with the film's plane. Therefore, other effects must be exploited to obtain thin films with out of plane magnetic anisotropy, treated in this thesis.
The third important term is the anisotropy which is induced by intrinsic properties of the material and hence does not have only one specific origin. One cause comes from the interaction between magnetic dipoles, which comprises a term dependent on the crystalline

properties of the material:

$$E_{an} = \frac{\mu_0}{2} \int_V \boldsymbol{M} \cdot \boldsymbol{\Lambda} \cdot \boldsymbol{M} dV \tag{2.7}$$

Where $\boldsymbol{\Lambda}$ is a tensor depending on the crystalline structure.
Secondly, spin-orbit interaction, which couples the spin angular momentum of an electron moving in an electric field to its orbital angular momentum, also plays a role in establishing the anisotropy. Qualitatively speaking, since some values of the orbital angular momentum $\boldsymbol{L}$ are stabilized by the crystal lattice and since the electron spin interacts with $\boldsymbol{L}$, the anisotropy of the lattice influences the spin direction [6].
A relevant case in experimental studies is the one of uniaxial anisotropy, in which the anisotropy energy can be modeled as a function of the angle θ between a given axis and the magnetization that satisfies rotational symmetry:

$$E_{an} = k_0 + k_1 sen^2(\theta) + k_2 sen^4(\theta) + ... \tag{2.8}$$

The case of interest in this work, thin films with perpendicular anisotropy, is the one in which only k_0 and k_1 are retained and k_1 is positive, meaning the out of plane direction corresponds to the so called easy axis and the plane perpendicular to it corresponds to the hard plane.
Perpendicular anisotropy has been reported in many FM/oxide systems due to the combined action of orbitals' hybridization at the interface and of spin orbit interaction which couples the preferential direction of magnetization with the lattice orientation [13].
The interface contribution to the free energy can be described in terms of surface density energy, which adds up to the total effective uniaxial anisotropy constant of the thin film:

$$K_{eff} = K_v - \frac{\mu_0}{2} M_s^2 + \frac{K_s}{t} \tag{2.9}$$

where K_v accounts for all the material bulk anisotropy contributions, $-\frac{\mu_0}{2} M_s^2$ represents the demagnetizing energy and K_s represents the interfacial contributions.
If the interfacial contribution is dominant over the demagnetization one, which tends to keep the magnetization in plane, thin films with PMA can be obtained.
The last considered contribution to the free energy is the one given by the presence of an external magnetic field. Its interaction with the magnetization, in fact, gives rise to an additional energy contribution having the following expression:

$$E_z = \frac{\mu_0}{2} \int_V \boldsymbol{H} \cdot \boldsymbol{M} dV \tag{2.10}$$

Equation 2.10 implies that the energy given by the presence of the external field is minimized when the latter and the magnetization are parallel.
From a dynamics standpoint, the external field exerts a torque on the magnetization which is equal to the rate of change of the magnetization itself:

$$\boldsymbol{\tau} = \frac{\partial \boldsymbol{M}}{\partial t} \propto \boldsymbol{M} \times \boldsymbol{H} \tag{2.11}$$

Such a torque is responsible for a precessional motion of $\boldsymbol{M}$ around $\boldsymbol{H}$ and so it does not allow the system to reach the condition of minimal energy. A way of modeling the collapse of the magnetization on the direction of the field is to include in the equation of motion a phenomenological damping term, thus obtaining the Landau–Lifshitz–Gilbert equation [17]:

$$\frac{\partial \boldsymbol{M}}{\partial t} = -\gamma \boldsymbol{M} \times H_{eff} + \frac{\alpha}{M_s}(\boldsymbol{M} \times \frac{\partial \boldsymbol{M}}{\partial t}) \tag{2.12}$$

Finally, all these competing terms sum up and constitute the total energy of the system. In the framework of micromagnetism then the total free energy can be written as follows:

$$E_{tot} = constant + \int_V (\frac{A}{2}[(\nabla m_x)^2 + (\nabla m_y)^2 + (\nabla m_z)^2] + k_1 sen(\theta)^2 + \frac{\mu_0}{2}\boldsymbol{H} \cdot \boldsymbol{M} - \frac{\mu_0}{2}\boldsymbol{M} \cdot \boldsymbol{H}_{dem})dV \tag{2.13}$$

Therefore, the magnetization is assumed locally uniform as it would be in a small particle and the total energy results from the integration over the contributions of volume elements dV. In addition, $\boldsymbol{M}$ attains its saturation value M_s everywhere and only changes direction from one volume element to another (macrospin model).
The stable equilibrium magnetization corresponds to the spatial configuration of the latter that minimizes the total energy. Brown demonstrated that, locally, the equilibrium magnetization lies parallely to the effective field $\boldsymbol{H}_{eff}$, which comprises several terms and involves all the parameters influencing the energy (anisotropy constants, exchange stiffness, saturation magnetization etc.).

2.2. Tunneling magnetoresistance

The magnetic tunnel junctions studied in this thesis belong to a wider class of devices called spin valves, widely used to investigate properties associated with spin transport. The basic spin valve device is a trilayer structure consisting of a paramagnetic (NM) layer sandwitched between two ferromagnetic (FM) layers. The first approach developed to model the current transport in ferromagnets, later applied to FM/NM/FM systems, is the Mott two current model [1], which assumes that at temperatures well below the Curie temperature most scattering mechanisms that an electron will encounter during its flow will preserve its spin direction. Since spin is conserved it can be considered a good quantum number and therefore it is possible to define two different energy sub bands whose states are defined not only by their wave vector but also by their spin. This consideration allows to derive the Stoner-Wohlfarth model band structure, which considers free electron dispersion for both minority and majority carriers, with minority displaced upward (in the energy axis) from majority by an amount equal to the exchange splitting energy Δ. The majority dispersion $E_\uparrow$ and the majority dispersion $E_\downarrow$ are given by:

$$E_\uparrow = \frac{\hbar^2 k^2}{2m_0} \tag{2.14}$$

$$E_\downarrow = \frac{\hbar^2 k^2}{2m_0} + \Delta \tag{2.15}$$

In order for this model to be valid some assumptions must be satisfied:

- Spin orbit coupling should be negligible, otherwise spin is not a good quantum number anymore.
- The two layers of the spin valve must have collinear magnetizations, otherwise a majority or minority spin in a layer becomes a linear combination of minority and majority spin in the other one, causing the two channels to mix up.
- The temperature must be well below the Curie temperature so that magnon scattering, which causes spin flip events, is negligible.

Since, under this hypothesis, transport is due to two non interacting channels, it is possible to describe it treating independently the flow of majority and minority carriers. Due to spin dependent phenomena taking place in FM/NM/FM structures, which depend on the nature of the materials involved, in general electron flow is subject to different resistances depending on whether the magnetizations of the two ferromagnetic layers are parallel (R_P) or antiparallel (R_{AP}).

The non magnetic spacer can be either metallic or insulating, with the fundamental difference that in the first case the transport is conductive, while in the second it occurs through tunneling. The magnetic tunnel junctions treated in this thesis work belong to the second case. In these structures the resistance difference between parallel and antiparallel configuration is characterized by the parameter called tunneling magnetoresistance (TMR):

$$TMR = \frac{R_{AP} - R_P}{R_P} \tag{2.16}$$

A simple but effective model to calculate the quantities described above in magnetic tunnel junctions was provided by Jullière in 1975 [32]. In his pioneering work, Jullière presented a formula to calculate the TMR based on a generalization of the transfer matrix model [38].

Let us consider a tunnel barrier interposed between two electrodes. In absence of bias the two Fermi levels are aligned, but a shift equal to eV arises when an external voltage V is applied to the electrode. This displacement of the Fermi levels is responsible for a current that can be evaluated starting from the Fermi golden rule as follows:

$$I(V,E) = I_{L\to R} + I_{R\to L} \propto |T|^2 \int_{\infty}^{\infty} D_L(E) D_R(E + eV_{bias})[f(E) - f(E - eV_{bias})]dE \tag{2.17}$$

Where $D_L(E)$, $D_R(E)$ are the densities of states of the left and the right electrodes, $|T|^2$ the square of the tunneling matrix element assumed constant over the relevant energy range $\simeq eV_{bias}$, and $f(E)$ the Fermi distribution.

In the low-bias regime (V $\to$ 0) and at low temperatures:

$$\lim_{V_{bias},T\to 0} \frac{[f(E) - f(E - eV_{bias})]}{eV_{bias}} = \delta(E - E_F) \tag{2.18}$$

Where E_F is the Fermi energy. Whit this semplification the conductance becomes:

$$G = \frac{dI}{dV} \propto |T|^2 D_L(E_F) D_R(E_F) \tag{2.19}$$

Where G is the zero-bias conductance of the tunneling junction.

In the case of magnetic electrodes, the densities of states for electrons with spin parallel $D^{\uparrow}(E)$ and anti-parallel $D^{\downarrow}(E)$ to the magnetization are different because the energy bands of up-spin and down-spin electrons are splitted by the exchange interaction. The additional assumption that the spin of the electron is conserved in tunneling makes the current in the up-spin and down-spin channels flow as in two wires in parallel (Figure 2.1).

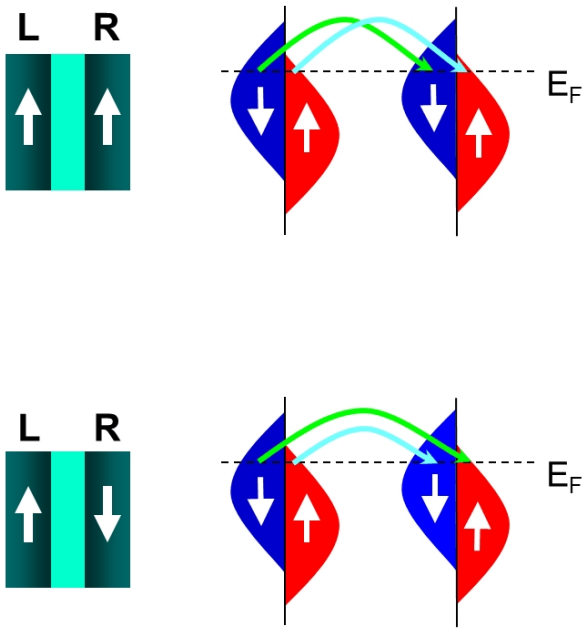

Figure 2.1: Pictorial representation of Jullière model. The image on the top represents transport in the parallel configuration while the one on the bottom represents transport in the antiparallel configuration. Arrows indicate the magnetization on the left and the spin magnetic moment on the right. From Ref. [50].

This allows to write the conductance associated to the parallel and antiparallel configuration as follows:

$$G_{AP} \propto D_L^{\uparrow}(E_F)D_R^{\downarrow}(E_F) + D_L^{\downarrow}(E_F)D_R^{\uparrow}(E_F) \tag{2.20}$$

$$G_P \propto D_L^{\uparrow}(E_F)D_R^{\uparrow}(E_F) + D_L^{\downarrow}(E_F)D_R^{\downarrow}(E_F) \tag{2.21}$$

Two parameters, P_1 and P_2, are introduced to characterize the spin polarization of the left and right electrodes, respectively:

$$P_1 = \frac{D_L^{\uparrow}(E_F) - D_L^{\downarrow}(E_F)}{D_L^{\uparrow}(E_F) + D_L^{\downarrow}(E_F)} \tag{2.22}$$

$$P_2 = \frac{D_R^{\uparrow}(E_F) - D_R^{\downarrow}(E_F)}{D_R^{\uparrow}(E_R) + D_R^{\downarrow}(E_R)} \tag{2.23}$$

The tunneling magnetoresistance as a function of P_1 and P_2 results from the Jullière formula:

$$TMR = \frac{G_P - G_{AP}}{G_{AP}} = \frac{2P_1P_2}{1 - P_1P_2} \tag{2.24}$$

Equation 2.24 indicates that, in order to obtain junctions with very high TMR, the electrodes' spin polarization should be as close as 1 as possible. From a band structures standpoint, unitary spin polarization can be obtained if the exchange splitting is such that the minority band is completely above the Fermi level and therefore no minority carriers are available for conduction.

Materials with this properties are called half metals [17] and a well-known example is lanthanum strontium manganite ($La_{2/3}Sr_{1/3}MnO_3$), which allows to realize tunnel junctions with TMR up to 1800% at a working temperature of 4.2 K using a strontium titanate ($SrTiO_3$) barrier [5].

Jullière model assumes constant transmission coefficients that do not depend on the characteristics of the electronic structure of the various layers. Such an approach is however not suitable for epitaxial heterostructures in which the crystalline order strongly affects the orbital properties of the flowing electrons. An example of inadequacy of the Jullière model is the epitaxial Fe/MgO/Fe structure, studied by Butler in 2001 [7].

In his study, Butler analyzes in detail the transmission probability as a function of the electrons' wave vector for all the three dimensions of reciprocal space.

Calculations show that transmission probability is maximum for the states having their wave vector directed perpendicularly to the surface ($k_{||} = 0$), therefore the band structure along this direction must be evaluated in order to investigate the transmission properties of each state populating it. In epitaxial Fe/MgO/Fe structures the direction perpendicular to the interface corresponds to [001](Γ-H) direction and the band structure along the latter is shown in Figure 2.2.

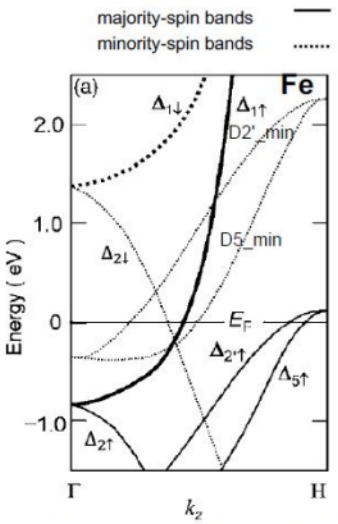

Figure 2.2: Band dispersion of Fe in the [001](Γ-H) direction. From Ref. [5].

We focus our attention to Δ_1 states. While the majority sub-band $\Delta_{1_\uparrow}$ crosses the Fermi level, the minority sub-band $\Delta_{1_\downarrow}$ lies completely above it, giving the system a half metallic behaviour. Δ_1 states are the most relevant because, due to their symmetry, they couple very effectively from Fe into MgO and also out of MgO into Fe of the electrode on the other side. This aspect can be appreciated in Figure 2.3, which displays the evolution of the minority and majority densities of states with $k_{||} = 0$ along the junction for parallel and antiparallel configuration.

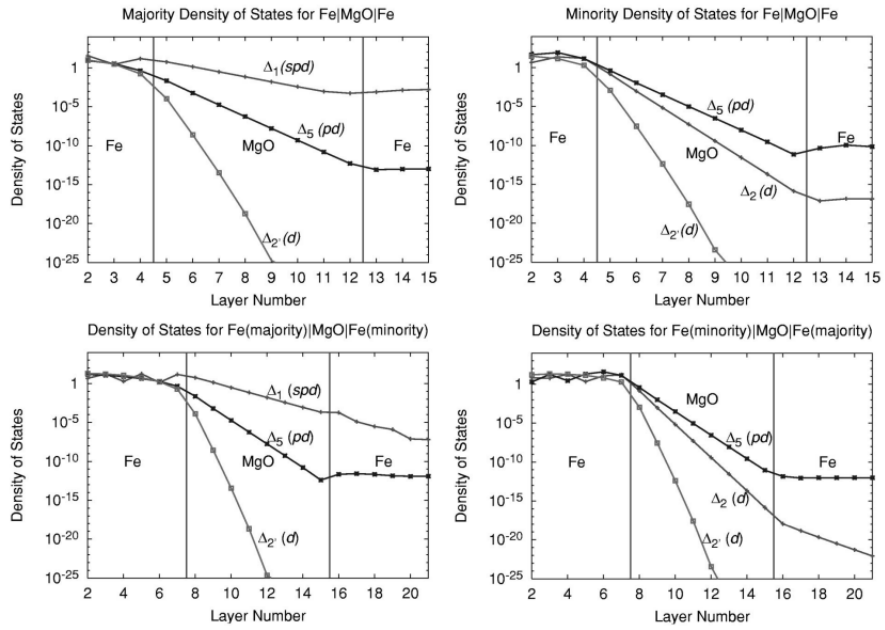

Figure 2.3: Tunneling DOS (TDOS) for Fe(100)/MgO/Fe(100). The four panels show the tunneling DOS for majority (upper left) minority (upper right), and antiparallel alignment of the moments in the two electrodes (lower panels). Additional Fe layers are included in the lower panels to show the TDOS variation in the Fe. Each DOS curve is labeled by the symmetry of the incident Bloch state in the left Fe electrode. From Ref. [5].

The graphs show that the states with Δ_1 simmetry are the largest contributors to the tunneling transport. Moreover, it can be noticed that the DOS for majority Δ_1 states is weakly attenuated in the parallel configuration while it gets strongly attenuated in the antiparallel cofiguration due to the half metallic behaviour mentioned earlier.
This k dependent tunneling is therefore responsible for the remarkably high TMR observed in this systems, which can reach few hundreds % at room temperature [45].

2.3. Spin Orbit Torques

2.3.1. Spin Transfer Torque

The LLG equation (Equation 2.12) states that when an external magnetic field is applied to a ferromagnet, its magnetization will tend to align to it thanks to the exerted torque and the dissipative term.
Applying a magnetic field, however, is not the only way to manipulate magnetization. A spin current with a given polarity, in fact, is able to exert a torque on a non collinear magnetic moment by means of the spin transfer torque effect.
In order to explain the physics behind this phenomenon we make use of a toy model [45] in which an electron with a given spin polarization direction flows into a ferromagnet with non collinear magnetization (Figure 2.4).

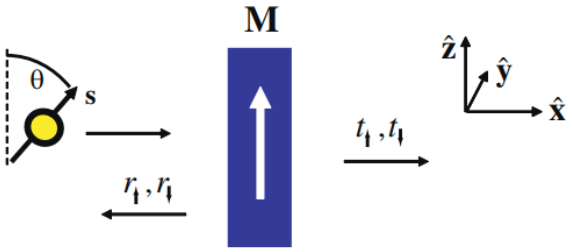

Figure 2.4: Illustration of the toy model explained in text. From Ref. [45].

The spin current associated with an electron of wave function ψ is a tensor embedding the information about direction of motion in real space and polarization in spin space and it is defined as:

$$\boldsymbol{Q} = \frac{\hbar^2}{2m} Im(\psi * \sigma \otimes \boldsymbol{\nabla}\psi) \tag{2.25}$$

For sake of simplicity we consider an incident plane wave electron whose spinor is expressed as a linear combination of the eigenstates of the ferromagnet:

$$\psi = \frac{e^{ikx}}{\sqrt{V}}(cos(\frac{\theta}{2})|\uparrow\rangle + sin(\frac{\theta}{2})|\downarrow\rangle) \tag{2.26}$$

Where V is the normalization volume, k the wave vector of the electron flowing along the x direction, θ the direction of the electron's spin polarization with respect to the magnetization of the ferromagnet. For a generic spinor with coefficients of up-spin and down-spin components equal to a and b respectively, Equation 2.25 allows to calculate

the three components of the spin current's polarization.

$$Q_{xx} = \frac{\hbar^2}{2m} 2Re(ab^*) \tag{2.27}$$

$$Q_{xy} = \frac{\hbar^2}{2m} 2Im(ab^*) \tag{2.28}$$

$$Q_{xz} = \frac{\hbar^2}{2m} (|a|^2 - |b|^2) \tag{2.29}$$

We describe the spin filtering property of the ferromagnet by considering different transmission and reflection coefficients for the up spin component of the wave function ($t_\uparrow$,$r_\uparrow$) and for the down spin component ($t_\downarrow$,$r_\downarrow$). While Equation 2.26 represents the incident wave functions, the transmitted and reflected one become:

$$\psi_{tr} = \frac{e^{ikx}}{\sqrt{V}} (t_\uparrow cos(\frac{\theta}{2}) |\uparrow\rangle + t_\downarrow sin(\frac{\theta}{2}) |\downarrow\rangle) \tag{2.30}$$

$$\psi_{ref} = \frac{e^{ikx}}{\sqrt{V}} (r_\uparrow cos(\frac{\theta}{2}) |\uparrow\rangle + r_\downarrow sin(\frac{\theta}{2}) |\downarrow\rangle) \tag{2.31}$$

Equations 2.32, 2.33 and 2.34 allow then to calculate the components of the associated spin current.

By conservation of angular momentum, one can say that the spin transfer torque acting on some volume of material can be computed by determining the net flux of nonequilibrium spin current through the surfaces of that volume. Taking an incident surface of the ferromagnet of area A, the net flux of nonequilibrium spin curren (i.e. spin transfer torque) through this surface is given by:

$$N_{st} = A\boldsymbol{x} \cdot (\boldsymbol{Q}_{in} + \boldsymbol{Q}_{ref} - \boldsymbol{Q}_{tr}) = \frac{A\hbar^2 k}{2Vm} sin(\theta)[(1 - Re(t_\uparrow t_\downarrow^* + r_\uparrow r_\downarrow^*))\boldsymbol{x} - Im(t_\uparrow t_\downarrow^* + r_\uparrow r_\downarrow^*))\boldsymbol{y}] \tag{2.32}$$

Of course, there is no torque applied in the direction parallel to the magnetization. In general, therefore, the applied torque is entirely perpendicular to the magnetization upon which it acts and it can be decomposed in two normal components, one directed as $\boldsymbol{M} \times \boldsymbol{\sigma}$ and the the other directed as $\boldsymbol{M} \times (\boldsymbol{M} \times \boldsymbol{\sigma})$, where $\boldsymbol{\sigma}$ is the versor of the incoming electrons' polarization. We call the first one field-like torque because it causes the magnetization to precess around $\boldsymbol{\sigma}$, analogously to the action of a field directed in the same way, while we call the second one damping-like torque because it pushes the magnetization towards the direction of the incoming spin current, analogously to the usual damping term of the LLG equation.

Tackling the problem from a different point of view allows to get more insights about the

relative entities of these two torques.
Let us consider a plane wave electron impinging against the non collinear ferromagnet. The transmitted part of the wave function feels the strong exchange field and starts precessing around it, while the reflected part interacts with it only during the scattering event and it acquires a certain phase due to the same precessional motion.
In real systems, however, many electrons are incident on the magnetic layer from several directions, corresponding to states belonging to different parts of the Fermi surface, and therefore different electrons take different paths through the magnetic layer. For this reason the $\boldsymbol{x}$ and $\boldsymbol{y}$ components of the transmitted and reflected spin current cancel out and the main contribution of the absorbed spin torque comes from the transverse component of the incident spin current. Since the latter belongs to the plane formed by the incident spin current poplarization and the magnetization, the absorbed momentum only contributes to the damping-like torque.

$$\boldsymbol{N}_{st} = A\boldsymbol{x} \cdot (\boldsymbol{Q}_{in} + \boldsymbol{Q}_{ref} - \boldsymbol{Q}_{tr}) \simeq A\boldsymbol{x} \cdot \boldsymbol{Q}_{in_\perp} \tag{2.33}$$

The spin transfer torque is related to the rate of angular momentum change, so in order to take into account its effect on the magnetization's dynamics the term $\frac{\boldsymbol{N}_{st}|g|\mu_b}{\hbar V}$ has to be added to the LLG equation, where V is the volume of the magnetic body. The LLG equation becomes:

$$\frac{\partial \boldsymbol{M}}{\partial t} = -\gamma \boldsymbol{M} \times H_{eff} + \frac{\alpha}{M_s}(\boldsymbol{M} \times \frac{\partial \boldsymbol{M}}{\partial t}) + \tau_{DL}(\boldsymbol{M} \times (\boldsymbol{M} \times \boldsymbol{\sigma})) + \tau_{FL}(\boldsymbol{M} \times \boldsymbol{\sigma}) \tag{2.34}$$

where τ_{DL} and τ_{FL} are the damping-like and field-like coefficients.
The concepts explained above are exploited to develop the Spin-Transfer Torque MRAM (STT-MRAM), mentioned in section 1.1, which allowed to solve the scalability-writing current tradeoff proper of field-induced switching MRAMs.
The basic element of STT-MRAMs is the usual magnetic tunnel junction. The magnetization of one of the two layers is pinned (pinned layer), for example by means of exchange bias, while the one of the other layer (free layer) is free to rotate upon the application of an external input.
In the case of STT-MRAMs, this input is provided by letting a current flow through the junction and expoiting the spin transfer torque effect.
Let us suppose we want to toggle the state of the junction from antiparallel to parallel and we inject a current such that electrons flow from the fixed layer to the free layer.
Electrons, initially randomly spin polarized, enters the fixed layer and their spin polarization alings with the ferromagnet's momentum due to the interaction with the large

exchange field. This current is therefore spin polarized and it is able to exert a torque on a non collinear ferromagnet.
Note that the free layer has its magnetization parallel to the one of the fixed layer therefore spin torque should not be effective. Due to thermal energy, however, in case of uniaxial anisotropy the free layer's magnetization randomically fluctuates around the equilibrium position given by the anisotropy field [46]. The situation, for a magnetic junction polarized in the z direction in which current flows in the z direction, is displayed in Figure 2.5.

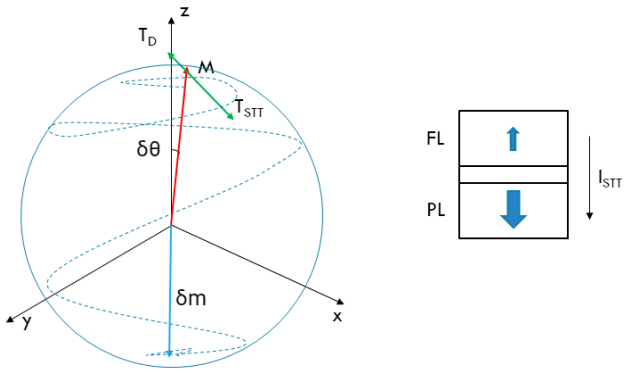

Figure 2.5: (Left image) Representation of the magnetization $\boldsymbol{M}$, tilted by $\delta\theta$ with respect to the z axis, and the torques acting on it during the action of the spin polarized current giving rise to the non equilibrium magnetization $\boldsymbol{\delta m}$. The damping-like spin transfer torque $\boldsymbol{T}_{STT}$ is opposite with respect to the Gilbert damping torque $\boldsymbol{T}_D$ and therefore it can destabilize the +z direction allowing switching through damped precessional motion (dashed blue curve). The precessional motion showed is qualitative and not obtained via simulations. (Right image) Pictorial representation of a STT-MRAM element with out of plane magnetizations. PL stands for pinned layer while FL stands for free layer. The verse of the current I_{STT} is opposite to the electrons' net velocity.

The spin polarized current has an associated non equilibrium magnetic moment $\boldsymbol{\delta m}$ having opposite verse with respect to the spin polarization $\boldsymbol{\sigma}$ owing to the negative sign of the gyromagnetic ratio of electrons. Since the anisotropy field and the polarization of the spin current are collinear and opposite, the Gilbert damping torque $\propto \boldsymbol{M} \times (\boldsymbol{H}_{an} \times \boldsymbol{M})$ and the damping-like component of the spin transfer torque $\propto \boldsymbol{M} \times (\boldsymbol{\delta m} \times \boldsymbol{M})$ have the same geometrical relationship and therefore they act in opposite ways on the magnetization [46]. When the input current is high enough, in fact, the spin transfer torque overcomes the Gilbert damping one and $\boldsymbol{M}$ is forced to collapse on the other equilibrium position along -z.

In case of switching from parallel to antiparallel state the mechanism is analogous, with the difference that now the electrons must flow from the free to the pinned layer. In this case, the fraction of minority electrons that remains non polarized after flowing through the free layer gets reflected at the interface with the pinned layer and re-interact with the free layer exerting STT.

2.3.2. Origin of Spin Orbit Torques

The spin transfer torque effect has been widely employed in the development of novel magnetic memories. In that case the spin current necessary to transfer angular momentum is a charge current that gets polarized by the fixed layer of the memory element. However, considering that in a two current model the spin current is defined as the difference between the current of up-spin and down-spin electrons, a pure spin current can flow in absence of charge current provided that the up-spin and down-spin flows are identical in magnitude but opposite in sign (see Equation 2.40 and 2.41 below).

$$j_s = j_\uparrow - j_\downarrow \tag{2.35}$$

$$j_c = j_\uparrow + j_\downarrow \tag{2.36}$$

In case of spin transfer torque the spin polarized charge current transfers its angular momentum to the ferromangets' magnetization via exchange interaction between the itinerant electrons and the ferromagnets' lattice electrons.
Spin polarized charge current is not however the only source of magnetic momentum of a system. The total angular momentum of the system includes contributions from the ions comprising the lattice and the electrons, which possess an orbital angular momentum and an intrinsic angular momentum derived from their spin. Each of these components represents a reservoir of angular momentum and they can transfer it from one to another thanks to various interactions [2], as it is represented in Figure 2.6.

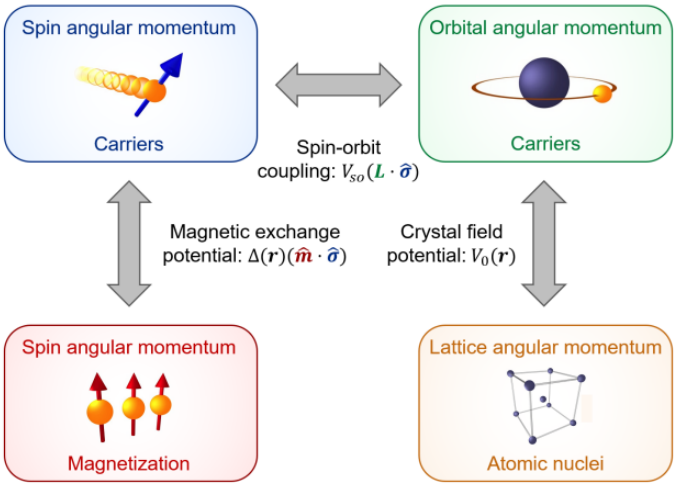

Figure 2.6: Schematic of different angular momentum reservoirs and the interactions coupling them. From Ref. [2].

The interactions responsible for the flow of angular momentum are summarized in the Hamiltonian for the electrons:

$$H = \frac{\hbar^2\nabla^2}{2m} + V_0(\boldsymbol{r}) + \Delta(r)(\boldsymbol{m}\cdot\boldsymbol{\sigma}) + V_{so}(\boldsymbol{L}\cdot\boldsymbol{\sigma}) \tag{2.37}$$

The first term is the kinetic energy. The second term is the crystal field, which breaks rotational symmetry so that electron's angular momentum is not conserved. This term allows the transfer of angular momentum from the lattice to the carriers. The third term is the exchange interaction between the itinerant electrons and the local magnetization and it permits momentum transfer between the two. The last term is the spin-orbit coupling (SOC).

SOC is rooted in the Lorentz transformation of an electric field into a magnetic field in the reference system of a moving charged particle, say an electron, through the following relation:

$$\boldsymbol{B} = \frac{\boldsymbol{E}\times\boldsymbol{v}}{2c^2\sqrt{1-\frac{v^2}{c^2}}} \tag{2.38}$$

If the particle presents a magnetic moment $\boldsymbol{\mu}$, the scalar product $-\boldsymbol{\mu}\cdot\boldsymbol{B}$ defines the energy of the interaction. Since $\boldsymbol{\mu}$ is proportional to the spin, it is clear that the interaction couples the electron motion to its spin. In a single particle picture, when the electric field originates from the nucleus to which the electron is bound, the interaction takes the form $\boldsymbol{L}\cdot\boldsymbol{\sigma}$, where $\boldsymbol{L}$ is the orbital angular momentum.

SOC is responsible for phenomena that allow the conversion of a charge current into a

pure spin current [2, 43]. If we use this spin current to manipulate the magnetization of ferromagnet then we talk about spin-orbit torque effect (SOT), whose effectiveness for magnetization reversal has been widely demonstrated [14, 26, 31]. The exact origin of SOT is still a matter of debate as different magnetic structures feature different behaviour in terms of magnitude of the effect and give hints of the concomitance of more mechanisms at work at the same time. It originates from the Spin Hall Effect (SHE) and the Rashba and Dresselhaus interactions which, despite intrinsically distinct phenomena, share the coupling between the spin and orbital motion [2].
Rashba effect arises in NM/FM heterostructures due to the breaking of inversion asymmetry introduced at the interface. The potential step between the two different materials is associated with a strong electric field directed perpendicular to the interface which transforms into an effective $\boldsymbol{k}$ dependent magnetic field in the reference frame of the moving electron. The energy term in the Hamiltonian is:

$$H_{Rashba} = \eta(\boldsymbol{k} \times \boldsymbol{z}) \cdot \boldsymbol{\sigma} \tag{2.39}$$

Where η is a parameter related to the strength of the Rashba effect, $\boldsymbol{k}$ is the electron's wave vector and $\boldsymbol{\sigma}$ is the Pauli matrix. Two bands splitted in $\boldsymbol{k}$ space arise characterized by a coupling between spin and momentum of the electrons, called "spin-momentum locking", that keeps spin and momentum perpendicular to each other (Figure 2.7a). At thermal equilibrium the bands are symmetric with respect to the origin of the $\boldsymbol{k}$ space so the net spin of the system is zero. The application of an electric field, say, in the positive x direction gives rise to an imbalance of carriers with positive $\boldsymbol{k}_x$ which translates into an imbalance of spin polarized in the y direction thanks to spin-momentum locking. (Figure 2.7b).

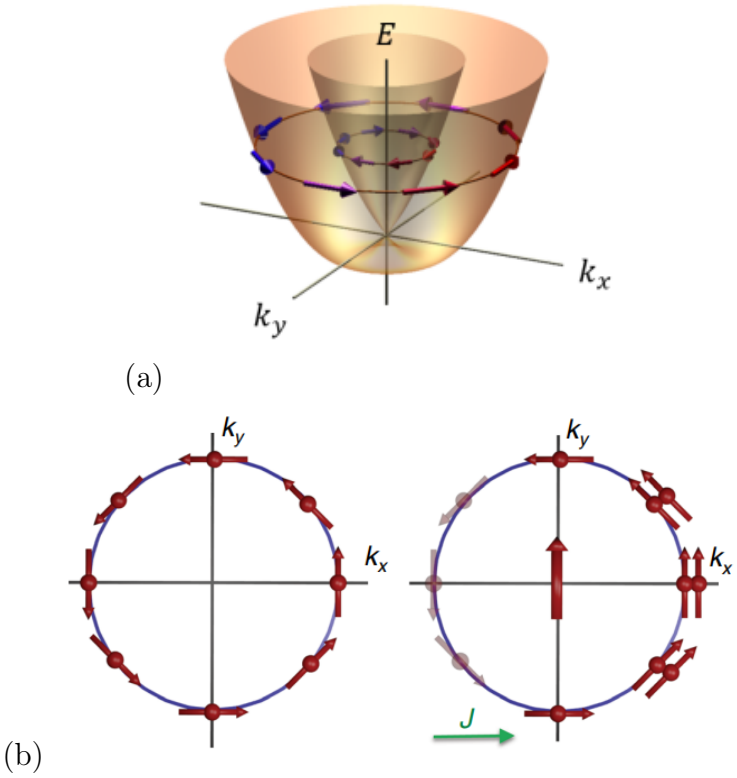

Figure 2.7: (a) The band structure obtained from the Rashba Hamiltonian of Equation 2.44. From Ref. [2]. (b) Left panel: Rashba spin texture for one of the chiral states in equilibrium with zero net spin density. Right panel: nonequilibrium redistribution of eigenstates in an applied electric field resulting in a nonzero spin density due to broken inversion symmetry of the spin texture. From Ref. [43].

This net spin accumulation is associated to a net magnetization $\boldsymbol{\delta m}$ that is able to exert field-like torque $\propto \boldsymbol{\delta m} \times \boldsymbol{M}$ and a damping-like torque $\propto \boldsymbol{M} \times \boldsymbol{\delta m} \times \boldsymbol{M}$ on the magnetization $\boldsymbol{M}$ of an adjacent ferromagnet via exchange interaction [43].
Rashba effect is responsible for the interfacial contribution of SOT. Charge to spin conversion can also arise in the bulk of materials with high SOC primarly thanks to the so called spin Hall effect (SHE) [43].
Spin Hall effect originates from three contributions: intrinsic, skew scattering and side-jump scattering [43]. The intrinsic contribution can be understood considering that, in presence of non negligible spin-orbit coupling the carrier's velocity is not simply proportional to the $\boldsymbol{k}$ derivative of the dispersion relationship $E(\boldsymbol{k})$, but it presents an additional spin dependent anomalous velocity [21].

$$\dot{x} = \frac{1}{\hbar}\frac{\partial E_n(\boldsymbol{k})}{\partial \boldsymbol{k}} + \dot{\boldsymbol{k}} \times \boldsymbol{B}_n(\boldsymbol{k}) \tag{2.40}$$

Where $E_n(\boldsymbol{k})$ is the dispersion relationship of a given band, k is the wave vector and $\boldsymbol{B}_n(\boldsymbol{k})$ a spin dependent parameter.
This anomalous velocity is perpendicular to both the electric field driving the current and the spin polarization of the electrons. As a consequence, considering the reference frame of Figure 2.5, a charge current flowing in the x direction generates a pure spin current polarized in the y direction and flowing in the z one. (Figure 2.8).

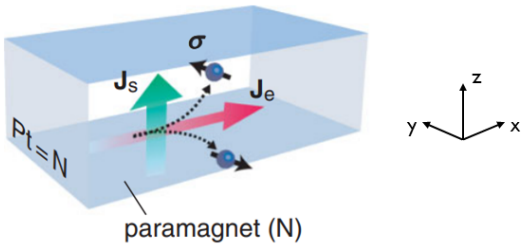

Figure 2.8: Illustration of the charge to spin conversion induced by SHE. From Ref. [35].

What distinguishes the intrisic contribution from the skew scattering contribution is the dependence introduced in the transverse hall conductance $\sigma_{Hall} = \frac{E_{xy}}{j_c}$ on the transport lifetime τ. The first one is related to the anomalous velocity described earlier and it is independent with respect to τ. The second one contributes to σ_{Hall} with a term proportional to τ and it derives from chiral features that appear in the disorder scattering in the presence of spin-orbit coupling [43].
The last contribution is related to the scattering of conduction electrons with impurities having strong spin orbit interaction. In particular, the electron gets deflected, upon scattering, toward a direction perpendicular to both the flowing direction and its spin polarization, thus giving rise to a transverse pure spin current that adds up to the other contributions.
In conclusion, SHE can exploited in heavy metal (HM)/ferromagnet bilayers to induce magnetization reversal without the necessity of a second ferromagnetic layer that polarizes the charge current.
Considering the reference frame of Figure 2.9 and a charge current flowing in the HM along the x direction, SHE induces a spin current polarized along the y direction that exerts both field-like and damping-like torques on the magnetization of the adjacent layer, similarly to what happens for STT, of the form [16]:

$$\boldsymbol{T}_{SOT} = \boldsymbol{T}_{FL} + \boldsymbol{T}_{DL} = \tau_{FL}(\boldsymbol{M} \times \boldsymbol{y}) + \tau_{DL}(\boldsymbol{M} \times (\boldsymbol{M} \times \boldsymbol{y})) \tag{2.41}$$

The current induced torques can be associated to an effective magnetic field acting on the magnetization (Figure 2.9).

$$\boldsymbol{B}_{\perp} \propto \boldsymbol{y} \;\; ; \;\; \boldsymbol{B}_{||} \propto \boldsymbol{M} \times \boldsymbol{y} \tag{2.42}$$

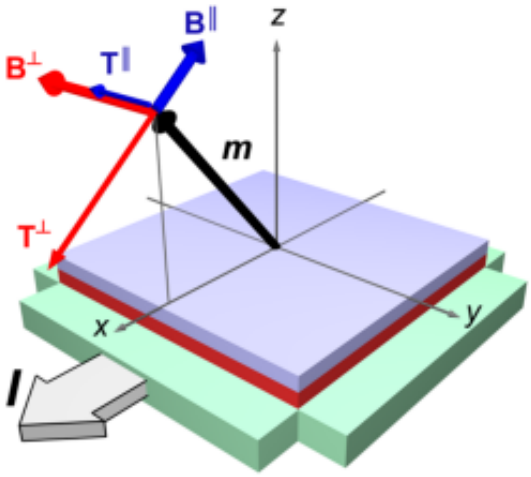

Figure 2.9: Illustration of the current induced torques in a HM/FM bilayer. $T_{||}$ corresponds to the damping like torque while $T_{\perp}$ to the field-like torque. The effective fields are also depicted. Here τ_{FL} and τ_{DL} are assumed to be positive. From Ref. [16].

2.3.3. Anomalous Hall effect

A final remark goes to the observation of anomalous Hall effect (AHE) in ferromagnetic materials. The current in these materials is spin polarized, meaning the number of flowing majority carriers is much larger than the number of minority ones. If charge current is directed along the x axis and the magnetization of the ferromagnet lies along the positive verse of the z axis, then SHE will tend to deflect more carriers toward the $\boldsymbol{x} \times \boldsymbol{z}$ direction rather than toward the $\boldsymbol{x} \times (-\boldsymbol{z})$ one. As a result, a net charge imbalance arises in the y direction that generates a voltage drop detectable experimentally.
This voltage drop adds up to the one related to the ordinary Hall effect and the overall transverse resistance can be described by the following empirical formula [34]:

$$\rho_{xy} = R_0 H_z + R_s M_z \tag{2.43}$$

Where ρ_{xy} is the transverse resistivity, R_0 is the ordinary Hall resistivity and R_s is the anomalous Hall resistivity.

The anomalous Hall contribution can be ten times larger than the ordinary one and therefore it can be efficiently exploited to electrically detect the out of plane magnetization of a system. It is in fact the method used to monitor the magnetization state of devices studied in this thesis since they posses perpendicular magnetic anisotropy.

To conclude, the theoretical concepts introduced in this chapter are necessary to understand the physical origins of the phenomena exploited and described in this thesis.
First, the mechanisms behind the arising of perpendicular magnetic anisotropy in thin films are clarified.
Afterwards, the explanation behind the high TMR obtained in Fe/MgO/Fe multilayers is provided. The same working principle governs the magnetotransport characteristics of the CoFeB/MgO/CoFeB magnetic tunnel junctions studied in this thesis.
The second part of this work deals with magnetization writing via SOT. For this reason in this chapter the mechanism of magnetization manipulation by means of spin currents is exposed and their spin-orbit coupling origin is introduced with the spin-Hall effect.

3 | Experimental methods

3.1. Growth and fabrication

3.1.1. Magnetron sputtering

Magnetron sputtering is a technique aimed at growing high quality thin films of several materials, insulating or conducting, magnetic or not, even with high melting point, by means of an eroding plasma. It belongs to the more general class of plasma assisted physical vapour deposition techniques [47]. To understand the working principles of sputtering, let us consider a scheme consisting in a capacitor-like structure inside a vacuum chamber and a gas, usually argon, pumped inside. If the voltage applied to the electrodes overcomes a threshold, known as breakdown voltage, the normally insulating gas starts conducting and current begins to flow through the gas and the electrodes. This occurs when the free electrons, always present in a gas, reach an energy high enough to ionize the neutral argon atoms. The electrons and the Ar^+ ions travel in different directions meaning that a net current flows. Increasing the voltage a situation is reached in which the ionization is self-sustained and in this case a plasma is formed.
Plasma is then confined by electric and magnetic fields having their lines respectively perpendicular and normal with respect to the electrode's surface. In this way the ions follow a trajectory directed as $\boldsymbol{E} \times \boldsymbol{B}$, close to circular orbits. If the ions have enough energy, their impact with a solid surface can extract atoms from it and the effect is enhanced by the confinement provided by the magnetic field [47].
The extracted atoms are deposited on the substrate and contribute to the growth of the film.
Sputtering guarantees high quality films in terms of uniformity, adhesion and grain sizes thanks to the high energy with which atoms arrive onto the substrates' surface. Their high mobility infact allows them to migrate on the surface and arrange in the lowest energy configuration.
Moreover, thickness control down to a fraction of a nm is obtainable thanks to the low deposition rates, in the order of 1 $\frac{nm}{min}$.

The instrument employed to grow films by magnetron sputtering is an AJA ATC Orion 8 Sputtering System, developed by AJA International Inc. It is endowed with ten 2"/1" DC or RF targets arranged in a confocal sputtering-up configuration, including MgO, Ta, Ru, $Co_{40}Fe_{40}B_{20}$, Pt, Co, IrMn, AlO_2, NiFe. RF targets are dedicated to oxides, since no direct current can flow through them, while DC targets to metals.
The substrate can be heated up to 800 °C and, if desired, mounted on an in-plane magnetized holder. A Cryo Vacuum Pumping system allows base pressure in the range 10^{-9} Torr while a load-lock decouples the main chamber from the outside during the un/loading of samples. Deposition rates are evaluated both using the quartz crystal microbalance positioned in place of the sample and by growing a reference specimen whose thickness is measured with atomic force microscope. Before every deposition, samples undergoes a process of soft etching by igniting the Ar plasma to clean the surface from contaminants; the plasma is striken delivering 20 W to the sample holder.

3.1.2. Thermal annealing

Thermal annealing is a widely employed process used to improve the material quality and to modify or strengthen the properties of materials. It consists of the slow heating and the subsequent slow cooling of the specimen, sometimes in presence of a magnetic field if a particular magnetic configuration is required. Keeping a solid at high temperature allows the atoms to rearrange toward their proper and stable locations to ehnance crystalline order. In the present work, thermal annealing of the duration of around an hour at temperatures ranging from 250°C to 350°C is needed in order to let the interface between CoFeB and MgO crystallize and the orbitals hybridation responsible for the formation of perpendicular magnetic anisotropy arise. An out of plane magnetic field of is usually applied during the process to help the spins to allign along the desired direction. As shown in Section 4.1.2, thermal annealing is mandatory to obtain PMA.
The process is carried out in a vacuum annealing system consisting of a vacuum chamber pumped by a turbopump ensuring operating pressures lower than 10^{-4} mbar. The sample is mounted on a ceramic bar, thermally conductive, in contact with a resistive filament. The filament temperature is raised by Joule heating and controlled by a PID controller. The rate of increase of the temperature, its final value and the dwell time can all be set through the controller. Vacuum is needed to avoid contamination of the sample and to preserve the heating filament. A uniform magnetic field of 4 kOe can be applied either in plane or out of plane by means of an external permanent magnet sorrounding the vacuum chamber.

3.1.3. Optical lithography

Lithography is a well established technique in which a 2D pattern is projected onto the sample surface from a model, the mask, thanks to the esposition to UV light. The mask consists in a transparent quartz substrate covered by Cr on the regions defining the desired pattern and it is positioned in close proximity with the sample during the process [33].
The sample is covered by an impressionable polimer, the photoresist, that allows the transfer of the mask's features upon exposition to light. When the substrate is illuminated, in fact, the regions of photoresist not protected by light undergo a chemical reaction that can either make the polymer more resistant of weaker. In the first case, the photoresist not exposed to light is easily removed while in the second case the the exposed photoresist can be stripped off. In both cases the result is the definition of the desired pattern on the sample.
Lithography generally starts from covering with a proper resist the sample, after it has been cleaned properly. The photoresist is initially liquid and it is therefore distributed on the surface by spin coating. The rotation speed and the spinning time can be adjusted to obtain the required thickness. The resist then solidifies thanks to a soft bake on a hot plate that makes its solvent evaporate.
Lithography can be of two types, direct or inverse: in the former case the exposed region is developed while in the latter case it is the region not exposed to the beam which is removed [33]. By definition, a positive resist is employed for direct lithography. In this case, the exposure breaks the chemical bonds of the resist and induces the solvability of the exposed areas which can thus be removed during the development. The development is accomplished by rapidly agitating the sample within a proper solvent; its duration is another parameter which needs to be calibrated. On the contrary, inverse lithography requires a negative resist or image reversal if an invertible positive resist is used. When adopting a negative photoresist, the unexposed regions are developed and eliminated. Instead, in the latter situation, the procedure involves more steps required to reverse the property of the resist, i.e. to make the exposed regions unsolvable and the unexposed ones solvable.
Figure 3.2 summarizes the main steps of direct lithography.

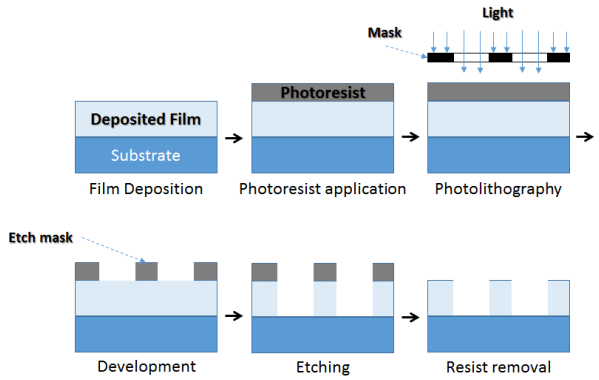

Figure 3.1: Illustration of the steps involved in direct lithography. After the resist development the etching step and the resist removal, which are going to be discussed later, are included. Adapted from Ref. [34]

The manual Karl Suss Mask Aligner MA6/BA8 is used to perform optical lithography needed to define the magnetic tunnel junctions. The machine is provided with a 1000 W mercury arc lamp emitting at 365 nm and provides 5.1 $\frac{mW}{cm^2}$ as intensity on the stage. The required dose, (energy per unit surface), and the intensity determine the exposition time of the resist. Spin coating was realized by means of the Karl Suss Spin Coater RC8 which permits rotation velocities as high as 7000 rpm. The positive resist used for all lithographic processes is the AZ5214.
A Heidelberg Tabletop Maskless Aligner 100 (MLA) is used for the Hall bars used to investigate SOT switching. The instrument permits the fabrication of micrometric structures by means of layouts designed for the purpose using the software Layout Editor. The esposition occurs by local esposition of the layout regions by means of a LED laser, which allows precision down to 1 μm.

3.1.4. Ion beam etching

Ion beam etching is a physical dry technique used to remove atoms from the surface of a material by means of accelerated Ar^+ ions.
It involves a filament (cathode) which, thanks to Joule heating, emanates electrons by thermoionic emission. The emitted electrons are then accelerated by the discharge voltage through an Argon gas. Electron with high enough energy can ionize Ar atoms and a current comprising electron and Ar ions arises: the latter are accelerated towards the sample and remove material from its surface, while the former contribute to sustain the ionization process.
The instrument employed is the Ion Beam Etching Kenosistec VS80, provided with a main

chamber and a load lock system kept at around 10^{-8} and 10^{-6} mbar, respectively. The Ar base pressure during operations was about 3.5 $\times 10^{-4}$ mbar while the beam accelerating voltage and the beam current were 200 V and 50 mA respectively. The sample holder is kept in rotation to ensure uniform sputtering and was tilted 30° away from the incident beam to prevent re-deposition of the etched material.
Typical etching rates of the material used in this thesis are in the order of 2-3 $\frac{nm}{min}$.

3.2. Sample characterization

3.2.1. Vibrating sample magnetometry

The Vibrating Sample Magnetometer (VSM) is an instrument able to extract the magnetic properties of a sample which exploits classical electromagnetic induction due to the movement of the magnetic sample. The sample is placed within a uniform magnetic field, whose magnitude can be varied within the range of a few Tesla, and put into vertical sinusoidal vibration. Its magnetic moment, either intrinsic or induced by the field, produces a stray field which oscillates in time.
Two pick-up coils are used to convert the oscillating magnetic flux into an electric field proportional to the magnetic moment owing to the Faraday-Newmann-Lenz effect described by the equation:

$$f = -\frac{\partial \phi}{\partial t} \tag{3.1}$$

Where f is the induced electromotive force, ϕ the magnetic flux.
The signal is detected by means of a lock-in amplifier which demodulates the input using the signal driving the sample's oscillation.

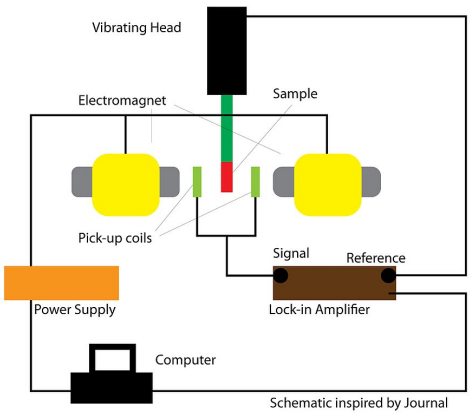

Figure 3.2: Simplified VSM schematics. From Ref. [23].

The instrument used throughout this work is a VSM model EZ-9 produced by Microsense, LLC. A uniform magnetic field up to 2.25 Tesla can be applied, the 360° rotation of the sample is fully automatized while an oven/cryostat system supports operations in the temperature range from 100 K to 1000 K. The minimum detectable magnetic moment is $\simeq 1\ \mu emu$.

3.2.2. Atomic force microscope

Atomic force microscope (AFM) is a technique for surface and geometrical characterization of samples. It provides three dimensional reconstruction of surfaces with subnanometer vertical resolution over the range of few hundreds of micrometers.
AFM belongs to the family of scanning probe microscopy (SPM), a branch of microscopy which allows the characterization of surfaces by means of a physical probe that interacts with it. In the particular case of AFM, the tip scanning the sample interacts with its surface via weak interatomic forces called Van der Waals forces.
The image is formed by moving the probe over the sample in a raster fashion ("zig-zag" motion), provided by a piezoelectric actuator which provides nanometric precision in all three spatial directions.
The probe motion sensor controls the force acting between the tip and the surface and it feedbacks a correction signal aimed at keeping the distance or the force between tip and sample costant.
In particular, as the tip is scanned over the sample or the sample is scanned over the tip, the forces between the two deflect the cantilever on which the tip is mounted and this movement is quantified by means of a system composed by a laser and a photodiode. The laser beam is directed towards the cantilever, which reflects it in the direction of the photodiode. During scanning, the z-displacement causes a cantilever flection which reflects on a variation of the signal acquired by the photosensor. This signal variation is fed to a servo systems that acts on the cantilever keeping the force or the distance between the tip and the sample constant (Figure 3.3).

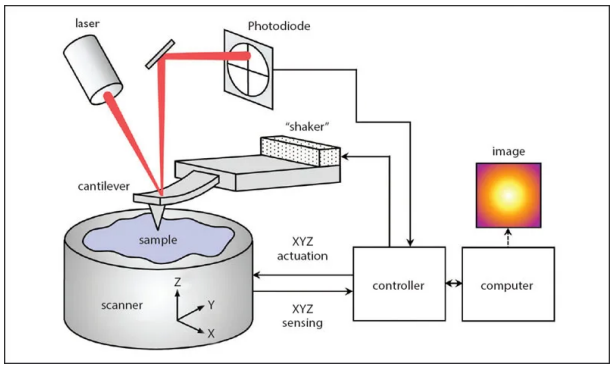

Figure 3.3: Illustration of an AFM comprising the tip, the scanner, the laser-photodiode system and the feedback loop. Adapted from Ref. [1].

The two most common AFM imaging modes are the tapping (or dynamic) mode and the contact (or static) mode. In the former case, the tip is externally driven into oscillations with a given amplitude and frequency; interactions with the surface result in variation of the resonant frequency and therefore of the actual amplitude of oscillation, detected by means of the deflection. This signal is used to reconstruct the topography and it is used by the feedback loop to keep the tip oscillation amplitude constant, varying the height of the tip.
In static mode the tip is always in contact with the surface and during the scan it bends to follow the topography. In particular, when it touches the surface the strong atomic repulsive forces tend to push it away. This time the feedback circuit does not act on the amplitude but on the deflection, which is kept as close as possible to the reference point so as to maintain the repulsive force unchanged.
A Keysight 5600LS AFM system has been used for all the scanning microscopic operations executed during the thesis, namely roughness analysis and thickness measurement.

3.2.3. Transport measurements setup

Most of the experimental results presented in this thesis work were obtained from electrical transport measurements. For this reason here I provide a description of the setups used for the different experiments.
The assessment of the TMR in magnetic tunnel junctions is performed using a probe station available in our laboratory. It is composed by four metallic tips attached to a handler which allows movement in three dimension with micrometric precision. The sample under test is positioned on a sample holder which is placed in the middle of the four probes. The procedure of putting the tips in contact with the substrate is monitored thanks to an optical microscope mounted at an adjustable height above the sample.

The tips are connected via coaxial cables to the measurement instruments, namely a Keithley 2611 current source and a Keithley 2600 nanovoltmeter. During the resistance measurement, performed in four contacts configuration (explained in Section 4.3), the first is used to inject the probing current while the second is used to detected the resulting voltage.
The out of plane magnetic field needed to investigate TMR is generated by means of a solenoidal electromgnet placed underneath the sample and powered by a Kepco Bop current generator. A hall probe is used to quantify the field to current ratio, found around 45 $\frac{Oe}{A}$ for this particular configuration, and to verify the absence of a non negligible in plane component of the field.
The experiments of SOT induced switching are performed on a different setup. As pointed out in Section 5.2, in this case the devices were bonded to a PCB in order to minimize noise and disturbances. The PCB is provided with 8 metallic pins that allow the connection of two devices. The pins connect the PCB to a holder that contains the wiring responsible for the electrical connections between the instruments, namely Keithley 2600 nanovoltmeter and Keithley 2611B sourcemeter, and the devices. The Keithley sourcemeter is preferred this time since it is offers the possibility of sending voltage pulses with duration down to 500 μs needed to induce SOT switching.
The holder is placed between the poles of an electromagnet providing a field to current ratio of around 890 $\frac{Oe}{A}$, whose lines are parallel to the plane of the sample. The holder is finally connected to a stepper motor controlled remotely via ArduinoUno controller that allows the sample rotation around the out of plane axis.
Finally, all the instruments are controlled remotely by means of a matlab script which sends commands via GPIB bus.
When a particular precision in the cancellation of the spurious out of plane component of the field is required, the setup is modified in order to allow rotation of the sample around the axis in the plane of the sample perpendicular to the external field's lines. This rotation, in fact, influences the projection of the external field on the out of plane direction of the sample, whose magnitude can be monitored via AHE measurement.

4 | Fabrication and characterization of magnetic tunnel junctions with perpendicular magnetic anisotropy

Magnetic tunnel junctions with perpendicular magnetic anisotropy (PMA), i.e. with easy axis of both layers perpendicular to the interfaces, are widely used in applications, mainly due to the better confinement of the magnetic stray field from the magnetic layers, thus allowing to increase the device density on the chip. This class of MTJs with PMA, pMTJs from now on, is also used to implement the current driven magnetization switching by SOT, by growing the magnetic layer on top of a heavy metal, topological insulator or Rashba system where charge current is injected.
In this chapter I describe the optimization of Ta/CoFeB/MgO/Ta pMTJs where the bottom CoFeB acts as free layer and Ta as heavy metal performing the charge-to-spin conversion giving the SOT.
This is the first step towards the implementation of SOT-pMTJs for unconventional computing, which is the general framework of this thesis.

4.1. Deposition and characterization of the magnetic stack

4.1.1. Materials and thicknesses choice

At the beginning of my thesis a well-established protocol for fabricating pMTJs was not available in the NaBiS group. The well known Ta/Ru/Ta/CoFeB/MgO/CoFeB/Ta/Ru stack is chosen to realize the device, owing to the various reports of high quality junctions

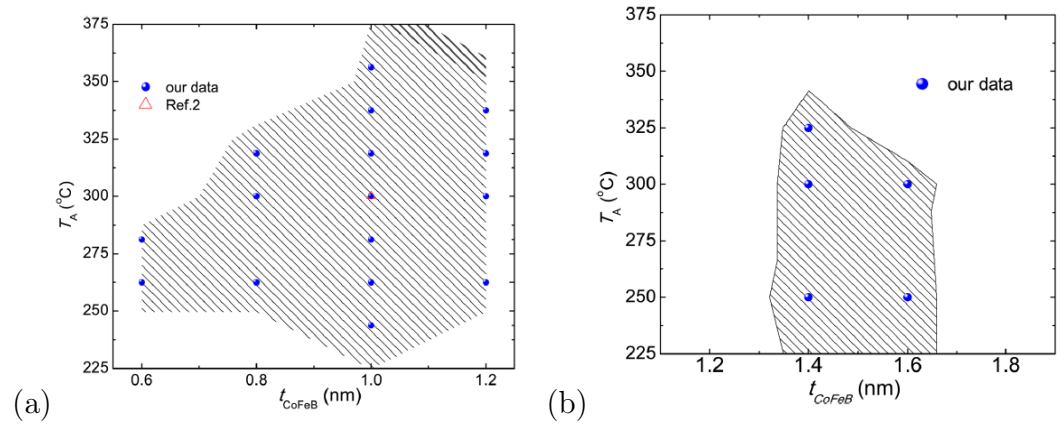

Figure 4.1: Phase diagram of the dependence between the CoFeB thickness and the annealing temperature of the Ta/CoFeB/MgO structure (a) and of the MgO/CoFeB/Ta strucure (b). The figures taken from Ref. [52] show by dashed area the combination of CoFeB thickness and annealing temperature giving PMA. Blue dots represents our experimental data from many samples during the optimization, while the red triangle of (a) represents a data taken from a different reference used by the author as a comparison [52].

resulting from it, when deposited by magnetron sputtering and treated with thermal annealing to promote the crystallization of the interfaces between CoFeB and MgO [12, 18].

The thicknesses of the various layers are chosen according to the studies conducted by S.Ikeda *et al.* [18] and by W.Wang *et al.* [52].

The latter reports, for the bottom CoFeB layer, good PMA with thickness between 0.6nm and 1.2 nm, with 1nm being appropriate over the largest range of annealing temperatures inducing the transition of the magnetization from in plane to out of plane (see the dashed area of Figure 4.1a). We performed a careful optimization of the CoFeB thickness and annealing temperature corresponding to the experimental points (blue dots) in Figure 4.1a. Our data are in good agreement with [52]. For this reason and based on other authors' indications [12, 18], 1 nm is chosen as the thickness of the bottom CoFeB layer.

Regarding the upper CoFeB, Wang *et al.* [52] observe a magnetic dead layer around 0.5 nm thick in the structure MgO/CoFeB/Ta, caused by the interdiffusion of tantalum in the magnetic film during the thermal annealing (see below).

For this reason the optimal range for the top layer's thickness turns out to be between 1.3 nm and 1.7 nm, and 1.4 nm is chosen again since it has the largest range of allowed annealing temperatures (Figure 4.1b).

The oxide barrier needs to be thin enough to allow effective tunneling, but thick enough to

guarantee the formation of an uniform layer despite the possible irregularities introduced by the sputtering process, therefore a thickness of 2 nm is selected.
For the Ta/Ru/Ta buffer layer and for the capping Ta/Ru layer the thicknesses are the same adopted by S.Ikeda *et al.* [18].
All the thicknesses after optimization are listed in Table 4.1

Material	Thickness(nm)
Ru	5
Ta	5
CoFeB	1.4
MgO	2
$Co_{40}Fe_{40}B_{20}$	1
Ta	5
Ru	10
Ta	5

Table 4.1: Thicknesses of the Magnetic stack's layers

4.1.2. Deposition and magnetic characterization

The problem of obtaining PMA in the entire heterostructure under exam is addressed studying the stacks containing only the top or the bottom CoFeB layers, separately.
First, the structure Ta(5)/Ru(10)/Ta(5)/CoFeB(1)/MgO(2)/Ta(5)/Ru(5) is prepared on a thermally oxidized silicon substrate by magnetron sputtering at room temperature using the AJA ATC Orion 8 sputtering system available at PoliFab.
The silicon specimen is initially covered by a layer of protective coating used during the dicing of the wafer to obtain 10x10 μm^2 samples, which is removed with 1 min. of ultrasound bath in acetone followed by the 1 min. of ultrasound bath in IPA.
The surface is then analyzed first with an optical microscope, to ensure that all the protective coating was correctly removed, and then with AFM, to verify that the substrate's roughness is low enough to accomodate a uniform thin film. As Figure 4.2 shows, the substrate's root mean square (RMS) roughness, estimated around 0.3 nm, is well below the thickness of the Ta/Ru/Ta buffer layer and also of the MgO barrier.
Anyways, as a precaution, a 10 min. soft etch step (20 W, 30 mTorr) is included in every deposition to flatten the surface in case of unexpected irregularities.
Once the substrate's preparation is over, the magnetic stack is deposited with magnetron

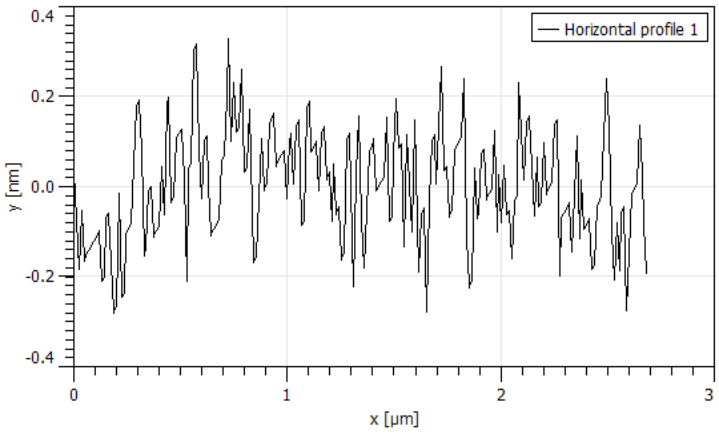

Figure 4.2: AFM profile showing the roughness of the thermally oxidized silicon wafer used for the deposition

sputtering using AJA ATC Orion 8 sputtering system. All the deposition rates used refer to a calibration performed right before the beginning of the depositions involved in this study. The rates, as well as the deposition conditions, are listed in Table 4.2.

Material	mode	Deposition rate(nm/min)	Ar pressure (mTorr)	Power (W)
Ru	DC	2.20	5	50
Ta	DC	4.53	3	100
$Co_{40}Fe_{40}B_{20}$	DC	1.2	3	60
MgO	AC	0.32	2.2	220

Table 4.2: Deposition rates of Ta,Ru,CoFeB and MgO with the sputtering system AJA ATC Orion 8

In plane and out of plane VSM measurements are then recorded before and after the thermal annealing procedure, of the duration of 1 hour at 250°C, performed under the action of an external out of plane magnetic field of around 300mT generated by a permanent magnet.
Figure 4.3 displays the out of plane (OOP) VSM results before (Figure 4.3a) and after (Figure 4.3b) the annealing process.

It is clear that the latter is crucial for the arising of perpendicular anisotropy since, while the as-deposited sample exhibits a cycle compatible with an in plane easy axis, in the thermally treated one the squared hysteresis appears, meaning the easy axis points now in the out of plane direction.
Table 4.3 lists the saturation magnetization and the coercive fields observed. Note that

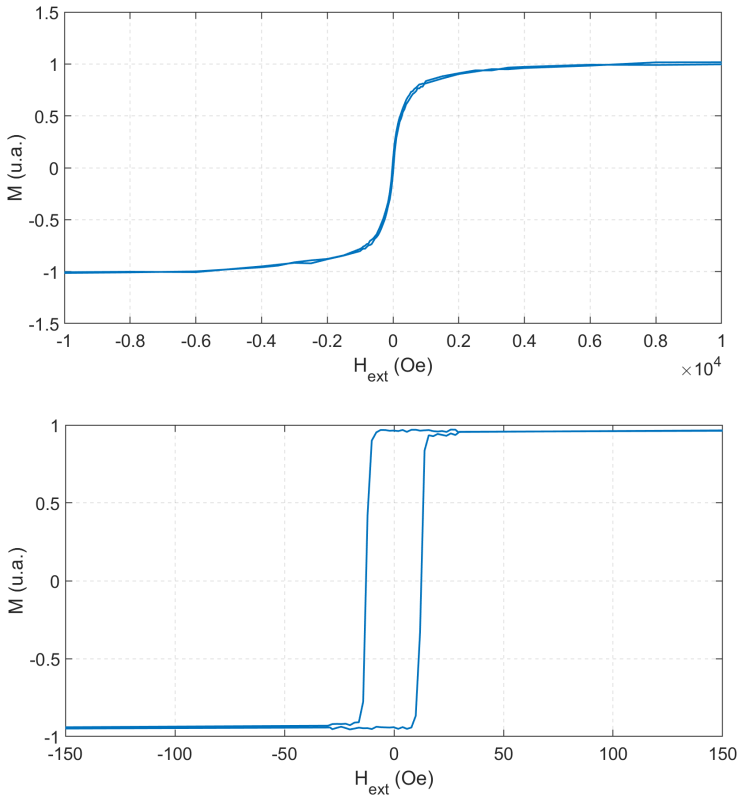

(a)

(b)

Figure 4.3: Out of plane hysteresis loop of the Ta(5)/Ru(10)/Ta(5)/CoFeB(1)/MgO(2)/Ta(5)/Ru(5) structure before(a) and after(b) the thermal annealing process at 250 °C. The squared loop present in the second case indicates that the annealing process is crucial for the arising of PMA.

the VSM measurement outputs the total measured magnetic moment, rather than the magnetization, as a function of the applied field. Therefore, in order to retrive the usual M-H loop, one has to divide the magnetic moment by the volume of the ferromagnet that generates it.

Coercive Field(Oe)	Saturation magnetization($\frac{A}{m}$)
12.5 ± 1	$7.34 \times 10^5 \pm 1 \times 10^4$

Table 4.3: Coercive field and saturation magnetization of the Ta(5)/Ru(10)/Ta(5)/CoFeB(1)/MgO(2)/Ta(5)/Ru(5) structure post annealing (bottom layer)

The coercive field is coherent with what observed by Wang *et al.* [52], who report a value around 13 Oe, while the saturation magnetization is lower than the one mainly reported in literature, equal to $10^6 \frac{A}{m^2}$ or larger [18, 42, 52].
The discrepancy might be explained with the presence of an large magnetic dead layer (MDL) caused by the interdiffusion of tantalum into CoFeB during both the deposition and the thermal treatment [42].
The thickness of this magnetic dead layer can be estimated with the following equation, taking as a reference the saturation magnetization found by Ikeda *et al.*, equal to $1.26 \times 10^6 \frac{A}{m}$ [18].

$$t_d = t_{CoFeB}(1 - \frac{M_s^{meas}}{M_s^{ref}}) = 0.53nm \tag{4.1}$$

where t_d is the MDL thickness, t_{CoFeB} is the CoFeB thickness, M_s^{meas} is the saturation magnetization retrived experimentally and M_s^{ref} is the reference saturation magnetization.

The same described steps are followed to study the structure containing the top CoFeB layer.
The stack Ta(5)/Ru(10)/Ta(5)/MgO(2)/CoFeB(1.4)/Ta(5)/Ru(5) is deposited and annealed, yelding the OOP hysteresis cycle of Figure 4.4.

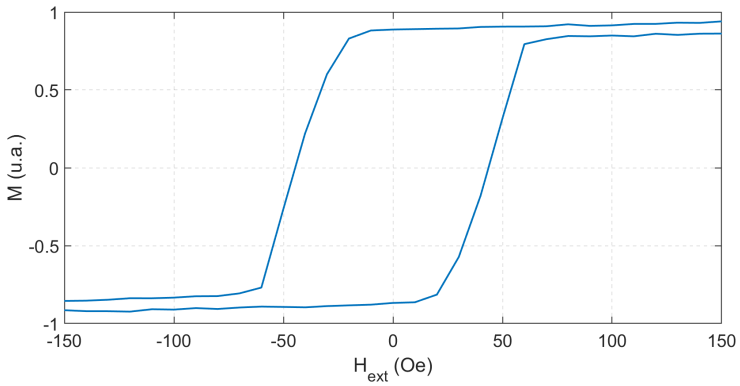

Figure 4.4: Out of plane hysteresis loop of the Ta(5)/Ru(10)/Ta(5)/MgO(2)/CoFeB(1.4)/Ta(5)/Ru(5) structure after the thermal annealing process.

The squareness of the cycle and the high remanence magnetization indicate the presence of a strong PMA here as well.
Table 4.4 displays the main magnetic parameters.

Coercive Field(Oe)	Saturation magnetization($\frac{A}{m}$)
43 ± 1	$6.34 \times 10^5 \pm 1 \times 10^4$

Table 4.4: Coercive field and saturation magnetization of the Ta(5)/Ru(10)/Ta(5)/MgO(2)/CoFeB(1.4)/Ta(5)/Ru(5) structure post annealing (Top layer).

Some considerations can be made comparing coercive field and saturation magnetization of top and bottom layers.
First of all, the saturation magnetization retrieved by the VSM measurement is slighlty larger in the bottom layer. This is coherent with the reports in literature of a more important dead layer taking place in the MgO/CoFeB/Ta rather than in the opposite sequence, caused by the "bombardment" effect of Ta heavy atoms hitting lighter CoFeB atoms during deposition, which creates a large number of magnetic defects at the interface.
In this case, in fact, the application of Equation 2.1 yelds a value for the dead layer thickness of around 0.99nm, always using the reference magnetization of Ref. [18].
The smaller effective thickness of the top layer CoFeB is expected however to have beneficial effects on the strength of PMA, as it can be deduced from the formula of the effective anisotropy constant K of the film [18]:

$$K = K_b - \frac{M_s^2}{2\mu_0} + \frac{K_i}{t_{CoFeB}} \tag{4.2}$$

where K_b is the bulk PMA constant, M_s the saturation magnetization, μ_0 the magnetic permeability of vacuum, K_i the interfacial PMA constant and t_{CoFeB} the CoFeB thickness.
The higher coercive field of the top layer structure observed experimentally is consistent with Equation 4.2 showing that K is inversly proportionaly to the CoFeB thickness.

After the desired magnetic properties of the single layers are obtained, the full heterostructure can be deposited and studied.
Figure 4.5 displays the out of plane hysteresis loop of the film Ta(5)/Ru(10)/Ta(5)/CoFeB(1)/MgO(2)/CoFeB(1.4)/Ta(5)/Ru(5), recorded after the usual annealing process of 1 hour at 250°C with applied out of plane field of 300 mT.

(a)

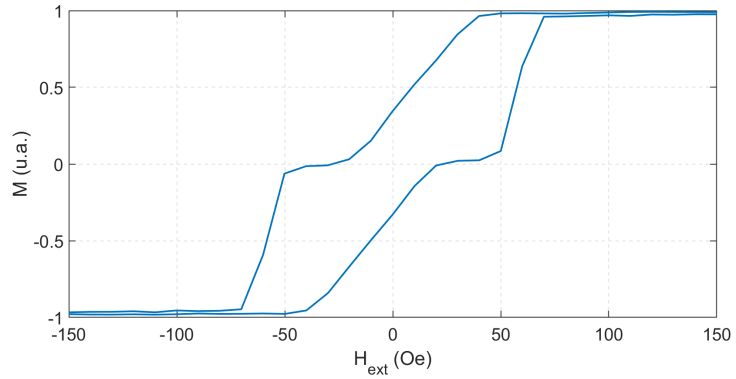

(b)

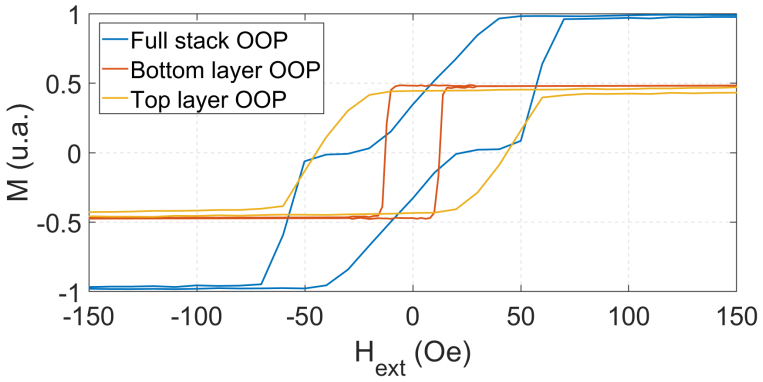

Figure 4.5: Out of plane hysteresis loop of the Ta(5)/Ru(10)/Ta(5)/CoFeB(1)/MgO(2)/CoFeB(1.4)/Ta(5)/Ru(5) structure(a) and the confrontation of the latter with the OOP cycles of the single layers(b).

The distinct contributions of the two layers are visible, but while one preserves its PMA, the other shows a partially in plane anisotropy, as the first smooth magnetization reversal and the low remanent magnetization suggest.
By comparison with the loops of the single layers (Figure 4.5b) it can be deduced that it is the bottom layer the one which loses its PMA character, as the cycle relative to the top CoFeB matches almost perfectly the second transition of the full stack's cycle, meaning that its anisotropy is fully preserved.
PMA gets spoiled only after the two layers are in the full structure. Weng *et al.* [53] report a loss of PMA in the bottom layer of the Ta/CoFeB/MgO/CoFeB/Ta heterorostructure as the annealing temperature grows over a certain threshold, as it is displayed in Figure 4.6. This suggests that in the complete structure interdiffusion of tantalum, which is favoured by high temperatures, has a stronger influence over the magnetic properties of the system. The cause of this behaviour might be ascribed to a non optimal control of the annealing temperature, which might be higher than expected. In the same article, the presence of an interlayer exchange interaction which shifts the bottom layer's magnetization reversal is also studied. This might also play a role in determining the magnetic properties of the structure addressed in this thesis, but further studies are required to verify this hypothesis.

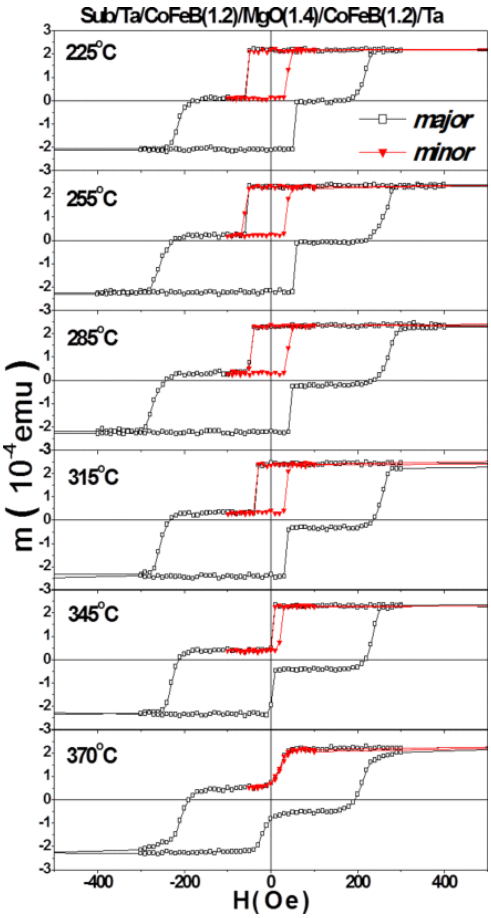

Figure 4.6: Hysteresis loops recorded in Ref. [53], including both the full loops and the minor loops, of CoFeB/MgO(1.4 nm)/CoFeB measured by the external field along the perpendicular direction after the annealing temperature varied from 225 C to 370 C. The cycle measured after the annealing at 370°C is similiar to the one measured in this thesis.

Despite the non optimal PMA of the bottom layer, the hysteresis cycles shows the presence of a range of fields in which top and bottom layers are magnetized in antiparallel directions, which is what is needed to observe TMR. Moreover, as explained in Section 4.2, an enhancement of PMA is expected after patterning.
For these reasons and for a matter of time we decided to use this full structure to proceed with the fabrications of the perpendicular magnetic tunnel junctions.

4.2. Perpendicular magnetic tunnel junctions fabrication

In the following section the process aimed at realizing the perpendicular magnetic tunnel junctions is described in all its phases.
It consists on the sequence of 3 lithographic steps carried out using a lithographic mask already available in the research group. The first two steps are of direct lithography and therefore involving etching, while the last on is of inverse lithography thus involving lift-off. The mask covers a surface of a 5 inches wafer and it contains, among the others, three 20x20 mm^2 sections comprising the patterns for the lithograpic steps, arranged as in Figure 4.7.

	4	1	1	3	3	7	
6	5	1	1	3	3	8	9
2.B	2.B	2.B	2.B	16.B	16.A	17.B	16.A
2.A	2.A	2.A	2.A	16.D	16.C	17.D	16.A
10.A	10.B	19.A	19.B	19.E	19.F	18.C	18.D
10.C	10.D	19.C	19.D	19.G	19.H	18.A	18.B
10.E	19.A	19.I	12.B	12.C	12.F	13	Carpene
	12.A	12.D	12.E	12.G	12.A	Grids	

Figure 4.7: Summary of the layout of the lithographic mask. The red, green and blue regions correspond to the areas dedicated to contacts, MESA and junction regions used in this work, as better explained later.

Each section contains the patterns for 144 devices, with junctions' areas ranging from $4\mu m^2$ to $1600\mu m^2$, both rectangular and elliptical with different aspect ratios. Figure 4.8 lays out the organization of each section.

2.A	A	B	C	D	E	F	2.A	G	H	I	J	K	L
1	40x4	40x8	40x20	20x20	4x4	30x30	1	10x10	40x2	8x2	8x2	2x2	10x10
2	30x4	30x8	30x20	15x2	15x15	8x8	2	40x2	30x2	4x2	4x2	10x10	2x2
3	20x4	20x8	15x2	30x30	2x15	40x40	3	30x2	20x2	2x2	5x5	2x4	2x8
4	15x4	15x8	15x15	2x15	20x30	20x40	4	20x2	15x2	10x10	2x2	2x4	2x8
5	8x4	30x30	8x15	8x20	8x30	8x40	5	15x2	5x5	2x15	2x20	2x30	2x40
6	15x15	4x8	4x15	4x20	4x30	4x40	6	10x10	2x15	2x20	2x30	2x40	10x10
2.B	A	B	C	D	E	F	2.B	G	H	I	J	K	L
7	10x10	40x2	8x2	8x2	2x2	10x10	7	40x4	40x8	40x20	20x20	4x4	30x30
8	40x2	30x2	4x2	4x2	10x10	2x2	8	30x4	30x8	30x20	15x2	15x15	8x8
9	30x2	20x2	2x2	5x5	2x4	2x8	9	20x4	20x8	15x2	30x30	2x15	40x40
10	20x2	15x2	10x10	2x2	2x4	2x8	10	15x4	15x8	15x15	2x15	20x30	20x40
11	15x2	5x5	2x15	2x20	2x30	2x40	11	8x4	30x30	8x15	8x20	8x30	8x40
12	10x10	2x15	2x20	2x30	2x40	10x10	12	15x15	4x8	4x15	4x20	4x30	4x40

Figure 4.8: Layout of the section containing the patterns for the junctions' pillars. Each cell in the table indicates the dimensions of the pillars in μm^2. The white part of the table includes the elliptic devices, while the other the rectangular ones.

The process begins with the deposition, via magnetron sputtering using the usual AJA ATC Orion 8, of the following stacks:

- Ta(5)/Ru(10)/Ta(5)/CoFeB(1)/MgO(2)/CoFeB(1.4)/Ta5)/Ru(5) on a 20x20 μm^2 thermally oxidized silicon substrate used for the fabrication of the devices after the thermal annealing process;
- Ta(5)/Ru(10)/Ta(5)/CoFeB(1)/MgO(2)/CoFeB(1.4)/Ta5)/Ru(5) on a 10x10 μm^2 thermally oxidized silicon substrate used for the AFM check of the second etching step;
- Ta(5)/Ru(10)/Ta(5)/CoFeB(1)/MgO(2)/CoFeB(1.4)/Ta5)/Ru(5) on a glass substrate used to control the first etching step;
- CoFeB(1)/MgO(2)/CoFeB(1.4)/Ta5)/Ru(5) on a glass substrate used to control the second etching step.

The aims of all these samples, here just mentioned, will be discussed in detail later.
Once the Ta(5)/Ru(10)/Ta(5)/CoFeB(1)/MgO(2)/CoFeB(1.4)/Ta5)/Ru(5) stack is annealed and its magnetic properties are verified, the first lithographic step is carried out, in which the MESA region is defined. The MESA region includes the area covered by the bottom contacts, (500x500 μm^2) and by the channel containing the junction (250x50 μm^2), as depicted in Figure 4.9.

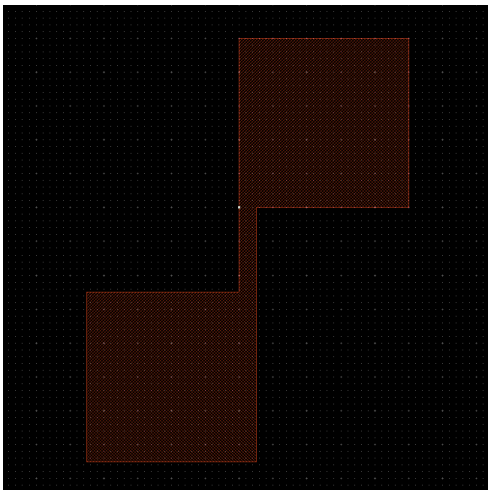

Figure 4.9: Reproduction of the MESA with the software Layout Editor.

First, photoresist AZ5214 is spin-coated on the sample by means of the spincoater Karl Süss RC8. The photoresist, initially liquid, solidifies after a soft bake on a hot plate that makes the solvent evaporate. The wanted pattern is then transferred on the sample by

Photoresist	Spinning	Soft bake	Expected thickness
AZ5214	6000 rpm 60 s	120°C 90 s	1.4 μm

Table 4.5: Parameters of the spin coating and soft bake procedure.

Energy density ($\frac{mJ}{m^2}$)	Lamp dose ($\frac{mW}{m^2}$)	Exposition time (s)	Al.gap (μm)
288	3.5	82.3	60

Table 4.6: Parameters of the lithographic exposure.

means of the mask alligner Karl Süss MA6/BA8. The exposition parameters are reported in Table 4.6. Being the machine provided with a wafer holder 5 inches large, the specimen is glued to a dummy 5 inches wafer with a drop of photoresist. The sample is then dipped in AZ726MIF developer for 30s in order to remove the exposed photoresist. A water bath is finally needed to stop the development process.
Figure 4.10 shows the optical microscope image of the sample after resist stripping.
The material outside the MESA is then etched via ion beam etching.
The glass substrate on which the whole stack was deposited and the 20x20 mm^2 silicon sample are loaded in the machine Kenosistec VS80, whose main chamber is provided with a small windows that allows to monitor the process.
A minute after the glass flag has becomes visibly transparent, the process is stopped and the photoresist is stripped off with a 1 min. long ultrasonic bath in acetone.
An optical microscope inspection follows the sample cleaning to ensure the good conditions of the structures. The visual method used to carry out the etching process is not quantitative, therefore AFM inspection is needed to quantify the thickness of material removed.
The profiles taken in different locations of a given device yeld a step height of around 35 nm $\pm$ 3 nm (Figure 4.11), very close to the expected 34.4nm given by the sum of all the layers' thicknesses of the heterostructure.

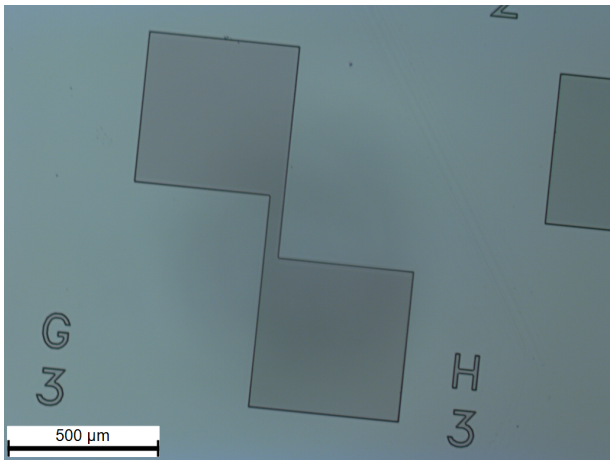

Figure 4.10: Microscope view of the result of the resist development after the MESA exposition.

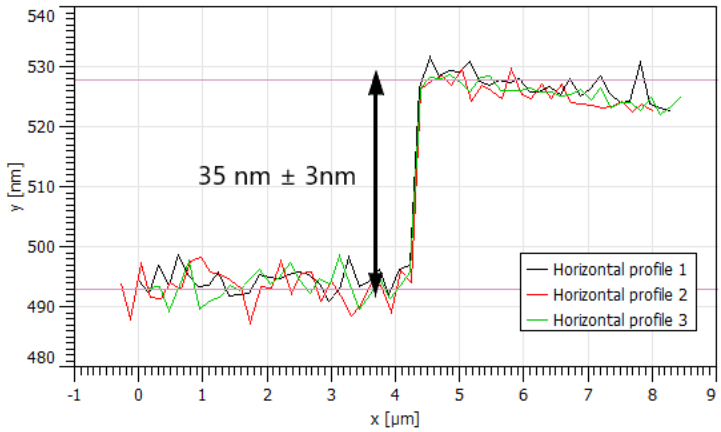

Figure 4.11: AFM profiles of the step between the substrate and the MESA.

Not only this results confirm the successful exit of the process, but it also quantitatively validates the method, which can therefore be used in the successive etching step.
The region of the magnetic pillars is defined in the second lithographic step. The goal here is the removal of the portions of channel between the pillar and the bottom contacts down to the Ta/Ru/Ta buffer layer.
To do this, the substrate is exposed and developed analogously to what was done in the previous step, using the layout reproduced in Figure 4.12.

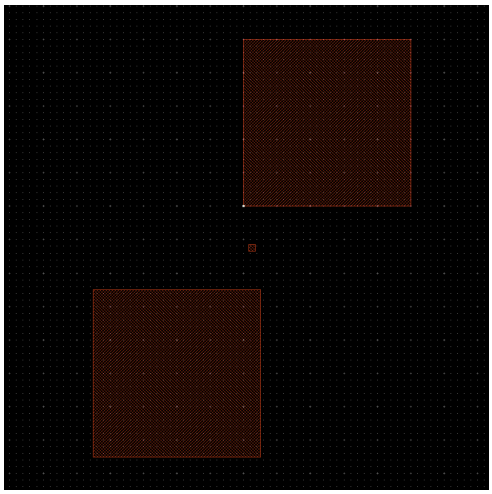

Figure 4.12: Reproduction of the pattern for the definition of magnetic pillar with the software Layout Editor.

With respect to the first step, this time the features are much smaller, making the photoresist development more critical. In fact, a 30s bath in AZ726MIF ends up removing also the non exposed resist from the pillar's region of a large fraction of devices. Reducing the development time to 20s improves the outcome significantly. There are still some missing junctions, but the portion of undamaged ones is high enough to proceed with ion beam etching.
It is important to keep in mind that this time the photoresist cannot be removed after the eching procedure, since it is exploited for the deposition and lift-off of a layer of SiO_2 needed for electrical insulation, as explained later. For this reason also the 10x10mm^2 silicon sample mentioned at the beginning of the discussion undergoes the second steps of lithography and etching. After the latter, in fact, the photoresist can be eliminated from the dummy sample and AFM profiling can be performed.
Figure 4.13a presents the results of such measurement. The sample containing the devices only undergoes microscope inspection to verify the conditions of the pillars (Figure 4.13b).

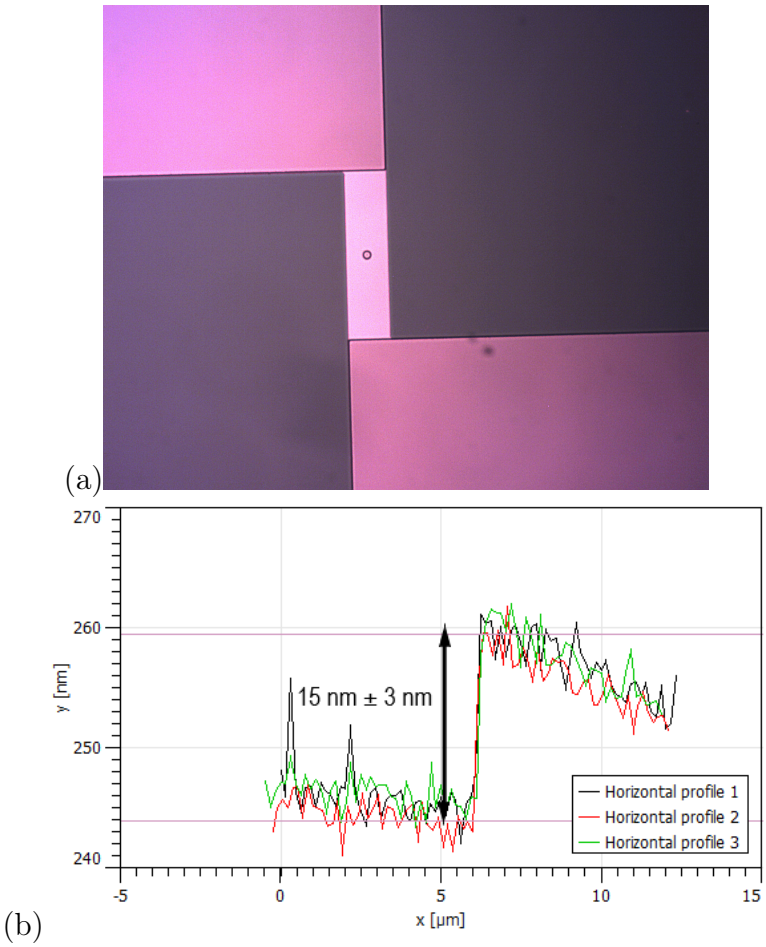

Figure 4.13: (a)Optical microscope image of a pillar after the etching procedure.(b)AFM profile resulting from the second etching step on the edge of a pillar.

The glass flag based method confirms its effectiveness, since here we measure a digged thickness of around 15.5 nm ± 3 nm, very close to the one expected, equal to 14.4 nm.
As already mentioned, a layer of SiO_2 is sputtered on the sample after the second etching phase. The photoresist present from the lithography permits a SiO_2 lift-off that leaves only the bottom contacts and the pillars uncovered, in such a way that the successive deposition of the top contacts does not cause any short circuit between the two. 15nm of SiO_2 are deposited to ensure planarity of the devices. The process is carried out with the Leybold LHZ400 sputtering machine, which provides a deposition rate for SiO_2 of $1.31\frac{nm}{min}$.
The lift-ff of the oxide then consists in a 15 min. bath in photoresist stripper Tecnistrip micro D2 at 70°C. No matter the aggressive procedure, most of the smallest junctions remained covered and therefore non usable.
We believe this is due to the fact that direct lithography is well suited for etching, but

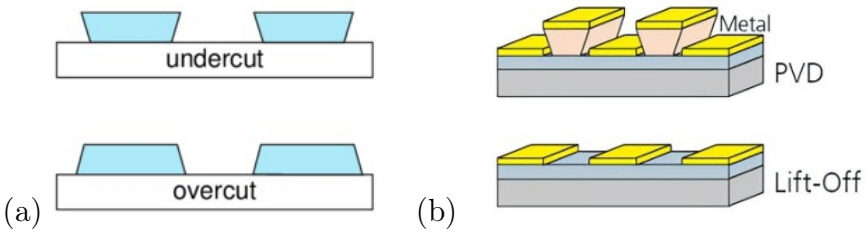

Figure 4.14: (a)Representation of the overcut and undercut profiles. From Ref. [44]. (b)Representation of the lift-off process in presence of undercut profile of the photoresist. From [23].

2.A	A	B	C	D	E	F	2.A	G	H	I	J	K	L
1	40x4	40x8	40x20	20x20	4x4	30x30	1	10x10	40x2	8x2	8x2	2x2	10x10
2	30x4	30x8	30x20	15x2	15x15	8x8	2	40x2	30x2	4x2	4x2	10x10	2x2
3	20x4	20x8	15x2	30x30	2x15	40x40	3	30x2	20x2	2x2	5x5	2x4	2x8
4	15x4	15x8	15x15	2x15	20x30	20x40	4	20x2	15x2	10x10	2x2	2x4	2x8
5	8x4	30x30	8x15	8x20	8x30	8x40	5	15x2	5x5	2x15	2x20	2x30	2x40
6	15x15	4x8	4x15	4x20	4x30	4x40	6	10x10	2x15	2x20	2x30	2x40	10x10
2.B	**A**	**B**	**C**	**D**	**E**	**F**	**2.B**	**G**	**H**	**I**	**J**	**K**	**L**
7	10x10	40x2	8x2	8x2	2x2	10x10	7	40x4	40x8	40x20	20x20	4x4	30x30
8	40x2	30x2	4x2	4x2	10x10	2x2	8	30x4	30x8	30x20	15x2	15x15	8x8
9	30x2	20x2	2x2	5x5	2x4	2x8	9	20x4	20x8	15x2	30x30	2x15	40x40
10	20x2	15x2	10x10	2x2	2x4	2x8	10	15x4	15x8	15x15	2x15	20x30	20x40
11	15x2	5x5	2x15	2x20	2x30	2x40	11	8x4	30x30	8x15	8x20	8x30	8x40
12	10x10	2x15	2x20	2x30	2x40	10x10	12	15x15	4x8	4x15	4x20	4x30	4x40

Figure 4.15: Table displaying the outcome of the SiO_2 lift-off. The red cells correspond to the lost devices.

not well suited for lift-off. In fact, while development after direct lithography induces an overcut profile of the remaining photoresist, development after inverse lithography induces an undercut profile (Figure 4.14a). This negative slope facilitates the subsequent deposition and lift-off since it prevents the material to deposit on sidewalls of the resist, and allows for the solvent to reach the sacrificial layer (Figure 4.14b). Finally, 27 of the 144 devices are lost. From Figure 4.15 we can observe that most of the damaged junctions have the smaller dimension equal to $2\mu m$.

However, due to the large number of preserved structures, the process is brought to completion.
The last lithographic step deals with the top contacts' fabrication. This time inverse lithography is needed to remove the photoresist from the regions covered by the mask. Starting from a positive photoresist, such as AZ5214, this is achieved by means of the process of image reversal described in Section 3.1.3, composed of the following operative steps.

- Exposure with mask alligner to a dose of 40 $\frac{mJ}{cm_2}$;
- Reversal bake of 90 s at 120°C on a hot plate;

- Flood exposure with proper UV lamp to a 8 $\frac{mJ}{cm_2}$ dose.

After this procedure, the resist development procedure is carried out in the same way as the first lithographic step. The optical microscopy inspection confirms successful development for all the structures.
Finally, the stack Cr(10)/Cu(200) is deposited by thermal evaporation using the Moorfield MINILAB-080 machine to obtain the final contacts. Chromium is used as an adhesive layer (10nm are sufficient) while the thick copper is required to guarantee robustness against the invasive measurement tools (tips of a probe station).
The undesired metal is removed by lift-off, consisting this time on a 2 min. ultrasonic bath in acetone followed by a 2 min ultrasonic bath in IPA. Note that ultrasonic bath is usually avoided in lift-off since it risks to strip off material from the regions not covered by resist. In this situation, however, since the litographed features are relatively large, ultrasound bath is chosen in order to speed up the process.
An optical microscopy check confirms the absence of damaged devices. Finally, Figure 4.16 shows a completed devices ready for electrical characterization.

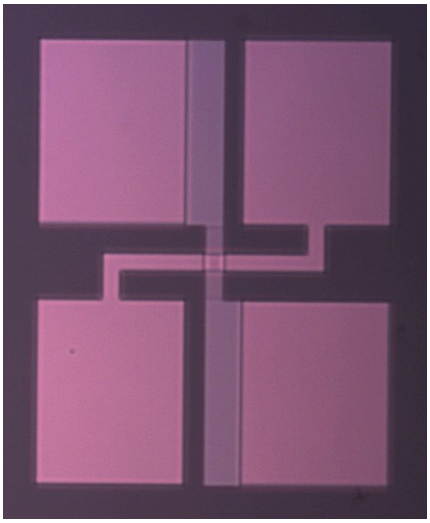

Figure 4.16: Microscope view of the result of the top contacts lift-off.

4.3. Electrical characterization

In this chapter the results of the transport measurements carried out on the fabricated devices will be reported. The first part deals with I-V curves, for the verification of the tunneling nature of conduction, and with the evaluation of the RA product among junctions with different areas. In the second part the dependence on the external magnetic field is explored with the measurements of tunneling magnetoresistance. All the experi-

ments are carried out at room temperature.

Despite being two terminal devices, the junctions under test are provided with four contacts. This configuration is necessary, in the measurement of resistances and in general of I-V curves, to eliminate the contributions of the contacts from the output signal.

Suppose to have a two terminal MTJ. Its electric equivalent in DC is displayed in Figure 4.17, where the central resistance R represents the actual junction while the other two represents the contacts.

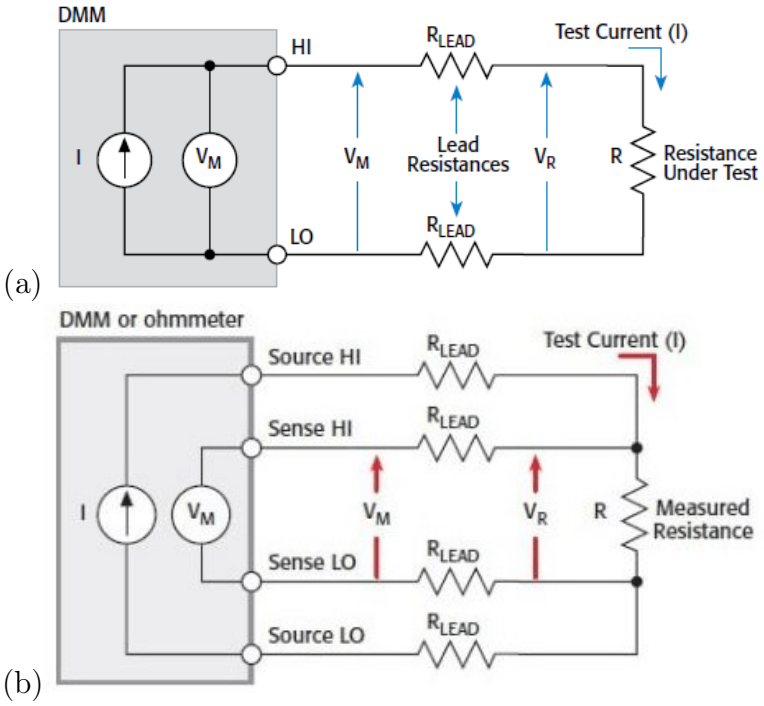

Figure 4.17: Schematic equivalent of the device and of the measurement circuitry in case of a two wires(a) and a four wire(b) measurement. From [54].

Recording the I-V of such a system requires the injection of a current in the two terminals and the subsequent acquisition of the voltage arising between the same two terminals (Figure 4.17a). It is clear that the I-V curve includes the contributions of the contacts (R_{lead}), which is not always exactly controllable and potentially non negligible with respect to the useful signal.

Adding two contacts in correspondence of the junction solves the problem, since two can be used to inject the current while the other two can be used to probe the arising voltage across the junction only (Figure 4.17b). The additional contacts' resistance does not play a role due to the high input impedance of the voltmeter to which they are connected.

For this reason all the measurements are carried out in this manner using the probe station available in our laboratory.

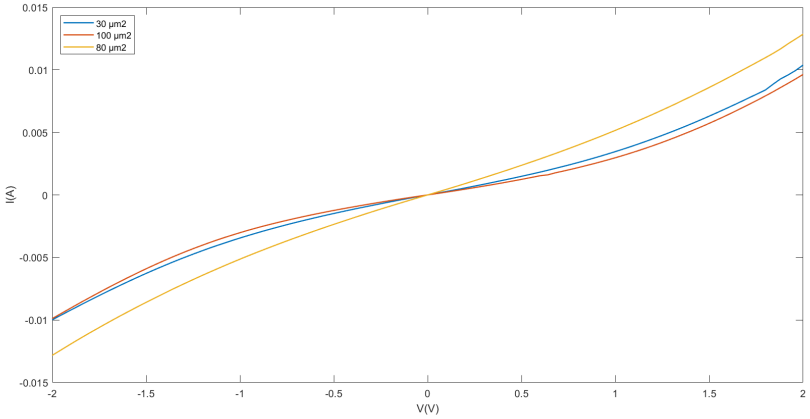

Figure 4.18: I-V curves of the measured devices.

Tunneling transport can be modeled by an exponential I-V relationship, which is approximable to a cubic one for small voltages applied (Equation 4.3).

Figure 4.18 shows the I-V curves recorded on 3 devices with different areas, namely 30 μm^2, 80 μm^2 and 100 μm^2. The cubic dependence is compatible with tunneling. However, since the J-V relationship ideally only depends on the barrier's properties, we expect the I-V curve to be proportional to the area of the junction (A), thus exhibiting a larger slope at the origin as the area increases.

$$J = \frac{I}{A} = \alpha V + \beta V^3 \tag{4.3}$$

$$\frac{\partial I}{\partial V}\Big|_{V=0} = \frac{1}{R} = A\alpha \tag{4.4}$$

Figure 4.18 is a clear indication of the fact that the expected behaviour is not observed, since, for example, the 80 μm^2 device's curve has a larger slope than the 100 μm^2 device's curve. In other words, the RA product is not constant over devices of different areas. Experiments conducted on 20 more devices show in fact a strong oscillation of this parameter. Figure 4.19 plots the values recorded, which have an average value of 10.7 $k\Omega\mu m^2$ and a standard deviation of 7.17 $k\Omega\mu m^2$.

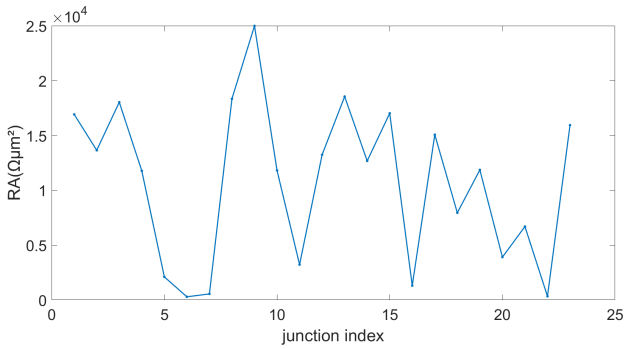

Figure 4.19: RA product of the measured devices.

This discrepancy might be caused either by the MgO barrier not having uniform properties around the sample, making the α and β parameters introduced in Equation 4.3 change among different devices, or defects at the edges of the pillars, either due to the incomplete liftoff of SiO_2 which left residues of photoresist on the edges of the magnetic pillars (as depicted in Figure 4.20) or to the creation of conductive paths at the edges upon ion beam etching.

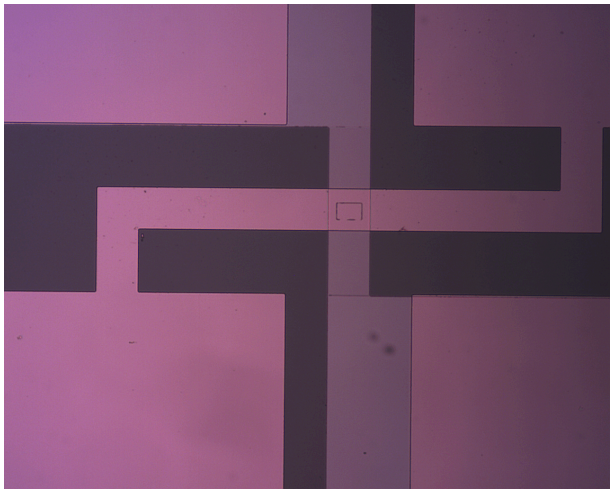

Figure 4.20: Zoom on the pillar region of the optical microscope image of the device. The dark edges of the pillar represent the photoresist leftover.

Despite the sizable device variability of this sample we moved to the investigation of TMR.

The experiments are carried out with a probestation provided with an electromagnet generating an out of plane field up to around 300 Oe powered by a Kepco Bop current generator. The probing current, $100\mu A$, is injected by means of a Keithley current source 6221, while the output voltage is read with a Keithley Voltmeter 2000, using the 4 wire

configuration described earlier.
The instruments are configured to be remotely controlled by a computer via GPIB bus. The measurement process is therefore automatized by means of a matlab script that sends, sequentially, the following commands. The sequence is executed in a loop for every value of the external field.

- Set external field and wait for around 1 s to let the electromagnet's current stabilize;
- Turn on the probing current and for 0.5 s to let the current stabilize;
- Measure the output voltage;
- Compute and store the resistance;
- Turn off the probing current.

A large TMR is successfully observed in several devices over the sample, reaching values of 88.2% and 98.4% in the devices whose R-H cycles are displayed in Figure 4.21a and Figure 4.21b, respectively. TMR is evaluated as $\frac{R_{AP}-R_P}{R_P}$, where R_{AP} is the resistance of the antiparallel state, while R_P is the resistance of the parallel state.

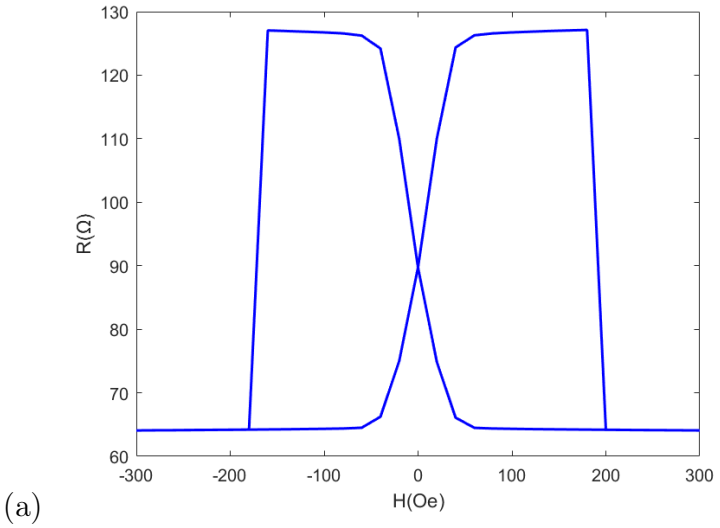

(a)

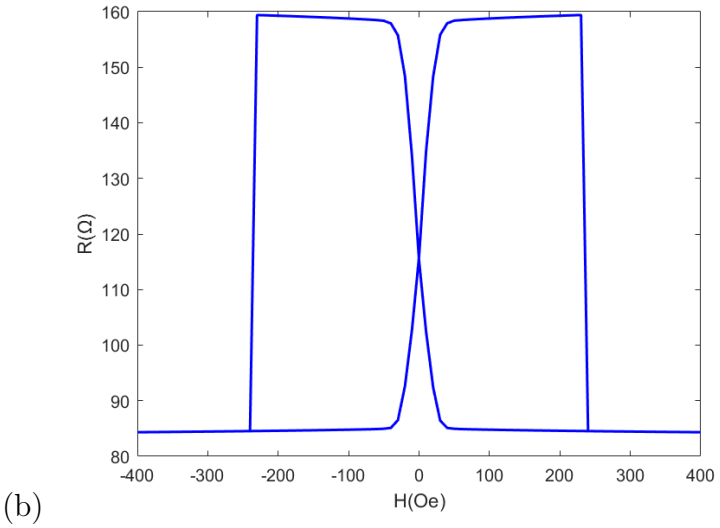

(b)

Figure 4.21: R-H cycles of two of the devices studied.(a) Elliptical junction of 125.6 μm^2 area. (b) Elliptical junction of 94.2 μm^2 area.

We can observe, in both R-H cycles, the sharp contribution given by the reversal of the top layer's magnetization and the smooth transition from parallel to antiparallel configuration given by the bottom layer, which has a weaker perpendicular anisotropy.
The magnetization reversal experienced by the bottom layer manifests itself as a gradual transition from the antiparallel to the parallel resistance owing to the Julliere formula of tunneling resistance for two layers witn non collinear magnetization under the macrospin

approximation (Equation 4.5).

$$R(\theta) = \frac{R_P}{1 + sen(\theta)^2 \frac{R_P - R_{AP}}{R_{AP}}} \simeq \frac{R_P + R_{AP}}{2} + cos(\theta)\frac{R_P - R_{AP}}{2} \tag{4.5}$$

$$for\ |\frac{R_P - R_{AP}}{R_{AP}}| << 1 \tag{4.6}$$

The parameter $\frac{R_P - R_{AP}}{R_{AP}}$ is equal to -0.47 and -0.50 for the cases of Figure 4.21a and Figure 4.21b, respectively, therefore the hypotesis is roughly verified. Since the angle θ is the one between the magnetization of the two layer and since the top one, during the rotation of the bottom one, is magnetized along the out of plane direction, we can conclude that the second term of the tunneling resistance is proportional to the out of plane component of the bottom layer's magnetization.

Another aspect to be noticed is the increase of the coercive field of the top layer, that went from 50 Oe measureed on the unpatterned stack to 180 Oe and 240 Oe for the devices of Figure 4.21a and Figure 4.21b, respectively. It is the effect of patterning, that causes an enhancement of the PMA, as briefly explained in the following lines.

As already pointed out in Section 2.1.2, the geometrical properties of a system influence its magnetic behaviour through the demagnetization energy. In the case of a thin film with PMA, the demagnetization energy pushes the magnetization to lie in the plane of the film, thus contrasting out of plane anisotropy.

The equations reported below point out that the entity of this contrast depends on the size of the thin film.

The anisotropy energy density is given by the sum of the contributions of interfacial out of plane anisotropy(E_{PMA} in Equation 4.7) and shape anisotropy(E_{shape} in Equation 4.7). Here we consider the case of a second order surface so that the demagnetization tensor $\boldsymbol{N}$ can be used to compute the demagnetizing energy. In our reference frame, the z axis points outside of the plane of the thin film.

$$\frac{E_{an}}{V} = \frac{E_{PMA}}{V} + \frac{E_{shape}}{V} = K_{PMA}(1 - m_z^2) + \frac{M_s^2}{2\mu_0}(N_{xx}m_x^2 + N_{yy}m_y^2 + N_{zz}m_z^2) \tag{4.7}$$

Since length and width of the device are comparable and much larger than its thickness, we can assume $N_{xx} = N_{yy} = N_{||}$; $N_{zz} = N_{\perp}$. Neglecting the constant terms, that do not play a role in energy minimization, and considering that $Tr(\boldsymbol{N}) = 1$ we obtain

$$N_{||}(m_x^2 + m_y^2) + N_{\perp}m_z^2 = N_{||}(1 - m_z^2) + (1 - 2N_{||})m_z^2 \tag{4.8}$$

$$\frac{E_{an}}{V} = -m_z^2(K_{PMA} + 3N_{||}\frac{M_s^2}{2\mu_0} - \frac{M_s^2}{2\mu_0}) \tag{4.9}$$

We can notice that the term relative to $N_{||}$ adds up to K_{PMA}, thus enforcing perpendicular anisotropy. Since $N_{||}$ grows as the surface of the magnetic structure shrinks, we can conclude that the effect of patterning is to enhance PMA and therefore increase the coercive field of the devices.
While the coercive field increase is present in the top layer, the bottom layer remains unaltered. This might be related to a non complete etching of the bottom layer or to the fact that, in order for the latter to experience the same effect, a more important surface reduction is needed, but further studies should be carried out in this regard to confirm the hypothesis.
Finally, we consider the possibility of exploiting these MTJs as MRAM elements with SOT induced switching of the free layer. As decscribed in the introduction, in such a device the information is written controlling the magnetization of one the two layers (called the free layer), while keeping the other unchanged (called the reference layer) and it is read exploiting the TMR effect.
As we are not pinning one of the two layer, i.e. by exchange bias, we can just exploit the different coercitivity, working in a range of magnetic fields not affecting the magnetic state of one of the two electrodes. In order to evaluate the signal resulting from the reading operation of one of these storing elements, we measure its R-H cycle with fields in a range that induced the inversion of the bottom layer but does not affect the top one. Finally, the TMR evaluated from the resistance at external field equal to 0 gives the information needed.

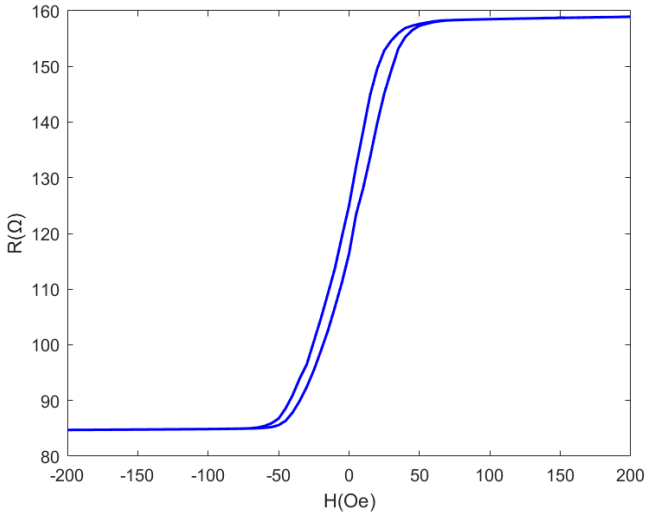

Figure 4.22: R-H cycle of the device of Figure 4.21b in which the bottom layer is the only one to switch.

Figure 4.22 shows the result of such an experiment. For H = 0 the resistance of the parallel state resistance is 116.6 Ω and the one of the antiparallel state is 125.1 Ω, corresponding to a "remanence" TMR equal to 7.3%. Clearly this is much lower than the full TMR, which can be calculated from figure 4.20, in the order of 90 %, but this is due to the fact that upon switching the bottom layer and removing the applied field only a small remanence is observed.

In conclusion, even though the full TMR cannot be exploited, these devices still show two different detectable resistance states upon switching of the bottom layer, thus allowing their operation as storing elements.

Noteworthly, the structure of the stack is suitable for the implementation of the SOT switching of the free layer, as the MTJs is grown on Ta which can act as charge-to-spin conversion material when a current pulse flows in it.

Even though further optimization is needed to achieve full PMA in the bottom layer, these results constitute a solid basis to develop novel MTJs suitable for SOT switching once the conditions for robust SOT induced magnetic switching have been identified. This is the topic of next chapter, focusing on the switching of CoFeB dots induced by current pulses in a Ta underlayer.

5 | Fabrication and characterization of Hall bars for the investigation of Spin Orbit Torque switching

5.1. Layout design

As anticipated in the thesis outlook, the main goal of this chapter is the observation and characterization of SOT induced switching in Ta/CoFeB/MgO trilayers.
Due to the lack of experience in this field, we decided to tackle the problem of SOT induced switching starting from this simple structure instead of the final pMTJ, since in the former we are able to easily obtain good PMA and the literature provides many successful examples [8, 9] that can guide our study.
It has to be pointed out that the non optimal PMA of the bottom layer observed in the analysis of the MTJs of Chapter 4 might not be a detrimental feature for SOT induced switching. As it will be explained later, in fact, an in plane field directed as the injected current is needed to allow SOT induced switching of structures with PMA. A pMTJ in which the bottom layer has partially in plane anisotropy could in principle realize field-free SOT induced switching, given that the in plane component of the free layer's remanent magnetization is aligned with the writing channel. This can be obtained, for example, with elliptical junctions having the long axis parallel to the flow of the writing current, in order to exploit shape anisotropy to obtain the desired initial magnetization's configuration.
These considerations are, however, left to further studies on field-free SOT switching.
The simplest way for reading the magnetic state after switching is using the anomalous Hall effect.
As discussed in Section 2.3.3, when a current $\boldsymbol{j}$ is injected in a ferromagnet with magnetization $\boldsymbol{M}$, the anomalous Hall effect causes a charge accumulation that generates a

voltage drop directed as $\boldsymbol{j} \times \boldsymbol{M}$. The device sketched in Figure 5.1, called Hall bar, can detect such voltage drop, since it allows to inject a current in one arm and to read the AHE voltage related to the z component of the magnetization across the perpendicular one. Following the indication of Ref. [31], the ferromagnetic material is confined in a dot positioned in the region common to the two arms of the cross.

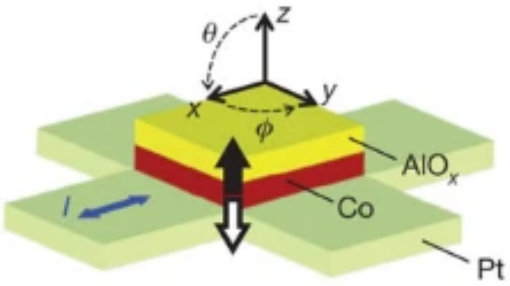

Figure 5.1: Pictorial representation of an Hall bar similar to the one used in our studies, taken from Ref. [31]. The materials indicated on the image refer to the Pt/Co/AlO$_x$ structure used in Ref. [31], while in our case the Hall bar is based on the Ta/CoFeB/MgO structure.

Due to the absence of an optical mask suitable for our purpose, a layout of the devices was designed by means of the software LayoutEditor to be used with the Heidelberg Tabletop Maskless Aligner 100 (MLA) machine.
The geometrical parameters, namely the length, width and thickness of the Hall bar's arms and the ferromagnetic dot's dimensions, have to be selected based on the constraints imposed by the fabrication process, by the measurement tools and by the physics of the phenomenon under study.

- ***Length***
  According to second Ohm's law the longitudinal resistance of the arm is proportional to its length. Since SOT switching imposes a constraint on the minimum amplitude of the current pulses used to induce it, we have to ensure that the longitudinal resistance of the device is low enough to keep the consequent voltage drop below the voltage compliance of the current source, equal to 202V. Regarding the minimum SOT current, the literature reports a required current density in the order of $10^7 \frac{A}{cm^2}$ for micrometric sized devices and current pulse's durations in the μs range [24]. Using the parameters listed in Table 5.1 and approximating all the current to flow

in the tantalum channel we find

$$RI = \rho_{Ta}\frac{l}{A}J_{TH}A < V_{MAX}; \quad l < \frac{V_{MAX}}{\rho_{Ta}J_{TH}} \simeq 1mm \tag{5.1}$$

Parameter	Value
ρ_{Ta}	200 $\mu\Omega cm$
V_{MAX}	202 V
J_{TH}	$10^7 \frac{A}{cm^2}$

Table 5.1: Values of the parameters involved in the choice of the arm's length.

where ρ_{Ta} is the tantalum resistivity, l the arm's length, A the area of the arm's section, J_{TH} the current density required for switching, V_{MAX} the current source's current compliance. The tantalum resistivity taken is the one of β-Ta, on which more details will be provided later.
Considering a safety factor of 5, the length chosen is finally 200 μm.

- ***Thickness***
  The thickness of the tantalum channel is chosen based on two contrasting constraints. The first one is related to the metal's oxidation which clearly compromises conduction reducing the effective thickness available for the current flow. It can occur both from the exposure to the atmosphere and from the proximity to the thermally oxidized silicon on which it is deposited. Moreover, oxidation is enhanced at high temperatures, so that the thermal annealing process also contributes to it. For this reason a too thin tantalum layer could result in devices too fragile to sustain the current densities required from the experiments.
  The second requirement is related to the crystalline properties of tantalum.
  Tantalum exists in two crystalline phases, α and β [27]. They have quite different characteristics, but for our purpose the three following differences have to be kept in mind:
  - β-Ta has a much higher spin hall angle than α-Ta (ranging from -0.0062 to -0.35 [39, 55]);
  - Bulk Ta is almost entirely α phase, while β-Ta is usually obtained in nanometric thin films [27];
  - α-Ta has a resistivity between 15 $\mu\Omega cm$ and 60 $\mu\Omega cm$, while that of β-Ta is

between 170 $\mu\Omega cm$ and 210 $\mu\Omega cm$.

The first highlighted distinction suggests that, in order to obtain successful SOT switching with tantalum, the latter must be in β phase. Only in this case, in fact, the input charge current gets converted into a spin current entering the CoFeB dot high enough to promote its magnetization's reversal.
The second aspect underlines the importance of choosing the correct thickness for the tantalum's layer, which has to be compatible with β phase. Therefore, following the literature [55, 56], we realize Hall bars with different thicknesses, namely 5nm, 10nm and 20nm.
Finally, thanks to the different resistivity, we can have an early indication about the crystalline properties of the deposited film by performing a simple resistance measurement.

- ***Width***
  Also for the width of the cross we have two contrasting limitations. The lower boundary is set by the minimum feature capability of the MLA machine, which can pattern objects down to approximately 2 μm and is able to align successive lithographic steps with a precision of around 1 μm. The upper boundary is imposed by Joule heating, which is proportional to the volume of the channel for a fixed current density.
  $$P_{DISS} = I^2R = \frac{J^2A^2\rho_{Ta}l}{A} = J^2\rho_{Ta}V \tag{5.2}$$
  Where P_{DISS} is the power dissipated responsible for the heating, $V = lA$ is the volume of the tantalum channel.
  To accomodate both restrictions, but also to evaluate the dependence of SOT switching on the dot's area, devices with different width are included in the layout, namely 5 μm, 10 μm, 20 μm and 40 μm.

Figure 5.2a shows the layout used in the lithographic process. It comprises 36 devices, half squared and half circular. For each shape there are four devices for each of the four width listed earlier. In 5.2b the zoom on a single Hall bar is provided. The red, blue and green portions correspond to the first, second and third layers of the layout, respectively.

(a)

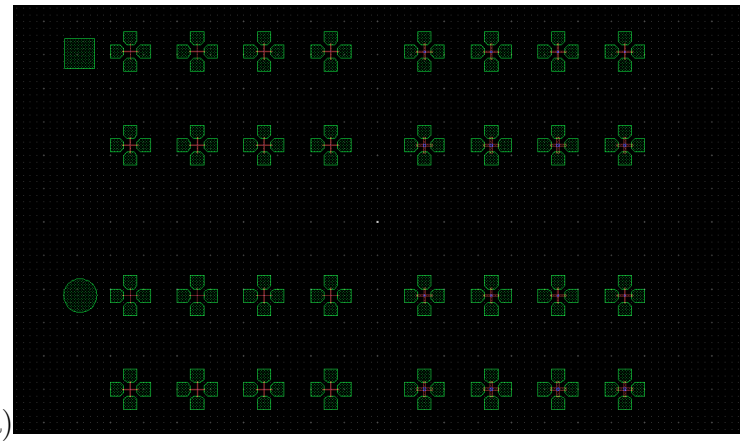

(b)

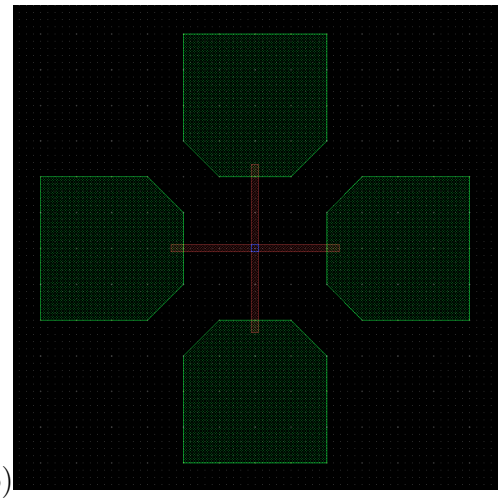

Figure 5.2: (a) Layout used for lithography. (b) View of a single device having a squared dot of 10 μm side.

5.2. Hall bars fabrication process

The devices are fabricated through a three lithographic steps process, similarly to the pMTJs, in which the cross, the central magnetic dot and the contacts are realized in this order.

The fabrication starts with the preparation of a 10x10 μm^2 thermally oxidized silicon substrate, on which the usual AZ5214 photoresist is spin-coated. After the soft bake the exposition of the layout's first layer and third layer (Figure 5.3) is performed using MLA. The latter uses its laser to expose the regions of the layout to a dose of 240 $\frac{mJ}{cm^2}$ for the later lift-off.

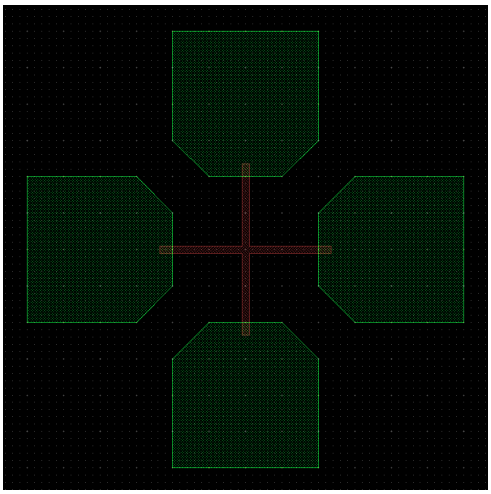

Figure 5.3: First and third layers of the Hall bars' layout.

The development of the photoresist, consisting in a 55 s bath in AZ726MIF developer stopped in water, finally removes the exposed photoresist from the device region.
Note that this first step already contains the third layer, used for the definition of the contacts. They are included to maximize the area of the interface between the bottom tantalum and the contact's metal deposited in the last step.
Successively, the structure Ta(x= 5,10,20)/CoFeB(1)/MgO(2)/Ta(5) is deposited by magnetron sputtering and the sacrificial photoresist is removed by lift-off, involving a low power ultrasound bath in acetone. The bath is first interrupted when no visible residues are present on the sample, which is then analyzed with an optical microscope. If remains are still present, further ultrasound baths of few seconds are carried out until the optical microscope shows a perfect clean surface.
At this point, despite patterning, the magnetic material left is still enough to allow VSM characterization. Thermal annealing is therefore executed and the magnetic hysteresis is recorded. Note that lift-off was chosen instead of etching since it speeds up the process but it still permits to verify the structure's magnetic properties.
The second lithographic step involves the realization of the magnetic dots at the center of the Hall bars. Since now we need to preserve the resist in those regions for the successive etching, inverse lithography is needed.
The substrate is cleaned from the old photoresist and new photoresist is spin-coated and soft baked. Afterwards, the operative steps for inverse lithography are executed as described in Section 4.2. The only difference is that the first step is done with MLA instead of Mask-Alligner, with the parameters listed in Table 5.2

Parameter	Value
Dose	30 $\frac{mJ}{cm^2}$
Defoc	+5

Table 5.2: MLA parameters used for the first step of inverse lithography .

The development consists in a 50 s bath in AZ726MIF developer stopped in water. The bath's duration is larger this time, since 30 s turned out not to be enough to obtain a satisfying result.
The successfulness of the process for all the structures is confirmed by optical microscopy inspection.
Ion beam etching with glass flag method is used to realize the magnetic dots. After the photoresist is removed, an AFM is performed to ensure the correct isolation of the pillar from the rest of the Hall bar.
In the third and last lithographic step the contacts are defined. This is done by transferring the patter of Figure 5.4 on the specimen, corresponding to the third layer of the layout.

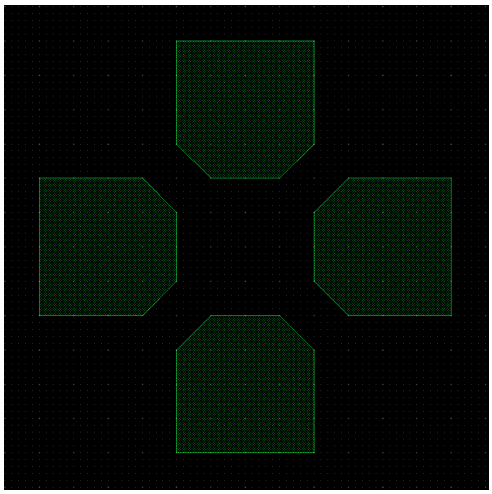

Figure 5.4: Third layers of the Hall bars' layout, used for the contacts' realization.

After the MLA exposure and the resist development, the contact's regions are freed from the latter as the lift-off procedure requires.
Before proceeding with the thermal evaporation of the terminal's metal, one should take into account the fact that tantalum tends to oxidize very easily when exposed to air. Depositing metal directly on the oxidized tantalum results in low quality contacts, having very high and non uniform resistance, making most devices unmeasurable.
The problem can be solved by depositing a 10nm thick film of platinum on tantalum,

after the latter is treated with a 10 min long soft etch, aimed at removing the unwanted oxide.
Since both these steps are performed in the AJA chamber at ultra high vacuum, no contamination of the sample occurs between the two.
Finally, the structure Cr(10)/Cu(150)/Au(25) is deposited by thermal evaporation. Due to the possibly small AHE output signal, the best choice is to minimize the noise introduced by the measurement tools by bonding the devices to a printed circuit board (PCB) holder. Since gold contacts favour the bonding procedure, gold is added on top of copper. Moreover, a gold pad is also preferable due to its stability against oxidation.
The fabrication process ends with the lift-off of the deposited metal, done in the same way as in the first lithographic step.

5.3. Dependence of SOT induced switching on tantalum's thickness

In this section the results of the measurements of SOT induced switching on devices with different tantalum's thicknesses will be shown and discussed.
The experiments performed are based on the one described in Ref. [31].
In orded to perform AHE detection a Keithley Sourcemeter 2611B is connected to one arm of the cross to inject the probing current while a Keithley Nanovoltmeter 2000 is connected to the other arm to read the transverse output voltage.
The current pulse for SOT induction is injected in the same channel as the probing current, therefore for both purposes the Keithley Sourcemeter 2611B is used. It is chosen instead of the Keithley Current Source 6221 since the former is provided with a pulse mode able to generate voltage pulses as short as 50 μs in absence of load, as 500 μs when a load is connected, as it was verified with the oscilloscope. Keeping the pulse duration as short as possible is a crucial aspect, since thermal stress easily deteriorates the devices.
The devices are bonded to a PCB, which is inserted in a holder that provides electrical connection between the PCB's terminals and the measurement tools. This holder is positioned between the poles of an electromagnet powered by a Kepco Bop current source, able to generate fields up to 6000 Oe.

The poles are placed in such a way that the devices experiences, considering the reference frame of Figure 5.5, a magnetic field of the form

$$\boldsymbol{H}_{EXT} = (H_x, 0, H_z) = (H_x, 0, H_x sin(\theta)) \tag{5.3}$$

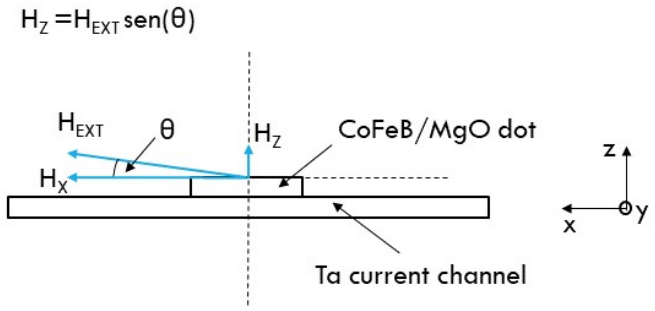

Figure 5.5: Section of the Hall bar taken in the x-z plane in which the external field (H_{EXT}) and its projections along the x axis (H_x) and z-axis (H_z) are displayed. H_{EXT} is tilted of an angle θ with respect to the x axis.

H_z is in order of $\frac{H_x}{10}$ and it is required to maintain the system oriented along z and prevent the formation of domains due to the large component along x [31]. The presence of this out of plane component clearly causes magnetization reversal when the total field reaches the value $H_{c\,EXT} = \frac{H_c}{sin(\theta)}$, where H_c is the coercive field of the dot under study.
In absence of a direct measurement of θ, this relation is used to estimate the tilt of the external field. The coercive field of a certain device in fact is directly found by recording the $R_{AHE} - H_z$ cycle under the action of a pure out of plane using the setup used for the characterization of pMTJs. Once this information is available, for $\theta \leq 10°$ the tilting angle is simply $\theta \simeq sin(\theta) = \frac{H_c}{H_{c\,EXT}}$.
In order to explain the role of H_x, let us recall the LLG equation in presence of SOT induced by a current flowing in the x direction considering the usual reference frame.

$$\frac{\partial \boldsymbol{M}}{\partial t} = -\gamma \boldsymbol{M} \times H_{eff} + \frac{\alpha}{M_s}(\boldsymbol{M} \times \frac{\partial \boldsymbol{M}}{\partial t}) + \tau_{DL}(\boldsymbol{M} \times (\boldsymbol{M} \times \boldsymbol{y})) + \tau_{FL}(\boldsymbol{M} \times \boldsymbol{y}) \quad (5.4)$$

From this equation it can be derived that when the threshold current is overcame the damping like torque $\tau_{DL}(\boldsymbol{M} \times (\boldsymbol{M} \times \boldsymbol{y}))$ makes the magnetization align along the y direction, which is the direction of the SHE induced spin current, instead of the z direction [26]. The situation is exposed in Figure 5.6, in which the image on the left shows the magnetization of the system $\boldsymbol{M}$ before it's destabilized by the input spin current with polarization $\boldsymbol{\sigma}$, while the image on the right shows the magnetization aligned with the -y direction after destabilization. $\boldsymbol{M}$ aligns with the direction opposite to the spin current's polarization since spin and associated magnetic momentum have opposite sign.

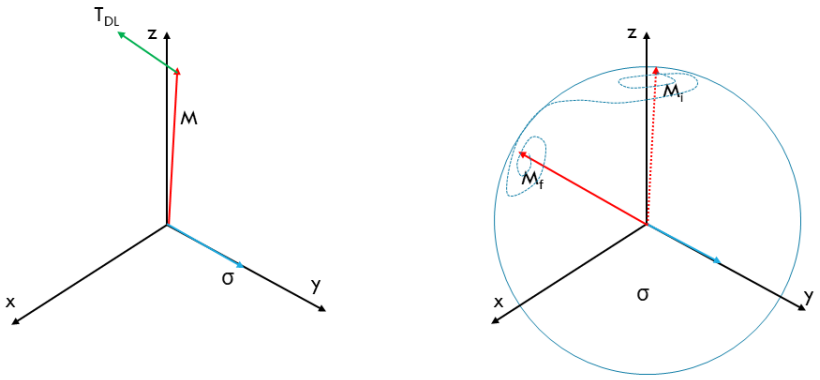

Figure 5.6: Magnetization direction before (left image) and after (right image) SOT has destabilized the z direction. (left image) $\boldsymbol{T}_{DL}$ is the damping-like torque which forces the magnetization $\boldsymbol{M}$ toward the -y direction (for $\tau_{DL} > 0$). (right image) Pictorial illustration of the precessional motion which brings $\boldsymbol{M}$ from the initial position ($\boldsymbol{M}_i$) to the new equilibrium ($\boldsymbol{M}_f$). Precession around -y is caused by the field-like torque, not shown. The precessional motion shown is qualitative and not obtained via simulations.

After the end of the current pulse $\boldsymbol{M}$ lies in a position where the internal effective field given by uniaxial anisotropy $H_{ex} = -\frac{\delta E_{tot}}{\delta M_z}$ is null therefore, in absence of H_x, there is no physical reason for which the magnetization should complete its reversal and deterministic switching is not possible. Adding an external field along the x axis introduces a torque $\boldsymbol{\tau}_z$ along z that pushes $\boldsymbol{M}$ out of the y direction toward one of the two out of plane orientations based on the reciprocal sign between this field and the sign of the current, as expressed by Equation 5.5.

$$\boldsymbol{\tau}_z = \gamma M_S(\frac{\boldsymbol{\sigma}}{|\boldsymbol{\sigma}|} \times \boldsymbol{H_x}) \propto -jH_x(\boldsymbol{y} \times \boldsymbol{x}) = -jH_x\boldsymbol{z} \tag{5.5}$$

Where $\frac{\boldsymbol{\sigma}}{|\boldsymbol{\sigma}|}$ is the versor of the of the spin polarization of SHE induced spin current, j the SOT inducing current density and H_x the external field. The completion of the magnetization reversal process is displayed in 5.7. At this point the anisotropy field arises and takes the magnetization along z.

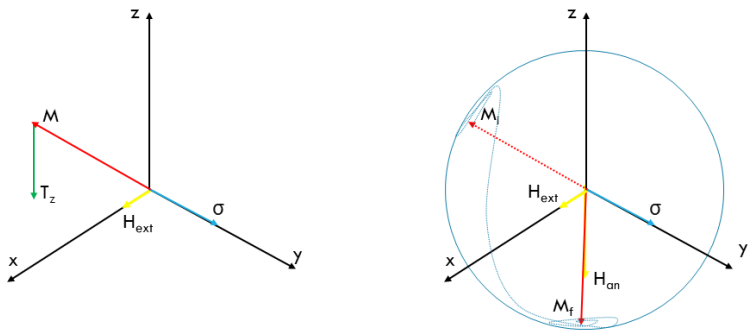

Figure 5.7: Magnetization direction before (left image) and after (right image) the combined action of the torque $\boldsymbol{T}_z$ and of the anisotropy field H_{an} makes the magnetization reach the -z direction. (left image) $\boldsymbol{T}_z$ is the torque induced by the external field H_{ext} directed along x which forces the magnetization $\boldsymbol{M}$ out of the y direction. (right image) Pictorial illustration of the precessional motion which brings $\boldsymbol{M}$ from the initial position ($\boldsymbol{M}_i$) to the final ($\boldsymbol{M}_f$) thus completing the switching event. Precession around y is caused by the field-like torque, not shown. The precessional motion shown is qualitative and not obtained via simulations.

This means that, for example, if the initial state is upwards then the input current and the external field must point in the same direction to allow switching for $\tau_{DL} > 0$.
For a first analysis of SOT switching we follow the methodology of Ref. [31].
The external field described above is swept in a range between -5000 Oe and 5000 Oe and for every intermediate value the transverse resistance is recorded. First, this operation is done in absence of switching current pulses, so that magnetization reversal is induced purely by the z-component of the external field. This evaluation is important because it allows to estimate the tilting angle θ and it shows which are the resistance values corresponding to the two magnetization states.
Finally, the SOT inducing current pulses are introduced as follows:

- A value of the external field is set;
- A 300μs positive current pulse of a given amplitude is injected;
- The transverse resistance is measured;
- A 300μs negative current pulse of the same amplitude is injected;
- The transverse resistance is measured;

All the steps of the experiments are repeated in a loop for every value of the external field and they are automated with a matlab script that controls the instruments. Positive

currents and positive fields point in the same direction.
SOT induced switching is detected when the resistance measured after the positive pulse is different from the one measured after the negative one, since it means that either one of the two pulses was responsible for the reversal of magnetization.

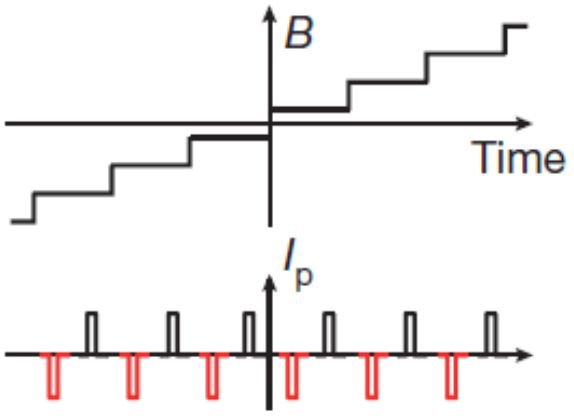

Figure 5.8: Time evolution of the external field and of the current pulses used in the experiments. From [31].

Let us now move to the discussion of the experimental data.
As explained earlier, the first task is to evaluate the coercive field of the magnetic dots of the Hall bars.
Figure 5.9 shows the R_{Hall}-H cycle recorded on a squared device with 5 μm side and Ta thickness of 20 nm.

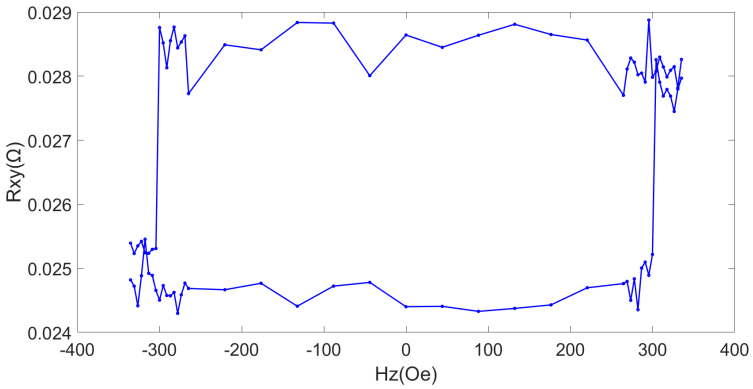

Figure 5.9: R_{xy}-H_z cycle recorded on a squared device of 5 μm side in presence of an out of plane field. The resistive states corresponding to the upwards and downwards magnetization are visible.

Ideally, since AHE induces opposite charge accumulation for opposite magnetization

states, the two resistance values should be equal in magnitude and opposite in sign. An offset is however present, probably due to a slight misalignment of the two halves of the read out arm of the cross or due to non uniform charge flow in the arms.
The loop's amplitude is around 4 $m\Omega$, much smaller than the values reported in literature [9, 31]. This is due to the large mismatch between the tantalum channel's resistance and the CoFeB dot's resistance. The former is, in fact, around 200 Ω for this device,corresponding to a resistivity of around 20 $\mu\Omega cm$, compatible with α-Ta. Negligible current is flowing in CoFeB and small AHE are expected. On the other hand α-Ta means the SOT is not efficient in these devices.
The coercive field is recorded for a device of every dimension, for both shapes. The results are listed in Table 5.3.

Circular		Squared	
Diameter(μm)	Coercive field($\frac{A}{m^2}$)	Side(μm)	Coercive field($\frac{A}{m^2}$)
5	245	5	295
10	195	10	275
20	195	20	245
40	145	40	220

Table 5.3: Coercive fields of the squared and circular magnetic dots as a function of their dimensions for a Ta thickness of 20 nm.

In the second part of the experiment current pulses and almost in plane field (H_p) parallel to the current pulses (i.e. along x) are introduced. The first analyzed sample is the one with tantalum's thickness of 20nm.
Figure 5.10a shows the hysteresis of the device of Figure 5.9, again in absence of current pulses. From its switching field we can conclude that the external field H_p is almost in plane, tilted of around 6°, which belongs to the range tested in Ref. [31]].

As expected, the injection of current pulses does not determine the arising of SOT induced switching. The only effect produced by the current on the system is a strong reduction of the coercive field due to thermal activation by Joule heating. Figure 5.10b displays the R_{xy}-H_p cycles recorded with the protocol of Figure 5.8 and bipolar current pulses of $1.5 \times 10^7 \frac{A}{cm^2}$. The almost in plane field at which magnetic switching is observed (due to the z component of H_p) is reduced from around 3300 Oe to around 2000 Oe but no switching induced by current pulses is observed.

By further increasing the current density up to $2.5 \times 10^7 \frac{A}{cm^2}$ (see panel c of Figure 5.10) we still do not observe any current induced switching but only a further reduction of the H_p determining the magnetization switching.

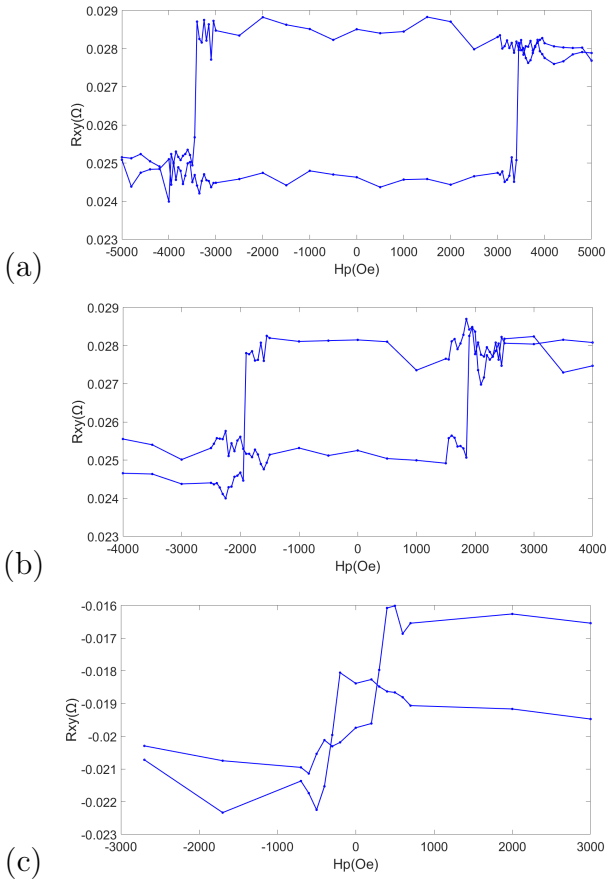

Figure 5.10: (a) R_{xy}-H_p cycle recorded on a squared device of 5 μm side in presence of the slightly tilted from the plane field. The magnetization switches at 3450 Oe, yelding a tilting angle of around 6° (b) R_{xy}-H_p cycle recorded as in (a) with current pulses of $1.65 \times 10^7 \frac{A}{cm^2}$. The magnetization switches at around 1800 Oe. (c) R_{xy}-H_p cycle recorded with $2.5 \times 10^7 \frac{A}{cm^2}$ current density pulses. The cycle is nearly absent and the resistive states corresponding to upwards and downwards magnetization are lost.

We don't believe the absence of switching is due to a non sufficient current density, since the highest one tested, equal to $2.5 \times 10^7 \frac{A}{cm^2}$, in enough to provoke an anomalous deterioration of the AHE loops (Figure 5.10c).
The lack of current induced switching must be instead ascribed to the large thickness of the Ta layer, favouring the α phase with low spin Hall angle.

The second specimen studied is the one with tantalum's thickness of 10 nm. The results

refer to a device with a circular dot of 10 μm diameter.
The hysteresis loop taken in absence of current pulses, displayed in Figure 5.11a, shows a more significant difference between the two resistance states, equal to 0.46Ω, with respect to the previous case. This is a symptom of the much larger resistance of the tantalum's channel, corresponding to a resistivity of around $200\mu\Omega cm$. The value is coherent with β phase of tantalum and therefore successful SOT switching can be expected.
For small current densities here as well the only observed effect is the shrinking of the hysteresis cycle (Figure 5.11).

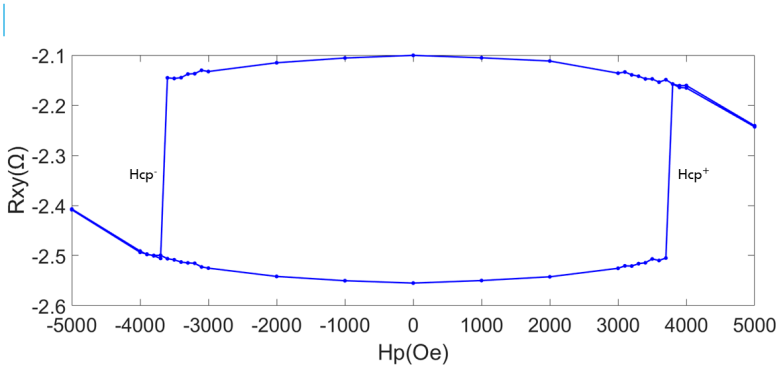

(a)

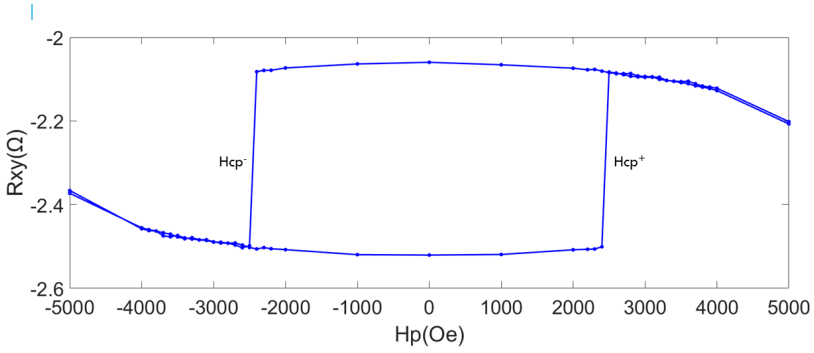

(b)

Figure 5.11: (a) R_{xy}-H_p cycle recorded on a circular device of 10 μm diameter in absence of current pulses. The two resistance states are visible. (b) R_{xy}-H_p cycle recorded on the same device with $0.8 \times 10^7 \frac{A}{cm^2}$ current density pulses. The magnitude of the coercive field ($|H_{cp}^{\pm}|$) goes from 3750 Oe to 2450 Oe.

Reaching the value of $1 \times 10^7 \frac{A}{cm^2}$ SOT induced switching starts to take place in addition to the magnetic switching at $H_{cp} \simeq \pm$ 1600 Oe induced by the z component of H_p . As it

can be seen in figure 5.12, two regions of fields between 2240 Oe and 2500 Oe and between -2280 Oe and -2400 Oe, (greys areas in Figure 5.12) appear where SOT effect is strong enough to overcame H_z which tends to keep the state unchanged. However, since we are still too close to the threshold currend density, the switching fails to be deterministic. The blue curve of Figure 5.12 plots the values of transverse resistance R_{xy} recorded after the injection of positive pulses, while the red one plots the transverse resistance measured after the injection of negative pulses (see Figure 5.8).
The two ranges of field are not symmetric, but this issue will be discussed later.

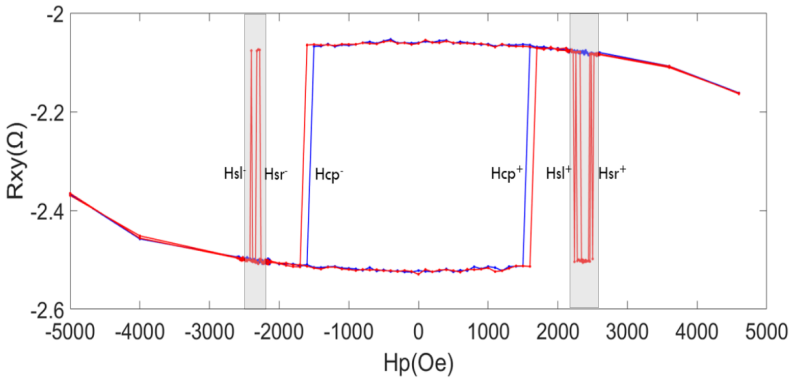

Figure 5.12: R_{xy}-H_p loops recorded with the application of positive pulses (blue curve) and negative pulses (red curve). Shaded areas indicate the current induced switching.

Further increasing the current density makes the SOT induced switching entirely deterministic for increasingly wider ranges of the applied field. This is due to the fact that the minimum in plane field required to enable it gradually decreases.
Figure 5.13 shows the results obtained for current densities equal to $1.4 \times 10^7 \frac{A}{cm^2}$ (Figure 5.13a) and $1.6 \times 10^7 \frac{A}{cm^2}$ (Figure 5.13b).

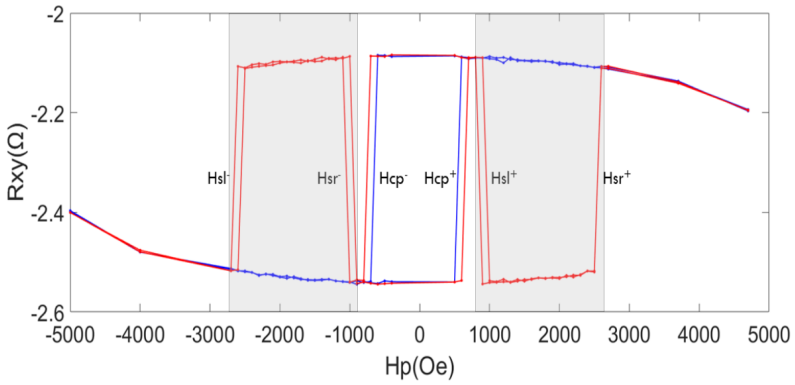

(a)

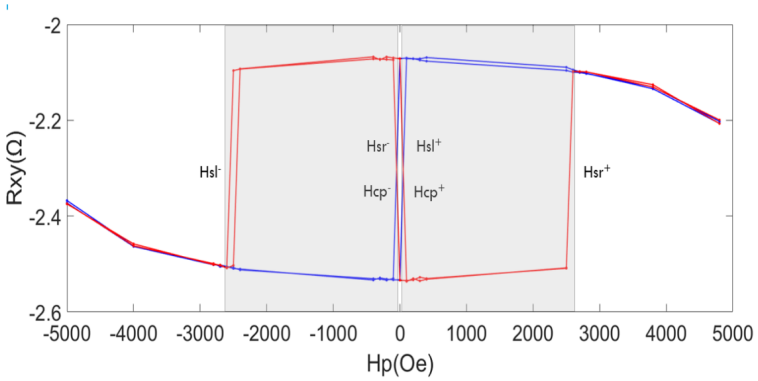

(b)

Figure 5.13: (a) R_{xy}-H_p cycles with positive (blue curve) and negative (red curve) $1.4 \times 10^7 \frac{A}{cm^2}$ current density pulses. (b) R_{xy}-H_p cycles with positive (blue curve) and negative (red curve) $1.6 \times 10^7 \frac{A}{cm^2}$ current density pulses. From (a) to (b) we observe a decrease of the effective coercive fields $H_{cp}^{\pm}$ at which the transition induced by the z component of H_p happens and a widening of the windows where the current induced switching is observed.

The same experiment is performed for current densities in the range between $0 \times 10^7 \frac{A}{cm^2}$ and $1.8 \times 10^7 \frac{A}{cm^2}$, with a step of $0.2 \times 10^7 \frac{A}{cm^2}$. Finally, the results are summarized in the phase diagram of Figure 5.14, in which the critical fields characterizing each R-H cycle are associated to the value of current density at which they are recorded [31]. The critical fields considered are (see Figure 5.14):

- positive and negative coercive fields $H_{cp}^{\pm}$ (blue curves in Figure 5.14)
- extremes of the positive switching window H_{sl}^{+}, H_{sr}^{+} if present (lower red and green curves in Figure 5.14)

- extremes of the negative switching window H_{sl}^{-}, H_{sr}^{-}, if present (lower red and green curves in Figure 5.14)

The switching regions extend toward $H_p = 0$ as the current density increases until it seems to saturate after $1.6{\times}10^7 \frac{A}{cm^2}$. In reality the window's lower end keeps decreasing but it becomes smaller than the field step, chosen equal to 100 Oe. Since two current pulses are sent for every field's value, we decided not to further decrease the field step to minimize the stress caused by Joule heating.

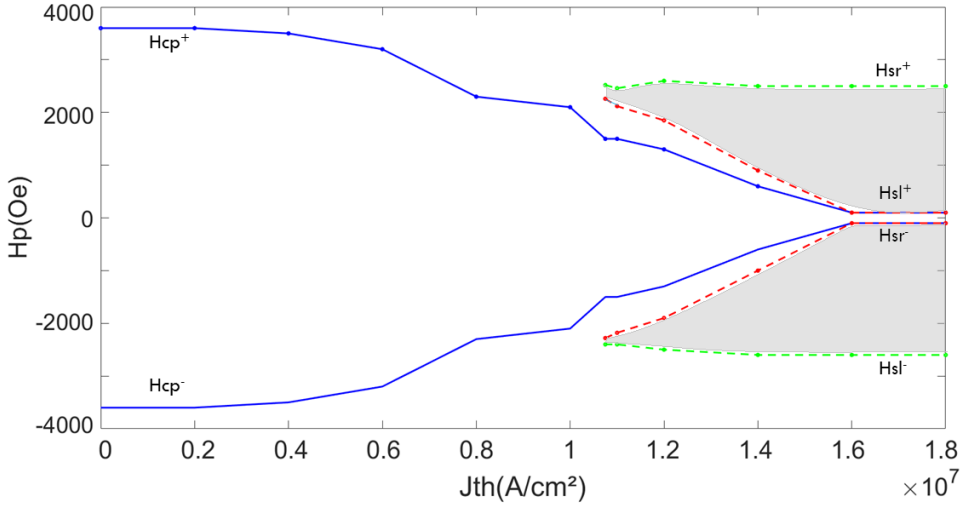

Figure 5.14: Phase diagram summarizing the dependence of SOT induced switching on the input current density and on the applied field. The shaded regions between the red and green curves represent the switching windows.

Finally, the 5 nm sample is addressed. Once again, the channel's resistance suggests that tantalum is in β phase.
However, we could not record reliable data regarding the SOT induced switching behaviour, since the device are not able to sustain the current pulses. Current densities in the range of $0.1 \times 10^7 \frac{A}{cm^2}$ are in fact enough to break down the device, probably due to the oxidation which makes the portion of channel actually available for conduction too small. The device's breakdown is detected when the transverse resistance starts assuming high random values in a irreversible way.
To summarize with 10 nm thick Ta layers in the Ta/CoFeB/MgO structure we have obtained devices displaying reliable and deterministic SOT switching in agreement with literature and the experimental methodology of the seminal paper by Miron *et al.* [31].

5.4. Investigation of SOT induced switching asymmetry

The results presented in the previous section refer to a device with circular dot of 10 μm diameter and 10 nm thick Ta layer. Smaller devices with different geometries in the same sample (t_{Ta} = 10 nm) are later tested, showing an intriguing asymmetric switching behaviour. This section presents the results of the SOT switching experiments collected from two devices having different types of dots, namely squared of 5 μm side and circular of 5 μm diameter, with particular attention given to the differences arising between the characteristics of SOT induced switching for positive and negative values of the external field. Regarding the device treated in the previous section (10 μm diameter, circular dot), the phase diagram of Figure 5.14 does not displays a significant asymmetry between the switching field windows for positive and negative fields. The only indication of such a difference is encountered in Figure 5.12, which shows a slightly larger switching window for positive fields than for negative ones.
In figure 5.15 the results of the experiments conducted on the circular device are reported (5 μm diameter, circular dot).

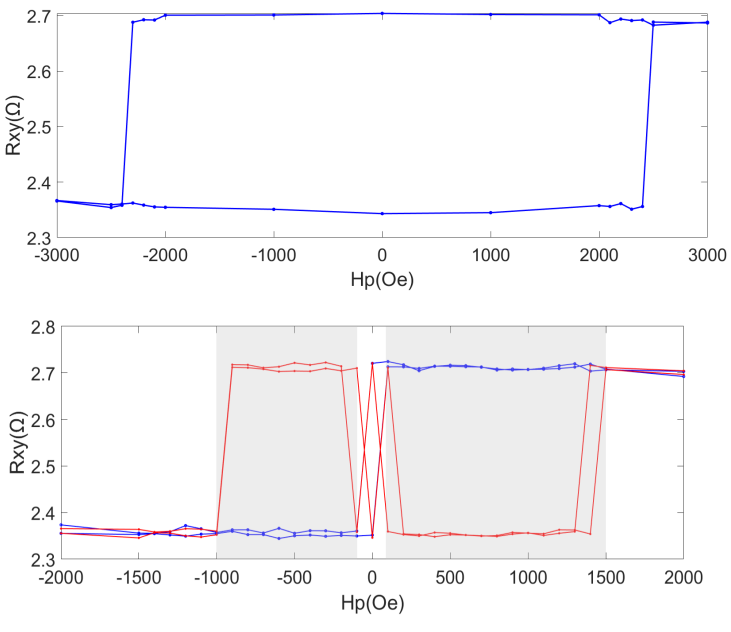

Figure 5.15: (a) R_{xy}-H_p cycle recorded on a circular device of 5 μm diameter in absence of current pulses. The magnetization switches at 2350 Oe, yelding a tilting angle of around 7° (b) R_{xy}-H_p cycle recorded on a squared device of 5 μm side in presence of current pulses of $1.8 \times 10^7 \frac{A}{cm^2}$. The positive field window is visibly larger than the negative one.

First, the cycle measured without current according to the protocol of Figure 5.8 (Figure 5.15a) allows to estimate the field angle, which is around 7°. Then, by activating the switching current the usual broadening of the switching windows is observed but, in contrast with Ref. [31], these windows have different width for positive and negative fields. In the case of Figure 5.15c, for example, the negative window goes from -500 Oe to -100 Oe while the positive one goes from 100 Oe to 1400 Oe. This means that SOT switching is more favoured for positive fields than for negative ones, since for the same current density the former allows a larger working window. The usual H-J phase diagram (like that in Figure 5.14), composed after the collection of data from experiments at different current densities, confirms this tendency and it is displayed in Figure 5.16. Again,for this phase diagram the field step is 100 Oe.

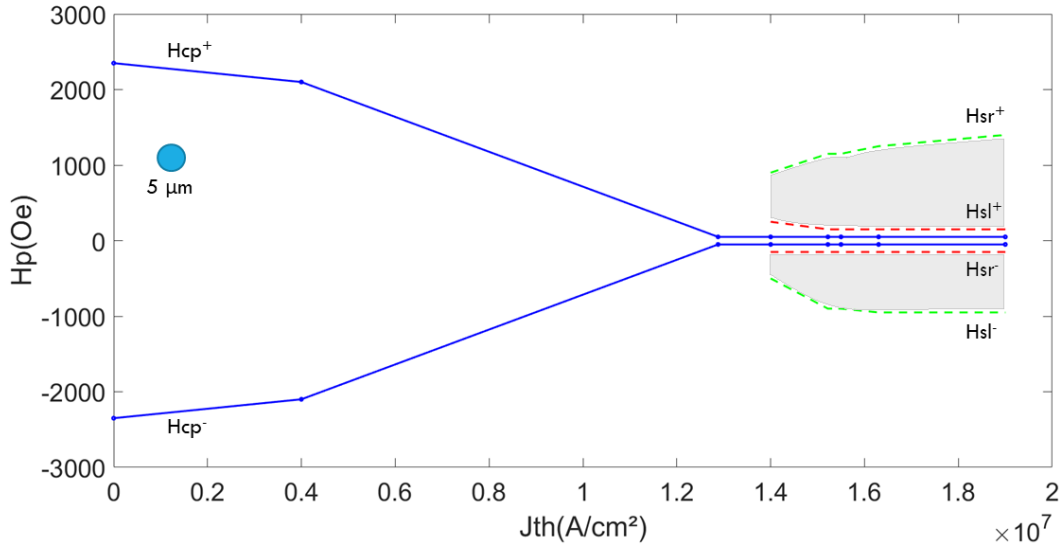

Figure 5.16: Phase diagram summarizing the dependence of SOT induced switching on the input current density and on the applied field for the circular device of 5 μm diameter. The regions between the red and green curves represent the switching windows. The asymmetry is clearly visible as the two switching regions (grey areas) have different width.

Noteworthy, the shape of the dot is the same as the one of the device analyzed in the previous section (circular dot), which only showed a small asymmetry in the case of current density close to threshold. The asymmetry therefore seems to be enhanced by the reduction of the dot's dimensions. The non optimal controllability of the z component of the field (due to sample mounting) should not play any role, since it is supposed to

influence in the same way the switching behaviour for positive and negative fields. In order to corroborate the hypothesis, experiments are also conducted on a device with squared dot of 5 μm side. In this way we can both confirm the dependence of asymmetry on the dot's size and evaluate an eventual influence of the dot's shape on the switching behaviour.

The current-free hysteresis cycle (not shown) presents a coercive field of around 3650 Oe, compatible with a tilting angle of around 5.5°. The injection of current pulses having density of $1.2 \times 10^7 \frac{A}{cm^2}$ determines the appearance of the expected asymmetric switching regions, as it can be see in Figure 5.17. The effect here seems even more pronounced, as for this current amplitude the negative switching window is not present.

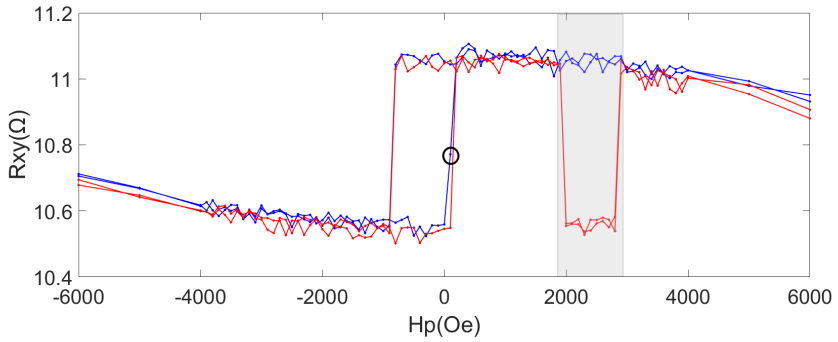

Figure 5.17: R_{xy}-H_p cycle recorded on a squared device of 5 μm side in presence of current pulses of $1.2 \times 10^7 \frac{A}{cm^2}$. The black circle indicates the intermediate state.

Another important aspect not observed in the previous experiments can be noted. The fields at which switching is caused by the z-component of H_p, i.e. $H_{cp}^{\pm}$ are not symmetric and this characteristic is present for values of the input current higher than $1.2 \times 10^7 \frac{A}{cm^2}$, as it can be visualized in the J-H phase diagram of Figure 5.19. We believe this is caused by the complex interplay of SOT switching and H_z, that favours one of the two states.

With reference to Figure 5.17, when H = 100 Oe, the positive pulse make the system reach an intermediate state and the negative pulse brings it back to the lower one. When H = 200 Oe the positive pulse promotes switching toward the up state via thermal activation, but H_z is too strong and H_x is too weak to allow the negative pulse in turn to switch. This remains true up to 2000 Oe, where the negative pulse begins being effective. Measurements carried out at a slightly higher current, $1.26 \times 10^7 \frac{A}{cm^2}$, show the emerging of an anomalous switching window for low fields which suggest that SOT switching is responsible for the asymmetry of the hysteresis (Figure 5.18).

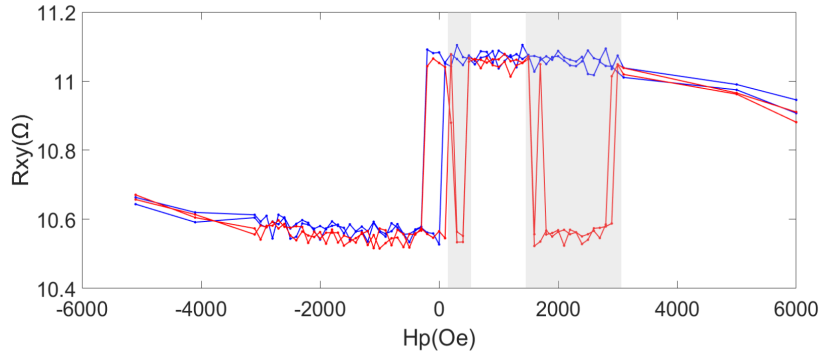

Figure 5.18: R-H cycle recorded on a squared device of 5 μm side in presence of current pulses of $1.26 \times 10^7 \frac{A}{cm^2}$. The additional switching window occurs between 200 Oe and 400 Oe.

Further increasing the input current make the negative switching region appear and the two positive windows to merge into a single one, as it can be noted in the J-H phase margin of Figure 5.19.

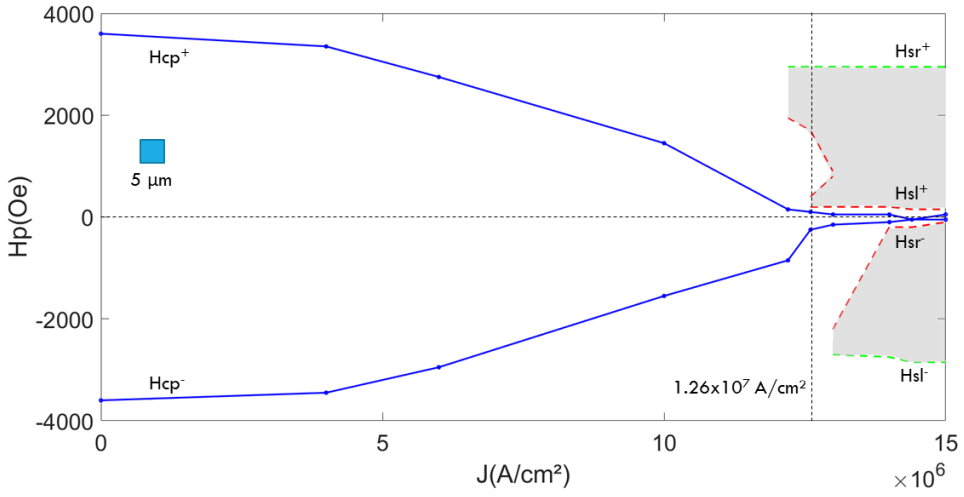

Figure 5.19: Phase diagram summarizing the dependence of SOT induced switching on the input current density and on the applied field for the squared device of 5 μm side. The regions between the red and green curves represent the switching windows. The asymmetric blue curves represent the asymmetric hysteresis caused by SOT.

A different type of experiment is then performed to evaluate the same phenomenon from a different point of view.

A larger positive than negative switching window for a given current density in Figure 5.19 should correspond to the minimum density current required for reversal being lower if a positive field, rather than a negative one, is applied. In order to verify this statement, the transverse resistance of the device with squared dot of 5μm side is recorded after the injection of 300 μs long current pulses with progressively larger current density in presence of an external in plane field pointing in the positive x direction. This time, however, the out of plane component of the field has to be minimized in order for it not to influence the outcome of the measurements.

For this purpose, the structure sustaining the PCB holder is modified in order to allow the rotation of the latter around the y axis. The angle of the sample with respect to the y axis is therefore adjusted in order to minimize the difference between the transverse resistance acquired for +6000 Oe and -6000 Oe. As the out of plane component of the field tends to zero for such a large field, in fact, the magnetization direction tends to reach the in plane direction and no detectable AHE signal should be seen. Manually adjusting the sample's angle while monitoring the variation of the difference between the transverse resistance at +6000 Oe and -6000 Oe allows to reach a minimum value of that variation smaller or equal to 0.05 Ω, which corresponds to the R_{xy}-H_p loop of Figure 5.20, displaying a sizable AHE only at low in plane fields where PMA gives rise to OOP remanent magnetization with some hysteresis.

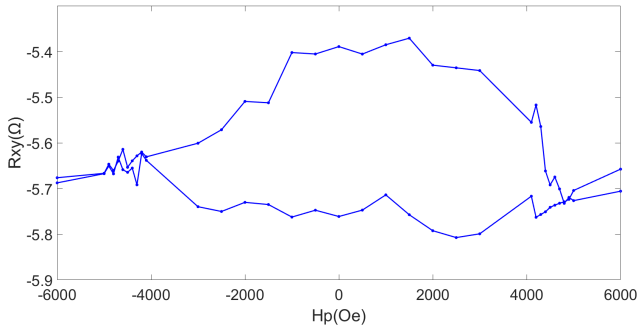

Figure 5.20: R_{xy}-H_p cycle recorded on the squared device of 5 μm side after the minimization of Hz. The steep transitions given by H_z are no longer present.

R_{xy}-J hysteresis loops are then recorded for different values of the external in plane field, from -2500 Oe to +2500 Oe. The loop obtained for $H_x = 500$ Oe is reported in Figure 5.21.

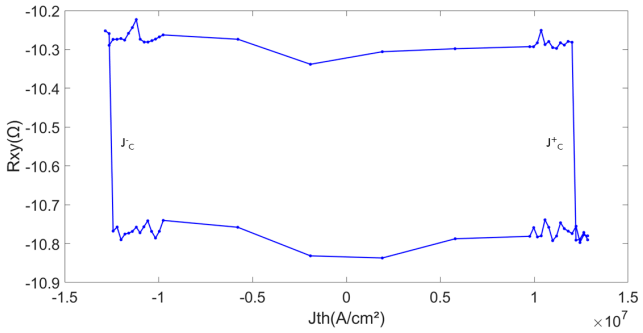

Figure 5.21: R_{xy}-J hysteresis recorded with applied in plane field equal to 500 Oe on a 5 μm square dot.

As expected, the threshold current density decreases as the field increases in absolute value.
In conditions of perfect symmetry one expects the width of the cycles, evaluated as the difference between the positive and the negative switching thresholds $\Delta J_c = J_c^+ - J_c^-$, to be equal for negative and positive fields. However, this does not occur in the case under analysis, as displayed in 5.22, in which the width of the hysteresis are plotted as a function of the in plane field.

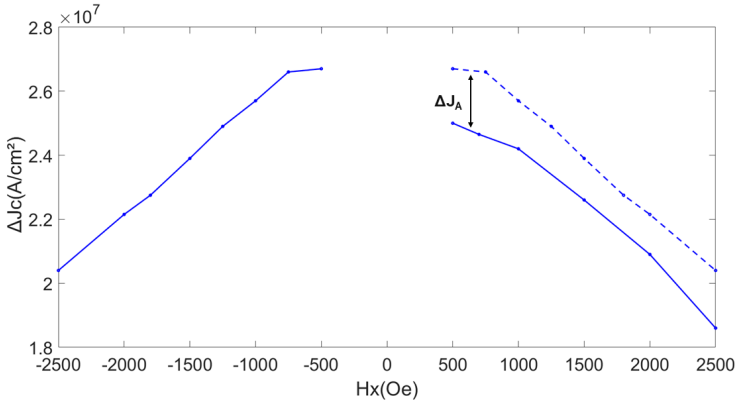

Figure 5.22: Width of the R_{xy}-J loops as a function of the in plane field under which they are recorded. The results reported refer to fields larger than 500 Oe in absolute value. The dashed curve represents the expected dependence of the loops' width on H_x in a symmetric situation. The magnitude of the asymmetry is indicated by the quantity ΔJ_A shown in figure.

We plot the width of the hysteresis loops in order to avoid to include in the graph the effect of a non controlled out of plane component of the field H_z. Since H_z stabilizes on of the two OOP magnetic states, its effect on the current thresholds is to enlarge the one linked to the transition to the unfavoured state and to decrease the one related to the transition to the favoured state, thus leaving the loop's width unchanged.
For this reason the influence of the spurious H_z should be appreciable in the dependence of the sum between positive and negative thresholds on H_x, showed in Figure 5.23. The average of the slopes taken for positive and negative H_x is around $8.8{\times}10^3 \frac{A}{mTcm^2}$.

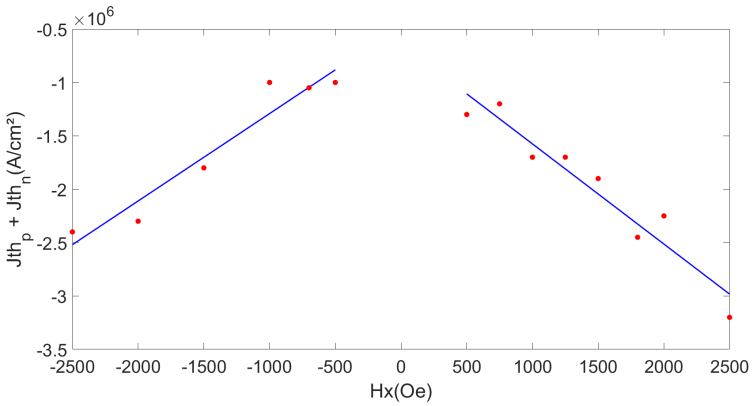

Figure 5.23: sum of the positive and negatives thresholds of the R_{xy}-J loops as a function of the in plane field under which they are recorded. The results reported refer to fields larger than 500 Oe in absolute value.

Different signs of H_z favour different magnetization states, but since changing sign of H_x inverts the current polarity responsible for the up-down and down-up transition, the spurious H_z results in a shift of the hysteresis loop in the same direction for positive and negative in plane fields.
We can finally confirm the tendency of SOT induced switching to be favoured when positive in plane fields are used to promote it. This is compatible with the presence of an internal bias field pointing along the direction of the injected current, which might be caused by the interacial DMI interaction between Ta and CoFeB. Morover, the comparison between the results collected from devices with different shapes and dimensions suggest that the asymmetric switching behaviour gets more pronounces as the size of the magnetic dots is reduced and that, for the same size, the squared geometry developes a larger asymmetry than the circular one. In order to understand the physical mechanisms involved, micromagnetic simulations should be performed. They are however left for further studies.

5.5. Dependence of SOT induced switching on the transverse applied field

The next aspect addressed in the study of SOT induced switching is its dependence on the application of a magnetic field along the y direction. As pointed out in Chapter 2, the field-like and damping-like torques can be associated to two effective fields that act on the magnetization generating them. In particular, in this configuration in which the spin Hall effect generates a spin current polarized in the y direction, the field-like effective field is directed in the same way.

$$T_{FL} \propto \boldsymbol{M} \times \boldsymbol{y}; \quad H_{FL} \propto \boldsymbol{y} \tag{5.6}$$

The application of an external field H_y is therefore expected to influence the spin orbit torques by adding up to the field-like effective field.
The influence of the field-like torque and in general of the application of a transverse field on the switching behaviour is not treated often in literature. In Ref. [14, 25] is reported a shift of the R_{xy}-J hysteresis loops increasing as the magnitude of H_y increases, justified by the formula for the switching current density $j_c^{\perp}$ of a macrospin in presence of H_y and taking the field-like torque into account [25].

$$j_c^{\perp} = \frac{2eM_s t}{\hbar \xi_{DL} \beta (2+\alpha\beta)} [(1+\alpha\beta)B_y \pm \sqrt{2\alpha\beta(2+\alpha\beta)B_k^2 + B_y^2}] \tag{5.7}$$

where $M_s t$ is the unit surface magnetization of the ferromagnetic layer, α is the damping constant, and B_k is the effective anisotropy field, ξ_{DL} is the damping-like torque efficiency, β is the FL-to-DL torque ratio.
The $\pm$ sign has to be replaced with $+$ for the evaluation of the positive threshold and with - for the evaluation of the negative one. Summing the two, the term under the square root cancels out and a linear dependence between the sum of the thresholds and B_y arises. Since $\alpha\beta << 1$ [48] we have:

$$j_c^{+} + j_c^{-} \simeq \frac{eM_s t}{\hbar \xi_{DL} \beta} B_y \tag{5.8}$$

In order to evaluate the presence of the described behaviour, R_{xy}-J hysteresis cycles are recorded for different values of the ratio $\frac{H_y}{H_x}$ with a fixed H_x.
H_y is changed by rotating the sample around the z axis using a stepper motor controlled by an Arduino Uno controller. Arduino Uno receives the commands of the matlab script via USB and sends them to the stepper controller that enables rotation.

After a given working angle ϕ is set (see Figure 5.24), the following operations have to be performed before starting the measurement:

- The external field has to be adjusted to $H_{ext} = \frac{H_x}{cos(\phi)}$ to keep the H_x constant;
- H_z have to be minimized since the rotation usually makes a spurious out of plane component of the field appear. The optimization is done here as well by minimizing the difference between the transverse resistance recorded at +6000 Oe and -6000 Oe.

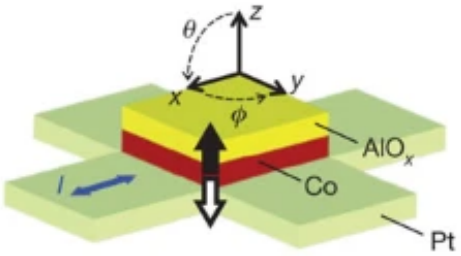

Figure 5.24: Image 5.1 is reproposed here to highlight the angle ϕ scanned in the experiments presented in this section.

Following [25], the range of values for $\frac{H_y}{H_x}$ is chosen between -1 and +1. The experiment is repeated for the same values of $\frac{H_y}{H_x}$ with different H_x, namely 1500 Oe, 2000 Oe, 2500 Oe to also evaluate the dependence on this parameter.
Equation 5.7 is used to fit the data. Fitting parameters for the positive and the negative threshold should be the same, since the two only differ for the sign discussed earlier. However, here we find the fitting parameters separately for the two to evaluate the presence of discrepancies. The positive and negative threshold current densities as a function of the H_y for H_x = 1500 Oe, 2000 Oe, 2500 Oe are plotted respectively in Figure 5.25a, 5.25b, 5.25c.

$H_x(Oe)$	a ($\frac{A}{mTcm^2}$)		b (mT^2)	
	j_c^+	j_c^-	j_c^+	j_c^-
1500	1×10^4	1.83×10^4	1.58×10^6	3.94×10^5
2000	1.41×10^4	1.97×10^4	4.77×10^5	3.96×10^5
2500	1.46×10^4	1.59×10^4	4.92×10^5	3.16×10^5

Table 5.4: Fitting parameters of the positive and negative threshold current density vs. H_y curves for all the studied H_x.

In all three cases the experimental data relative to the positive and negative thresholds starts deviating from the fitting curve for certain values of positive and negative fields (vertical dashed lines in Figure 5.25), respectively. After these values, in fact, the experimental threshold current density tends to saturate (horizontal dashed lines in Figure 5.25) due to the effect of H_x instead of diverging, as Equation 5.7 would predict [25]. We individuate the saturation window as the range of fields in which the switching current densities do not differ more than $2\times10^5 \frac{A}{cm^2}$ from each other.
It corresponds to H_y < -750 Oe and H_y > 750 Oe for H_x = 1500 Oe, H_y < -1000 Oe and H_y > 1000 Oe for H_x = 2000 Oe, H_y < -750 Oe and H_y > 750 Oe for H_x = 2500 Oe.
The data outside the saturation windows (first field belonging to the saturation window included) are therefore used for the fit with Equation 5.7.
The parametric fitting curve can be written as:

$$j_c^{\perp} = a[B_y \pm \sqrt{b + B_y^2}] \tag{5.9}$$

Table 5.4 collects the fitting parameters a and b for positive and negative threshold curves.

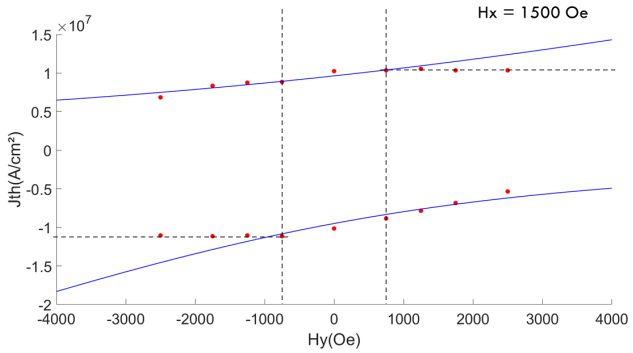

(a)

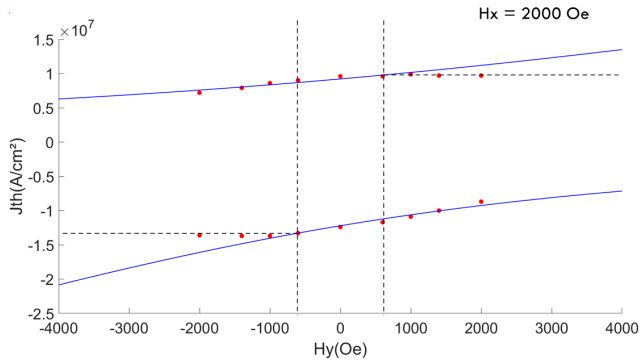

(b)

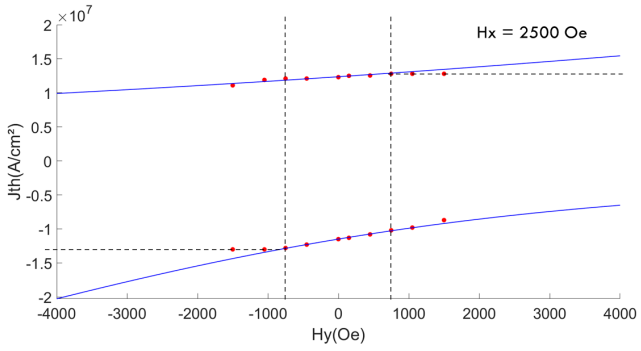

(c)

Figure 5.25: Data acquired (red dots) and fitted curves (blue curves) relative to the dependence of the positive and negative threshold current densities on H_y at fixed H_x of 1500 Oe (a), 2000 Oe (b) and 2500 Oe (c).

Equation 5.7 suggests the possibility of estimating the field-like torque efficiency $\xi_{FL} = \beta\xi_{DL}$ knowing the value of a using the relation:

$$a \simeq \frac{eM_s t}{\hbar \xi_{FL}} \tag{5.10}$$

The estimated a parameter is not uniform, therefore in principle an average of all the re-

trieved values should be performed. However, the fitting obtained for $H_x = 2500Oe$ seems more reliable due to the larger H_y span covered in the experiment and as a consequence the relative average a parameter is used for the estimation of ξ_{FL}. Such a calculation yelds a value for ξ_{FL} equal to 9.41, much larger than the one usually found experimentally, equal to 0.11 $\pm$ 0.01 [25] for Ta/CoFeB system. This discrepancy is probably caused by the fact that while Equation 5.7 is derived under macrospin approximation in absence of thermal effects, the experimental data are acquired in a system in which switching occurs through domain walls nucleation and propagation and it is assisted by Joule heating. Simulations performed under the macrospin hypothesis [58] show in fact threshold current densities about two order of magnitude larger that the ones experimented here. Simply scaling the experimentally found threshold current densities of the same quantity would let us retrieve a realistic value of $\xi_{FL} \simeq 0.1$.

The data collected from the experiments at 1000 Oe do not present a H_y span large enough to make the expected trend visible. However, the sum of the positive and negative threshold currents presents the linear relationship with the transverse field derived in Equation 5.8 and the slope of the latter is similar to the one found with the measurements with H_x = 1500 Oe, 2000 Oe, 2500 Oe.

Figure 5.26 displays the experimental values of $j_c^+ + j_c^-$ plotted against H_y and the relative linear fits for longitudinal fields of 1000 Oe, 1500 Oe and 2000 Oe.

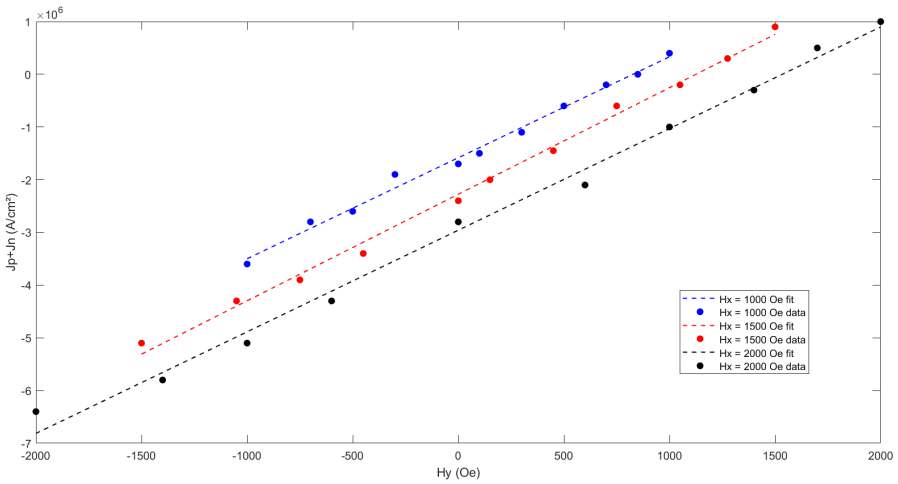

Figure 5.26: Data acquired and fitted curves relative to the dependence of sum between the positive and negative threshold current densities on H_y at fixed H_x of 1000 Oe (blue curve and points), 1500 Oe (black curve and points) and 2000 Oe (red curve and points).

The offset presented by the curves is not predicted by Equation 5.8, but it is probably caused by a spurious non controlled out of plane component of the field that favours one of

the two magnetization states thus introducing an asymmetry in absence of transverse field. This explanation is coherent with the increment of the offset following the increment of the longitudinal field, which gives rise to the spurious H_z due to the sample's misalignment. Table 5.5 gathers the slopes of the fitting curves obtained for all the different values of H_x.

$H_x(Oe)$	Slope ($\frac{A}{mTcm^2}$)
1000	1.92×10^4
1500	2.02×10^4
2000	1.93×10^4
2500	1.86×10^4

Table 5.5: Slope of the linear fit of the sum between positive and negative threshold current densities vs. H_y for all the studied H_x

These values should in principle correspond to the sum of the a parameters of Equation 5.10 obtained by fitting the positive and the negative thresholds' curves. However, they are smaller, probably due to a non optimal fitting of Figure 5.25 caused by lack of data. The slope of the curves of Figure 5.26 shows better uniformity of the fitting parameter with respect to the case of the threshold density currents curves of Figure 5.25. Since this slope is equal to twice the parameter a of Equation 5.9, we should in principle use it to obtain a more realistic value of ξ_{FL}. Plugging the average of the retrived slopes in the formula for $2a$ we find $\xi_{FL} \simeq 14.8$, still compatible with values from literature once scaled by two orders of magnitude.
The magnitude of the dependence between hysteresis asymmetry and H_y of Figure 5.26 allows to exclude the influence of a spurious transverse field due to sample misalignment on the dependence of the loop's asymmetry on H_x illustrated in Figure 5.23. With a misalignment of ϕ of, say, around 2°, the y component of the field would be about $\frac{H_x}{\theta(inrad)} = 0.03H_x$. If the loops' asymmetry Δj_c of Figure 5.23 was caused by the non controlled H_y the derivative of the former with respect to the latter should be about $\frac{d\Delta j_c}{0.03dH_x} \simeq 1.92\times10^5\frac{A}{mTcm^2}$, which is way larger than the slope retrived from the data collected with variable H_y.
Finally, for sake of completeness, we investigate the dependence of the width of the R_{xy}-J hysteresis loops on the transverse field H_y. The results are plotted in Figure 5.27.

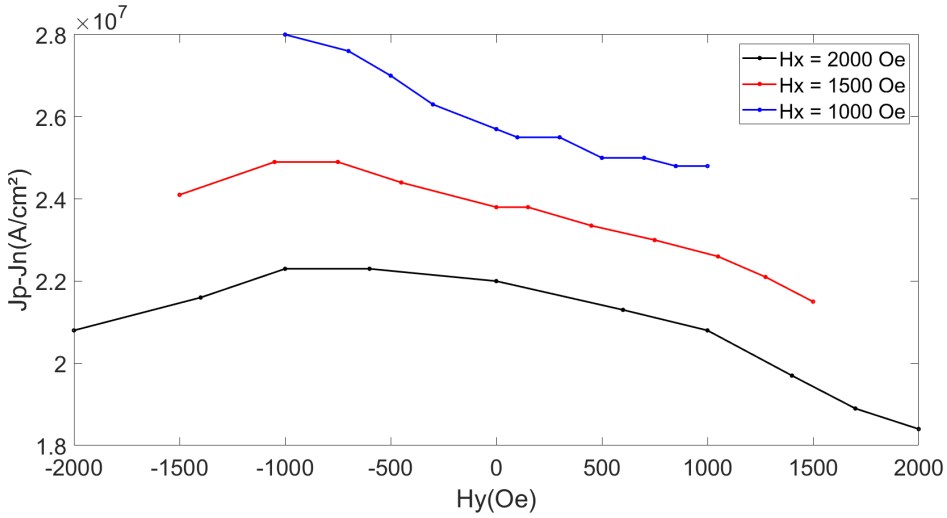

Figure 5.27: Data acquired relative to the dependence of difference between the positive and negative threshold current densities on H_y at fixed H_x of 1000 Oe (blue curve), 1500 Oe (black curve) and 2000 Oe (red curve) .

The width of the R_{xy}-J hysteresis loops tends to be smaller for positive transverse fields, meaning that switching is favoured for positive values of H_y. This suggest the possibility of the presence of an internal bias field also in the y direction, compatible indeed with the field-like effective field. Ref. [59] reports SOT switching promotion for transverse fields directed as the field-like field and hindering of SOT switching for transverse field directed in the opposite way.

5.6. Attemp of realizing multistate switching tunable with a transverse field

Today's computing systems are primarily built based on the von Neumann architecture where data must be moved to a processing unit. During the execution of various computational tasks, large amounts of data need to be moved back and forth between the processing and memory units and this determines significant costs in latency and energy. The latency associated with accessing data from the memory units is a key performance bottleneck for a range of applications, in particular for the rapidly growing field of artificial intelligence (AI) [41]. One of the approaches developed to tackle this problem is the in-memory computing, in which the memory unit is composed by elements that, arranged and controlled properly, allow computation thus avoiding data transfer with a CPU.
In the landscape of devices for in-memory computing, memristors have gained large interest in the recent years, due to their potential to enable efficient brain-inspired computing

[29]. Memristors are two-terminal electronic devices whose conductance can be precisely modulated by charge or flux through it [13] in a non volatile way and this property makes them a suitable implementation of synapses gain of neurons in neural networks. As figure 5.28 shows, the inputs of the neuron get multiplied by the relative synaptic weights and the sum of these multiplications are fed to a non linear activation function.

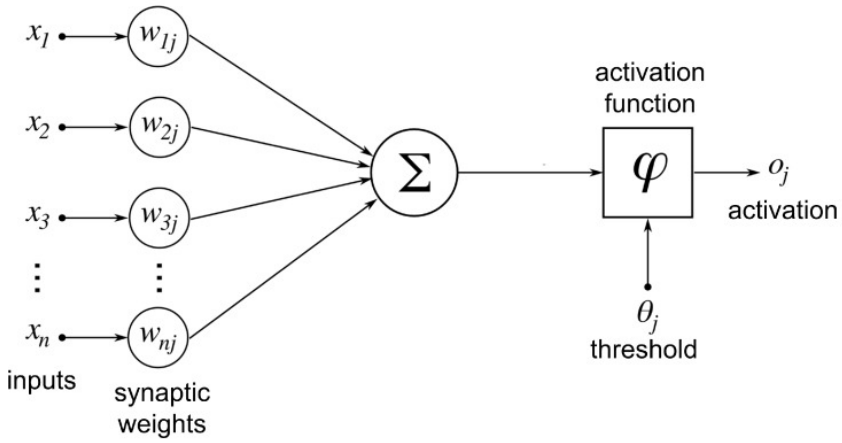

Figure 5.28: Block diagram of a neuron. From Ref. [3]

Considering the memristor's conductance G as the synaptic weight, then an array of input voltages $\boldsymbol{v_{in}} = [v_1, .., v_n]$ gets transformed in an array of currents thanks to the first Ohm's law: $\boldsymbol{I} = [G_1 v_1, .., G_n v_n]$. The currents then can be easily summed into the virtual ground node of an operational amplifier in negative feedback configuration thus performing in a very simple way the dot product the vector of input voltages and the vectors of synaptic weights.

After each training session the synaptic weights get updated to improve the accuracy of the network's output. Memristors are characterized by the possibility of using voltage pulses to change their conductance and therefore to execute fast and efficient training [29].

Spintronics can be exploited to implement these devices thanks to the possibily of controlling the magnetization texture by means of current induced spin orbit torques and of exploiting effects such as AHE of TMR to detect it.

In the case of trilayer with PMA, it is possible to use SOT to induce intermediate magnetization states that translate into a gradual transition of AHE transverse resistance between the fully up and fully down resistive states [13]. These resistive states are non volatile and current controlled, therefore giving the device a memristive behaviour.

The last part of the experimental work discussed in this thesis deals with the study of the possibility of using SOT to realize multistate switching in the fabricated Hall bars,

following the approach of Ref. [13]. In addition, we explore the potentiality of using a transverse field to control intermediate states owing to the influence of H_y on the switching behaviour discussed in section 5.5.
The experiment performed is similar to the one described in Ref. [13]. A sequence of trains of ten pulses of increasing amplitude is injected into the device and after each pulse the transverse resisted is recorded. For a given amplitude, train of pulses of both polarities are sent in order to toggle the state of the magnetization periodically. Finally, the current waveform is the one of Figure 5.29.

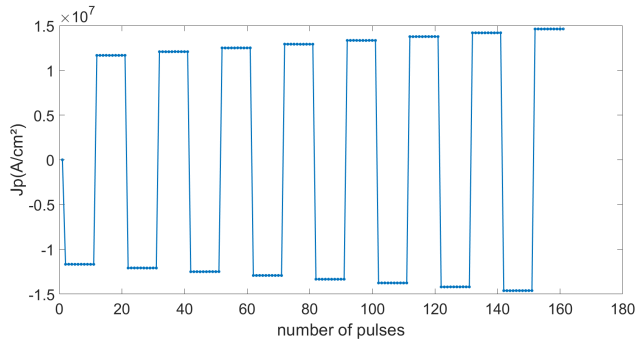

Figure 5.29: Current waveform used for the experiment. Each point corresponds to a current pulse.

The working conditions, namely initial current density and working longitudinal field, are chosen based on the R_{xy}-H_p measurements, which shows the arising of a SOT induced intermediate state around 100 Oe for a current density of $1.2 \times 10^7 \frac{A}{cm^2}$ (Figure 5.30).

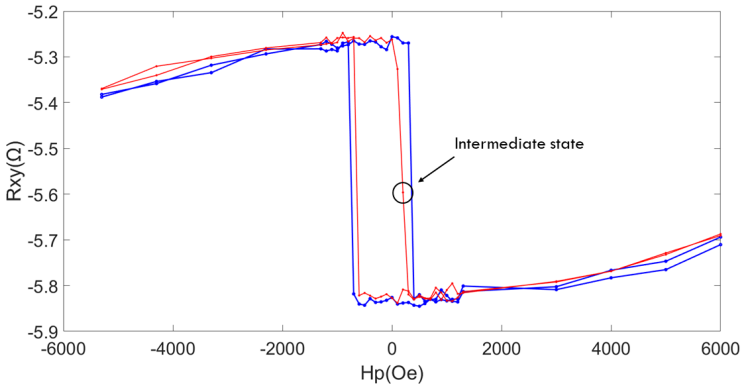

Figure 5.30: R_{xy}-H_p loop measured on a different device with the same geometry with current density pulses of $1.2 \times 10^7 \frac{A}{cm^2}$. The red curve is recorded after the injection of negative pulses and it shows intermediate states between 100 Oe and 300 Oe.

A value of 110 Oe is therefore chosen for H_x and the sequence of train pulses spans values from $\pm 1.16 \times 10^7 \frac{A}{cm^2}$ to $\pm 1.46 \times 10^7 \frac{A}{cm^2}$ with a step of $3.75 \times 10^5 \frac{A}{cm^2}$. In absence of transverse field the resistive response of the device shows only one intermediate state in the transition from upper state to the lower one for current densities equal to $-1.29 \times 10^7 \frac{A}{cm^2}$ and $-1.33 \times 10^7 \frac{A}{cm^2}$ while no intermediate states are observed in the opposite transition, coherently with the R_{xy}-H_p measurement. For larger current densities the switching becomes completely digital. Four pulses with the same intensity are needed to push the system out from the intermediate state, which are equal to around 10.82 Ω. The results are plotted in Figure 5.31.

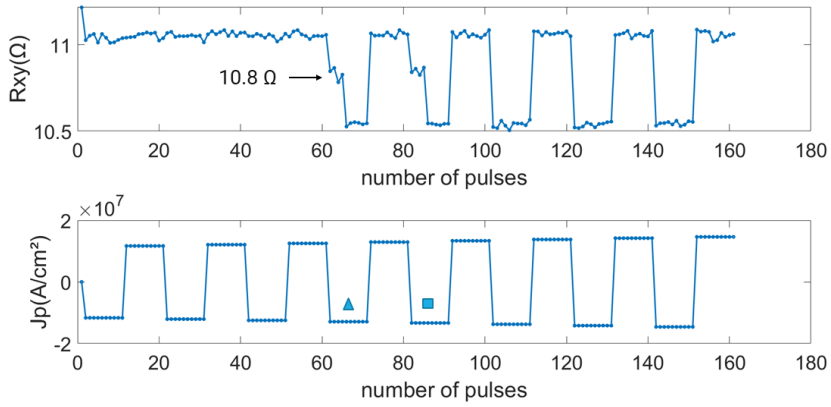

Figure 5.31: Time evolution of the transverse resistance of the device under study under the application of the described train pulses sequence. The pulses with the triangle corresponds to current density of $-1.29 \times 10^7 \frac{A}{cm^2}$, the pulses with the square correspond to current density of $-1.33 \times 10^7 \frac{A}{cm^2}$

Successively, the experiment is repeated for the same $H_x = 110$ Oe but introducing different values of the transverse field $H_y = [-110\,Oe,\ -55\,Oe,\ 55\,Oe,\ 110Oe]$.
We first discuss the cases with positive H_y, plotted in Figure 5.32. Two measurements at 110 Oe are reported, with current densities intervals starting at different values, since they were required to record the whole transition's dynamics.

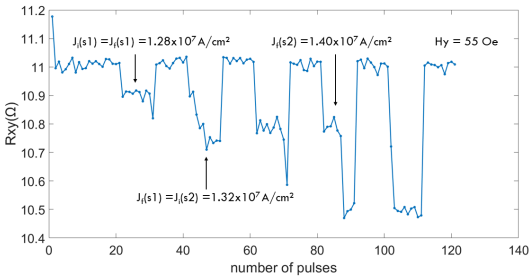

(a)

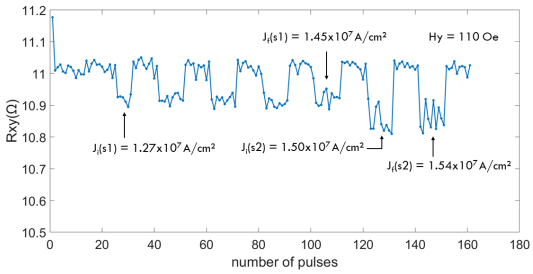

(b)

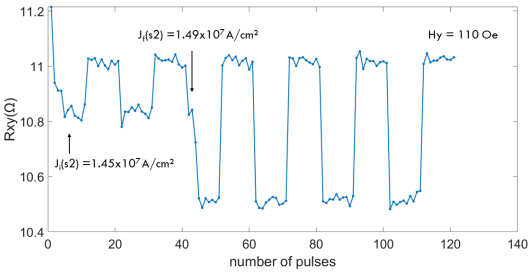

(c)

Figure 5.32: Time evolution of the transverse resistance of the device under study under the application of the train of pulses and of a transverse field $H_y = 55$ Oe (a) for current densities between $-1.23 \times 10^7 \frac{A}{cm^2}$ and $-1.54 \times 10^7 \frac{A}{cm^2}$ and $H_y = 110$ Oe for current densities ranges from $-1.23 \times 10^7 \frac{A}{cm^2}$ to $-1.54 \times 10^7 \frac{A}{cm^2}$ (b) and from $-1.45 \times 10^7 \frac{A}{cm^2}$ to $-1.67 \times 10^7 \frac{A}{cm^2}$ (c). In the three images, the quantities $J_i(s1)$, $J_f(s1)$, $J_i(s2)$, $J_f(s2)$ indicate the initial (J_i) and final (J_f) current densities giving the intermediate states s1 and s2 of resistances equal to about 10.9 Ω and 10.8 Ω, respectively. H_x is fixed to 110 Oe.

We can clearly observe that in these new configurations a new state arises, at around 10.9 Ω, while the usual state at around 10.8 Ω is still present. Both states, moreover, tend to persist for a larger current density span as H_y increases. In particular, for $H_y = 110$ Oe the state at 10.9 Ω appears for current densities between $-1.27 \times 10^7 \frac{A}{cm^2}$ and $-1.45 \times 10^7 \frac{A}{cm^2}$ while the same state only is visible between $-1.28 \times 10^7 \frac{A}{cm^2}$ and $-1.32 \times 10^7 \frac{A}{cm^2}$ for H_y

= 55 Oe. The state at 10.8 Ω, however, seems more stable at 55 Oe than at 110 Oe and at 0 Oe. This suggests the possibility of using H_y to control the stable intermediate switching state. In order to highlight the difference between the three cases we repeat each measurement and we plot different hystograms of the recorded resistance values of both measurements for different values of H_y, which are reported in Figure 5.33.

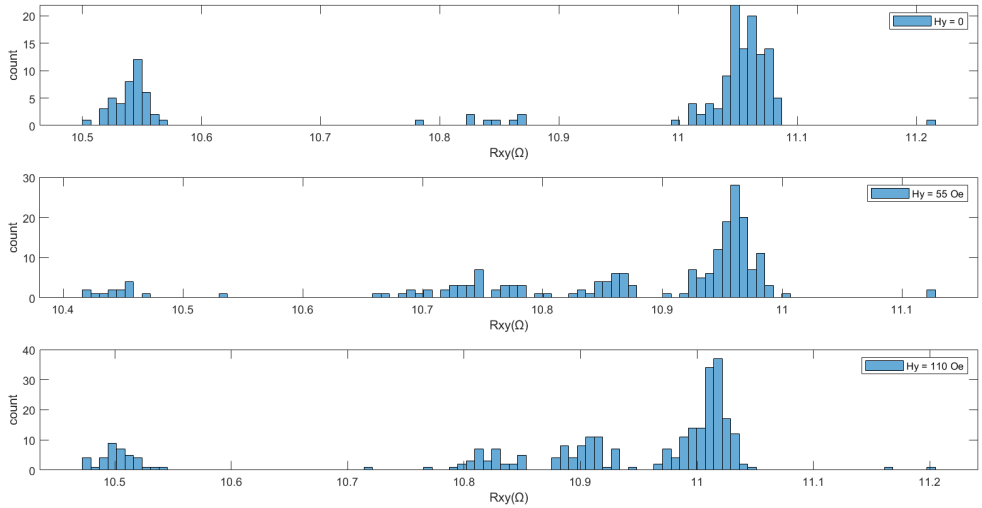

Figure 5.33: Hystograms of the resistances recorded for Hy=0 Oe (figure on the top), Hy = 55 Oe (figure in the middle) and Hy = 110 Oe (figure on the bottom).

The hystograms confirm that the two main intermediate states are the ones around 10.8 Ω and 10.9 , with the latter only appearing for H_y different from zero.
Next, we investigate the behaviour for negative H_y for the same value of H_x. Figure 5.34 reports the results of the experiments conducted for H_y equal to -55 Oe and -110 Oe.

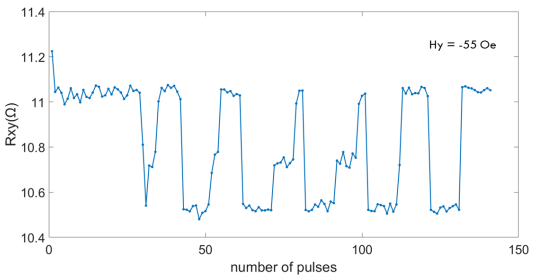

(a)

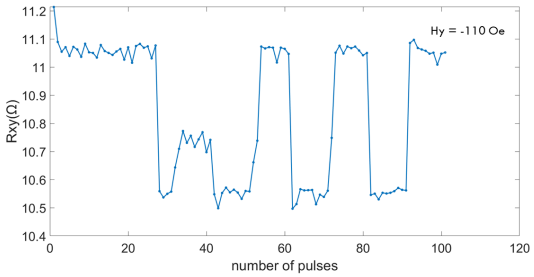

(b)

Figure 5.34: Time evolution of the transverse resistance of the device under study under the application of the train pulses sequence under the application of a transverse field of - 55 Oe (a) and - 110 Oe (b). The current density step is always about $4 \times 10^5 \frac{A}{cm^2}$.

In this case the state at 10.9 Ω is not observed but the most important difference with respect to the previous situation is that now the intermediate state occurs in the transition from the lower state to the upper one, therefore for positive current pulses. This is another feature that could be exploited in a multistate device based on the structures studied here.

A final remark goes to the sign of H_x. The same experiments are also conducted for H_x = 110 Oe, but no intermediate states are observed, probably due to the H_x asymmetry already discussed in section 5.4. However, further work has to be carried out in this regard to have a better understanding of the phenomenon.

In conclusion, we have demonstrated the possibility of realizing a multistate device controllable via SOT, whose behaviour can be tuned using an external transverse field. Of course, further experiments and micromagnetic simulations are necessary to gain a deeper knowledge of the mechanisms behind the data observed and to prove their repeatability.

6 | Conclusions and further developments

The Ta/CoFeB/MgO heterostructure has been employed for the fabrication of perpendicular magnetic tunnel junction and for the realization of deterministic Spin-Orbit Torque switching of out of plane magnetization. This work represents the first systematic study on SOT induced switching within the NaBiS research group.

A reliable process based on sputtering deposition and thermal annealing which allows to obtain Ta/CoFeB/MgO and MgO/CoFeB/Ta thin films with perpendicular magnetic anisotropy has been developed and successfully tested. The combination of the two structures has also been explored obtaining a partial degradation of PMA only in one of the two layers.

An optical lithographic process aimed at the fabrication of magnetic tunnel junction has also been presented, which permitted to attain devices with tunneling magnetoresistance up to $\simeq 100\%$. An optimization of the SiO_2 lift-off step is however required, since its partial failure limited the minimum magnetic pillar's dimension obtainable.

Successively, Ta/CoFeB/MgO based Hall bars have been optimized in order to achieve deterministic Spin-Orbit Torque switching, with particular focus on the optimal thickness of the tantalum layer.

The dependences of the switching behaviour on the input current densities and on the external applied fields have been carefully addressed, highlighting the tendency of switching to be promoted or hindered when a positive or negative field collinear to the input current are applied, respectively. We ascribe this phenomenon to the presence of an internal biasing field, which may be caused by DMI. However, micromagnetic simulations are required to validate this hypothesis and to shed light on the influence of the geometrical properties of the device on the strength of this asymmetry.

Finally, an attempt to use SOT to induce intermediate states of the magnetization has been carried out. We discovered that a near-threshold working regime exists where two additional intermediate states arise and their occurance is influenced by the presence of an external field orthogonal to the direction of the injected current. In particular, these

state are observed for positive or negative currents depending on whether the transverse field is negative or positive, respectively.
Once again, micromagnetic simulations can help gaining a better understanding of the mechanisms behind the stabilization of the detected states and on the external field dependence. This is indeed necessary to engineering the MTJs to obtain robust devices that can be employed in the realization of memristive devices for neuromorphic computing.

Bibliography

[1] What is Atomic Force Microscopy (AFM)? URL `https://afm.oxinst.com/outreach/atomic-force-microscopy`.

[2] V. Amin *et al.*. Interfacial spin-orbit torques. *Journal of Applied Physics 128*, pages 151101–1–151101–28, 2020.

[3] R. Asaad *et al.*. Back Propagation Neural Network(BPNN) and Sigmoid Activation Function in Multi-Layer Networks . *Academic Journal of Nawroz University, 8(4)*, pages 1–6, 2019.

[4] S. Bhatti *et al.*. Spintronics based random access memory: a review. *Materials today 20(9)*, pages 530–548, 2017.

[5] M. Bowen *et al.*. Spin-polarized tunneling spectroscopy in tunnel junctions with half-metallic electrodes. *Physical review letters 95, 137203*, pages 137203–1–137203–4, 2005.

[6] P. Bruno. Physical Origins and Theoretical Models of Magnetic Anisotropy. 1993.

[7] M. Butler *et al.*. Spin-dependent tunneling conductance of Fe/MgO/Fe sandwiches. *Physical review B 63, 054416*, pages 054416–1–054416–12, 2001.

[8] J. Cao *et al.*. Spin-orbit torque induced magnetization switching in Ta/Co20Fe60B20/MgO structures under small in-plane magnetic fields. *Applied Physics Letters 108, 172404*, pages 172404–1–172404–5, 2016.

[9] S. Cao *et al.*. Spin-orbit-torque-driven multilevel switching in Ta/CoFeB/MgO structures without initialization. *Applied Physics Letters 114, 042401*, pages 042401–1–042401–4, 2019.

[10] R. Caraballo-Vivas. *Magnetism from intermetallics and perovskite oxides*. PhD thesis, Centro Brasileiro de Pesquisas Físicas, 2017.

[11] J. Coey. *Magnetism and Magnetic Materials*. Cambridge University Press, 2010.

[12] M. Cubukcu *et al.*. Spin-orbit torque magnetization switching of a three-terminal

perpendicular magnetic tunnel junction. *Applied Physics Letters 104*, pages 042406–1–042406–5, 2014.

[13] B. Dieny *et al.*. Perpendicular magnetic anisotropy at transition metal/oxide interfaces and applications. *Reviews of modern physics, 89*, pages 025008–1—-025008–54, 2017.

[14] W. Fan *et al.*. Asymmetric Spin-Orbit-Torque-Induced Magnetization Switching With a Noncollinear In-Plane Assisting Magnetic Field. *Physical review applied 11, 034018*, pages 034018–1–034018–7, 2019.

[15] A. Fert *et al.* Giant Magnetoresistance of (001)Fe/(001)Cr Magnetic Superlattices. *Physical Review Letters, 61*, pages 2472–2475, 1988.

[16] K. Garello *et al.*. Symmetry and magnitude of spin–orbit torques in ferromagnetic heterostructures. *Nature Nanotechnology, 8*, pages 587–593, 2013.

[17] T. Gilbert. A Lagrangian Formulation of the Gyromagnetic Equation of the Magnetization Field. *Physical Review D, 100*, 1955.

[18] S. Ikeda *et al.*. A perpendicular-anisotropy CoFeB–MgO magnetic tunnel junction. *Nature Materials 9*, pages 721–724, 2010.

[19] S. Ikegawa *et al.* Magnetoresistive Random Access Memory: Present and Future. *IEEE transaction on electron devices, 67(4)*, pages 1407–1419, 2020.

[20] J.C.Slonczewski. Current-driven excitation of magnetic multilayers. *Journal of Magnetism and Magnetic Materials, 159 (1-2)*, pages L1–L7, 2011.

[21] R. Karplus *et al.*. Hall Effect in Ferromagnetics. *Physica review, 95*, pages 1154–1160, 1954.

[22] S. Karthik *et al.*. Transmission electron microscopy study on the effect of various capping layers on CoFeB/MgO/CoFeB pseudo spin valves annealed at different temperatures. *Journal of Applied Physics 111(8)*, pages 083922–1–083922–7, 2012.

[23] M. Khakifirooz *et al.*. Modelling and decision support system for intelligent manufacturing: An empirical study for feedforward-feedback learning-based run-to-run controller for semiconductor dry-etching process. *The International Journal of Industrial Engineering: Theory, Applications and Practice, 25(6)*, pages 828–842, 2018.

[24] G. Kim *et al.*. Spin–orbit torque engineering in -W/CoFeB heterostructures with W–Ta or W–V alloy layers between -W and CoFeB. *NPG Asia Materials*, pages 1–9, 2019.

[25] V. Krizakova *et al.*. Tailoring the switching efficiency of magnetic tunnel junctions by the fieldlike spin-orbit torque. *arXiv:2206.14587*, 2022.

[26] D. Lee *et al.*. Spin-orbit Torque Switching of Perpendicular Magnetization in Ferromagnetic Trilayers. *Scientific Reports, 10*, 2011.

[27] S. Lee *et al.*. Texture, structure and phase transformation in sputter beta tantalum coating. *Surface and Coatings Technology 177–178*, pages 44–52, 2004.

[28] L. Liu *et al.*. Spin-Torque Switching with the Giant Spin Hall Effect of Tantalum. *Science 336(6081)*, pages 555–558, 2012.

[29] W. Ma *et al.*. Neuromorphic computing with memristive devices. *Science China Information Sciences, 61, 060422*, pages 060422–1—-060422–9, 2020.

[30] S. Makarov *et al.*. Cmos-compatible spintronic devices: a review. *Semiconductor Science and Technology, 31*, pages 1–25, 2016.

[31] I. Mihai *et al.*. Perpendicular switching of a single ferromagnetic layer induced by in-plane current injection. *Nature, 476*, pages 189—-193, 2011.

[32] M.Julliere. Tunneling between ferromagnetic films. *Physics Letters A, 54(3)*, pages 225–226, 1975.

[33] A. Mücklich *et al.*. ART AND SCIENCE OF MICRO-PATTERNING.

[34] N. Nagaosa *et al.*. Anomalous Hall effect. *Reviews of moderm physics, 82*, pages 1539–1592, 2010.

[35] H. Nakayama *et al.*. Spin Hall Magnetoresistance Induced by a Nonequilibrium Proximity Effect. *Physical review letters, 110*, pages 206601–1–206601–5, 1954.

[36] J. Osborn. Demagnetizing Factors of the General Ellipsoid. *Physical Review 67*, pages 351–357, 1945.

[37] G. Prenat *et al.*. Ultra-Fast and High-Reliability SOT-MRAM: From Cache replacement to Normally-off Computing. *IEEE transaction on multi-scale computing systems, 2(1)*, pages 49–60, 2004.

[38] D. Ryndyk. *Theory of Quantum Transport at Nanoscale*. Springer, 2016.

[39] E. Sagasta *et al.*. Unveiling the mechanisms of the spin Hall effect in Ta. *Physical Review B, 98*, pages 060410–1–060410–7, 2018.

[40] R. Sbiaa *et al.*. Materials with perpendicular magnetic anisotropy for magnetic random access memory. *Phys. Status Solidi RRL*, pages 413–419, 2011.

[41] A. Sebastian *et al.*. Memory devices and applications for in-memory computing. *Nature Nanotechnology, 15*, pages 529—-544, 2020.

[42] S. Shen *et al.*. The Correlation Between Magnetic Dead Layer and Perpendicular Magnetic Anisotropy in MgO/CoFeB/Ta Top Structure. *IEEE transactions on magnetics 55(2)*, 2019.

[43] J. Sinova *et al.*. Spin Hall effects. *Review of modern physics, 87*, pages 1213–1259, 2015.

[44] B. Stuhrmann. *Self-Organized Active Biopolymer Networks in Migrating Living Cells*. PhD thesis, Universität Leipzig, 2009.

[45] H. Sukegawa *et al.*. Revisiting Fe/MgO/Fe(001): Giant tunnel magnetoresistance up to 420% at room temperature. *2021 IEEE 32nd Magnetic Recording Conference (TMRC)*, pages 1–2, 2021.

[46] J. Sun. Spin-transfer torque switched magnetic tunnel junction for memory technologies. *Journal of Magnetism and Magnetic Materials, 559*, 1993.

[47] S. Swann. Magnetron sputtering. *Physics in Technology 19 67*, pages 67–75, 1988.

[48] T. Taniguchi *et al.*. Critical current destabilizing perpendicular magnetization by the spin Hall effect. *Physical Review B 92, 024428*, pages 024428–1–024428–12, 2015.

[49] S. Tinti. Dispositivi di memorizzazione NVDIMM: classificazione e vantaggi, 2020. URL `https://www.e4company.com/2020/09/dispositivi-di-memorizzazione-nvdimm-classificazione-e-vantaggi/`.

[50] E. Tsymbal. Tunneling Magnetoresistance, 2003. URL `https://unlcms.unl.edu/cas/physics/tsymbal/reference/spin-dependent_tunneling/tunneling_magnetoresistance.shtml`.

[51] T. University. Team demonstrates sub-nanosecond operation of nonvolatile memory, 2016. URL `https://phys.org/news/2016-06-tohoku-university-sub-nanosecond-nonvolatile-memory.html`.

[52] W. Wang *et al.*. The perpendicular anisotropy of $Co_{40}Fe_{40}B_{20}$ sandwiched between Ta and MgO layers and its application in CoFeB/MgO/CoFeB tunnel junction. *Applied Physics Letters 99*, pages 012502–1–012502–3, 2011.

[53] Y. Weng *et al.*. Interlayer Exchange Coupling and Perpendicular Magnetic Anisotropy in $Co_{40}Fe_{40}B_{20}$ /MgO/$Co_{20}Fe_{60}B_{20}$ Tunnel Junction Structures. *IEEE transactions on magnetics, 49*, pages 4425–4428, 2013.

[54] R. W. World. Advantages of 2 Wire Resistance Measurement | Disadvantages of Two Wire resistance Measurement, 2012. URL `https://www.rfwireless-world.com/Terminology/Advantages-of-2-Wire-Resistance-Measurement.html`.

[55] R. Yu *et al.*. Determination of spin Hall angle and spin diffusion length in -phase-dominated tantalum. *Physical Review Materials 2(7)*, pages 074406–1–074406–7, 2004.

[56] R. Yu *et al.*. Dependence of inverse-spin Hall effect and spin-rectified voltage on tantalum thickness in Ta/CoFeB bilayer structure . *Applied Physics Letters 106, 032409*, pages 032409–1–032409–5, 2015.

[57] S. Yuasa *et al.*. Giant room-temperature magnetoresistance in single-crystal Fe/MgO/Fe magnetic tunnel junctions. *Nature Materials 3(12)*, pages 868–871, 2004.

[58] S. Yun *et al.*. Critical switching current density induced by spin Hall efect in magnetic structures with frstand second-order perpendicular magnetic anisotropy. *Scientific Reports volume 7, 15314*, 2017.

[59] J. Zhuo *et al.*. Mechanism of field-like torque in spin-orbit torque switching of perpendicular magnetic tunnel junction. *Science China Physics, Mechanics Astronomy, 65*, pages 107511–1–107511–6, 2022.

List of Figures

List of Tables

Acknowledgements

I want to thank Prof. Bertacco, Luca Nessi and all the people that helped me at PoliFab. A special thanks goes to my family, which has supported me and believed in me through these years.